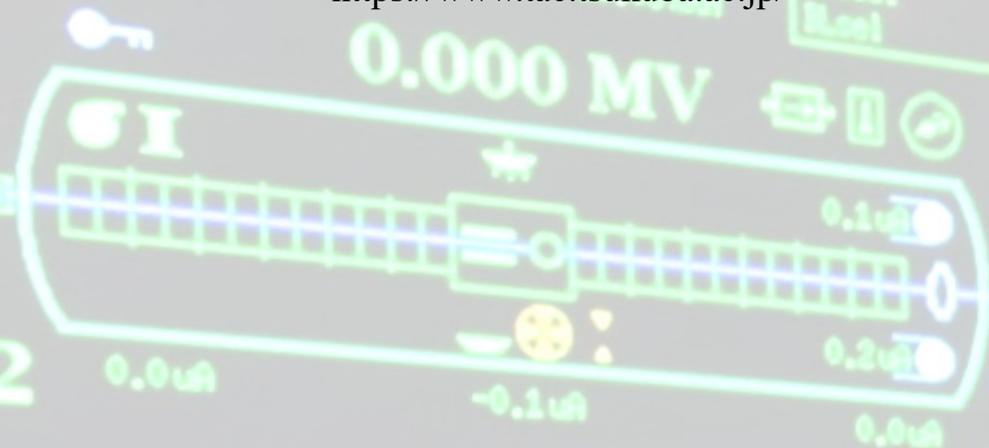UTTAC-91, 2022

UTTAC
ANNUAL REPORT 2021

TANDEM ACCELERATOR COMPLEX
Research Facility Center for Science and Technology
University of Tsukuba

https://www.tac.tsukuba.ac.jp/

UTTAC

ANNUAL REPORT 2021

April 1, 2021 − March 31, 2022

Editors : Tetsuaki Moriguchi, Kimikazu Sasa, Yoshihiro Yamato, Masumi Matsumura, Masao Sataka, Hiroshi Naramoto, Eiji Kita, and Hiroshi Kudo (editor-in-chief)

UTTAC ANNUAL REPORT is a series of issues, which describes annual research activities at Tandem Accelerator Complex, Research Facility Center for Science and Technology, University of Tsukuba.

All reports are written on authors' responsibility and thus the editors are not liable for the contents of the report.

Cover: Oblique-angle photo of the display for operating the UTTAC 6MV tandem accelerator.

PREFACE

This annual report covers research and development (R&D) carried out at University of Tsukuba Tandem Accelerator Complex (UTTAC) during the fiscal year 2021 (1 April 2021 ~ 31 March 2022). The topics include not only accelerator-based R&D using the 6MV tandem and 1MV Tandetron accelerators, but also radioisotope-based R&D employing positron annihilation spectroscopy and Mössbauer spectroscopy. Serious influence on the UTTAC's social activity by COVID-19 continued, in fact, there were no student visitors from high schools in these two fiscal years. Nevertheless, R&D using the UTTAC facility has been successfully carried out, as reported here.

September 1, 2022
Editorial board

Cooperative experiments using the 6MV tandem accelerator. Students of the University of Tsukuba and from Saitama University are learning the data acquisition system.

CONTENTS

1.

ACCELERATOR AND RELATED FACILITIES

Acceleration tube of the UTTAC 6MV tandem accelerator, viewed down from the central terminal to the high-energy end.

1.1   Accelerator operation 2021

K. Sasa, S. Ishii, T. Takahashi, Y. Yamato, Y. Tajima, M. Matsumura, T. Moriguchi

University of Tsukuba Tandem Accelerator Complex (UTTAC) is promoting the maintenance and operation of a tandem accelerator facility consisting of the 6MV Pelletron tandem accelerator and the 1MV Tandetron accelerator for cooperative researches both inside and outside the University of Tsukuba. In fiscal 2021, there were no cancellations nor postponements of machine time to prevent coronavirus infection. The number of research projects and operation time of the accelerators increased from the last year [1].

In fiscal 2021, there were 12 research projects on campus and 9 research projects shared by facilities outside the campus. The maintenance status of the facility is as follows. For the 6MV Pelletron tandem accelerator, the RF charge exchange ion source (Alphatross) was maintained in the usual way and four TMPs were overhauled. There was also a problem with the gas-stripper drive unit in the accelerator tank, which has been repaired. The neutron area monitor in the Tandetron room was updated.

1MV Tandetron accelerator

The 1MV Tandetron accelerator has 2 negative ion sources and 4 beamlines. The operation time and the experimental beam time were 644 and 286 hours, respectively, during the total service time in fiscal 2021. The 1MV Tandetron accelerator was operated for a total of 68 days. A total of 39 research programs was carried out and a total of 212 researchers used the 1MV Tandetron accelerator. Figures 1 and 2 show classification of the accelerated ions and of experimental purposes, respectively.
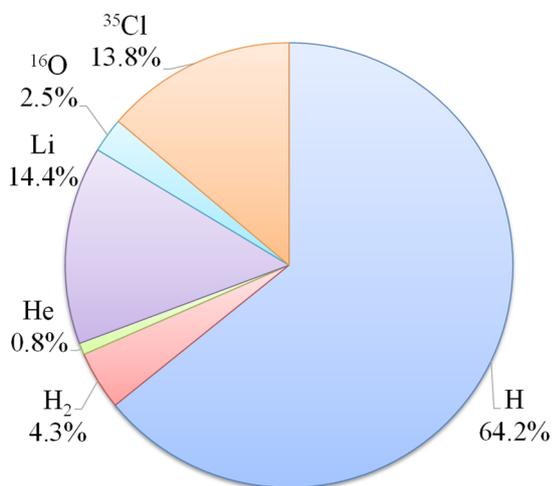
Fig. 1. Accelerated ions by the 1MV Tandetron accelerator in fiscal 2021.
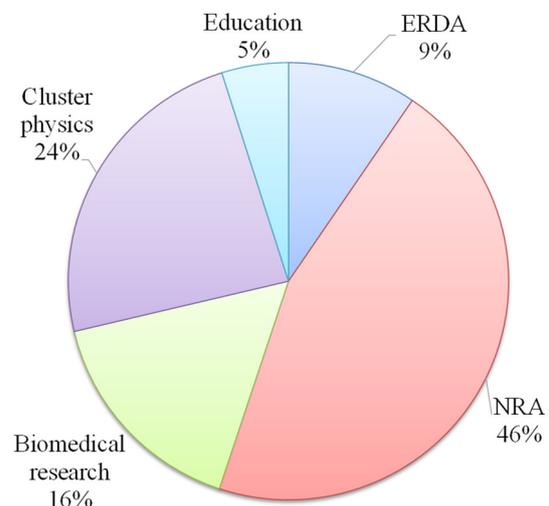
Fig. 2. Experimental purposes of the 1MV Tandetron accelerator in fiscal 2021.

6MV Pelletron tandem accelerator

The 6MV Pelletron tandem accelerator has 5 negative ion sources and 12 beamlines. The operation time and the experimental beam time of the 6MV Pelletron tandem accelerator were 1,441 and 1,148 hours, respectively, during the total service time in fiscal 2021. The operation time increased by about 34% compared to the last year. The 6MV Pelletron tandem accelerator was operated for a total of 132 days. A

total of 74 research programs was carried out and a total of 477 researchers used the 6MV Pelletron tandem accelerator. Figure 3 shows the beam time histogram with respect to the terminal voltage. Figures 4 and 5 show classification of the accelerated ions and of the experimental purposes, respectively. The main fields of application are accelerator mass spectrometry (AMS), ion beam analysis using microbeams, detector developments, nuclear experiments using polarized beams, and radiation resistance tests for space devices. In the acceleration test of the polarized deuteron beam from the Lamb shift type polarized ion source (PIS), the degree of polarization was about 65% and the beam intensity was about 30 nA downstream of the PIS. We performed Cs beam generation tests using the rubidium (Rb) sputtering negative ion source which is a modified version of the S-5 ion source (MCG-SNICS) with the aim of developing AMS for Cs-135. The Rb sputtering negative ion source can generate H^- ions of 10 μA or more, and is also used as a normal negative ion source.
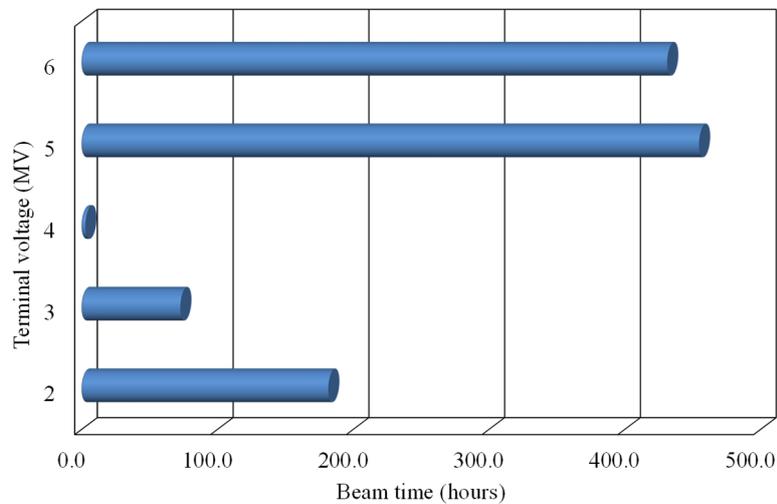
Fig. 3. Beam time histogram as a function of the terminal voltage for the 6MV Pelletron tandem accelerator in fiscal 2021.
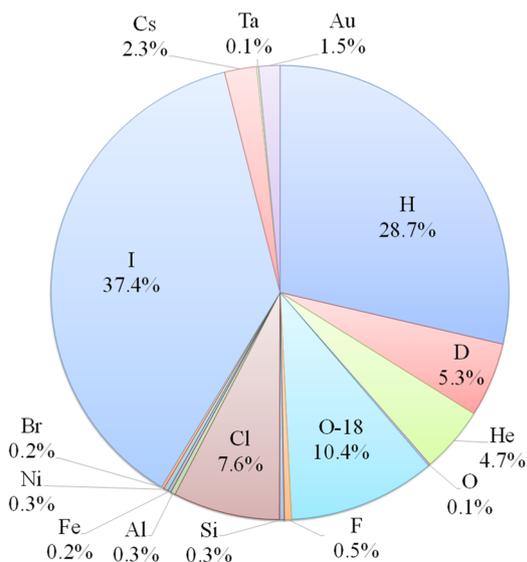
Fig. 4. Accelerated ions for the 6MV Pelletron tandem accelerator in fiscal 2021.
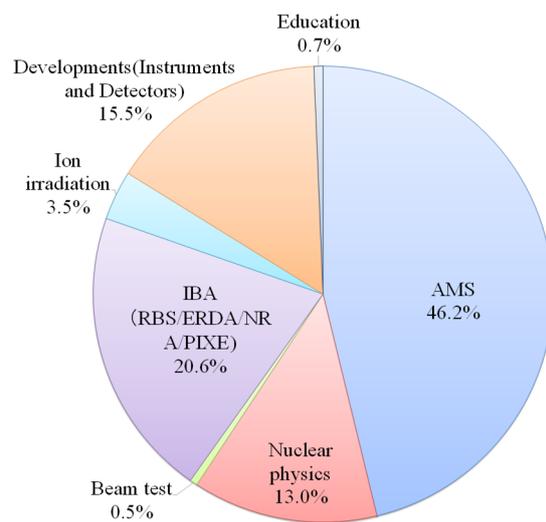
Fig. 5. Experimental purposes of the 6MV Pelletron tandem accelerator in fiscal 2021.

Reference

[1] K. Sasa et al., UTTAC Annual Report 2020, UTTAC-90 (2021) 1.

1.2 Approach to possible maximum energies of ions accelerated by the 6MV tandem accelerator

M. Sataka, T. Takahashi, H. Naramoto, H. Kudo, K. Sasa

Acceleration tests of ion beams obtained from the 6MV tandem accelerator at UTTAC have been continued [1]. The experimental data of the highest energies of available ions is indispensable for radiation resistance tests of semiconductors used in space [2]. Very weak beams are needed in these tests. On the other hand, high intensity beam is important for ion irradiation experiment for material science such as ion beam modification of materials [3].

In this fiscal year, Fe and Ta ions were newly tested, while Al and Ni data were updated. We have measured beam currents of the accelerated ions as a function of the ion charge at terminal voltages from 3 to 6 MV. Figure 1 shows the beam current distributions of Fe ion as a function of the ion charge at the maximum terminal voltage of 6 MV. Argon gas and a carbon foil were used as the strippers at the 6 MV terminal. The gas pressure was about 5 μPa, and the thickness of the carbon foil was about 5 μg/cm^2. The ion current distribution for the foil stripper shifts to higher charge state by about 3 than for the gas stripper.
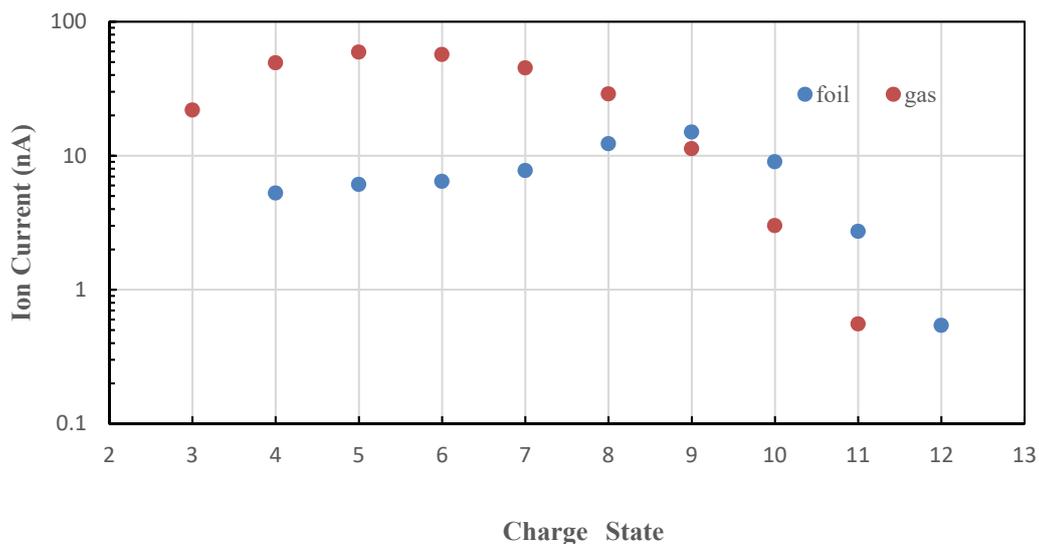
Fig. 1. Ion beam current distribution of Fe ion for the terminal voltage of 6 MV. Both gas and foil strippers were used at the high voltage terminal.

In the acceleration tests, negative molecular Al ions were injected towards the high voltage terminal. In this case, the accelerated Al energy cannot be determined only by the terminal voltage and the ion charge state of Al after acceleration. The maximum acceleration energy of 51 MeV was obtained in this test using the gas stripper.

Table 1 shows the available beam current of Al, in addition to N, Ca, Sc, Ti, Mo, and W, which were investigated until the last fiscal year. Table 2 shows the ion charges and maximum energies obtained for injection of negative atomic ion at the terminal voltage of 6 MV, which have been accumulated from 2016 to 2021.

Table 1. Available beam current of ions obtained by molecular ion injection at the terminal voltage of 6 MV, which have been accumulated since 2016. The measured beam intensity is shown by the symbols: ○: ≥ 1nA, △: ≤1nA. The data shown in red were collected by using foil strippers.

charge state	N	Al	Ca	Sc	Ti	Mo	W
14							
13				△	△		
12				○	○		
11				○	○		△
10			△	○	○	△	△
9			△	○	○	○	○
8		△	△	○	○	○	○
7		○		○	○	○	
6	△	○	△	○	○	○	
5	○	○	△	○	○	○	
4	○	○		○	○	○	
3	○	○		○	○		
2	○	○					
1							

Table 2. Summary of the acceleration tests from 2016 to 2021 for negative atomic ion injection at the terminal voltage of 6 MV. The measured beam intensities are shown by the symbols: ○: ≥ 1nA, △: ≤1nA. The data shown in red were collected by using foil strippers.

charge state	energy (MeV)	H	He	Li	B	C	O	F	Al	Si	S	Cl	Fe	Ni	Cu	Br	Ag	I	Ta	Au
14	90													△		△	△	○		△
13	84													○	△	○	△	○		△
12	78												△	○	○	○	○	○		○
11	72								△	△			○	○	○	○	○	○		○
10	66									○	○	○	○	○	○	○	○	○		○
9	60								△	○	○	○	○	○	○	○	○	○	△	○
8	54					○	○		○	○	○	○	○	○	○	○	○	○	△	○
7	48					○	○	○	○	○	○	○	○	○	○	○	○	○		
6	42				○	○	○	○	○	○	○	○	○	○	○	○	○	○		
5	36				○	○	○	○	○	○	○	○	○	○	○	○	○			
4	30				○	○	○	○	○	○	○	○	○	○	○					
3	24			○	○	○	○	○	○	○	○	○	○							
2	18		○	○	○	○	○	○	○		○									
1	12	○	○	○	○															

References

[1] M. Sataka et al., UTTAC Annual Report 2020, UTTAC-90 (2021) 3 and references therein.

[2] T. Shiobara et al., this Annual Report 6.2.

[3] M. Matsui et al al., this Annual Report 6.3.

1.3 Present status of the Lamb-shift polarized ion source

T. Moriguchi, Y. Yamato, A. Ozawa, N. Kaname, A. Moriyama, A. Yano

The Lamb-shift polarized ion source (PIS) is one of the injectors for the 6MV Pelletron tandem accelerator which was installed as the new main machine at UTTAC in 2014 [1]. PIS, which was damaged seriously by the 2011 disaster, was also newly reconstructed along with the installation of the new machine [2]. PIS can produce highly polarized negative proton and deuteron beams. Until now, the polarized protons have been mainly used to measure nuclear magnetic moments of unstable nuclei, while the polarized deuterons were accelerated by the 6MV Pelletron tandem accelerator for the first time in FY2021 [3]. In this report, we refer to the present status of PIS.

For maintenance of the duoplasmatron (DP), we open the DP chamber and clean several electrodes at least one time for every year to remove cesium deposits inside the chamber. As shown in Fig. 1 (a) and (b), the cesium deposits turn white around the electrodes. These deposits originate from cesium vapor from the cesium cell, and cause discharges frequently. The present electrodes in DP are almost the same as the replaced ones in 2018 [4]. The turbomolecular pump (TMP) used for DP was broken several times so far. The present TMP shown in Fig. 1 (c) is of a magnetic levitation type (TG907M, Osaka Vacuum, Ltd.), which was installed in 2019, and has been stably operated. TMP of the electrostatic analyzer (ESA), which is located downstream of PIS for $90°$ deflection of the beam, was also repaired because of cracks in the bearing in 2020. The present cesium cell replaced the previous one in 2018 [4]. Immediately after installing this cesium cell, the cesium leakage occurred and the cell was repaired in 2019. The beam fluctuation derived from two focus lenses downstream of an argon gas cell disappeared after grounding their two electrodes using the two electrical resistors of 100 MΩ, as shown in Fig. 1 (d). The power supply of the Wien filter (WF) was replaced by new one in 2021 because of deterioration of the previous one after being used for more than 40 years. The spin filter (SF) is of significance for nuclear polarization using PIS. Since operation of the 6MV Pelletron tandem accelerator started, SF has been in stable operation without serious troubles since it was constructed for the previous tandem accelerator at UTTAC in 1976 [5]. We are continuing to maintain PIS for its stable operation.

References
[1] K. Sasa et al., UTTAC Annual Report 2014, UTTAC-84 (2015) 1.
[2] T. Moriguchi et al., UTTAC Annual Report 2014, UTTAC-84 (2015) 6.
[3] T. Moriguchi et al., this Annual Report 2.2.
[4] T. Moriguchi et al., UTTAC Annual Report 2018, UTTAC-88 (2019) 3.
[5] Y. Tagishi et al., Nucl. Instr. Meth. 164 (1979) 411.
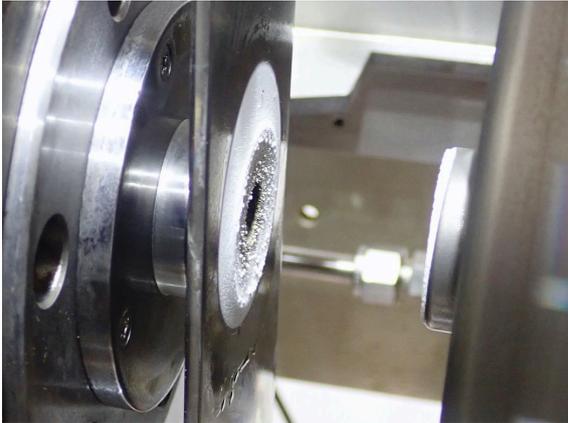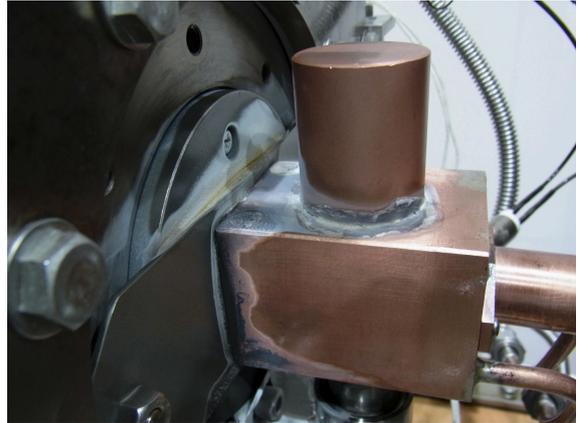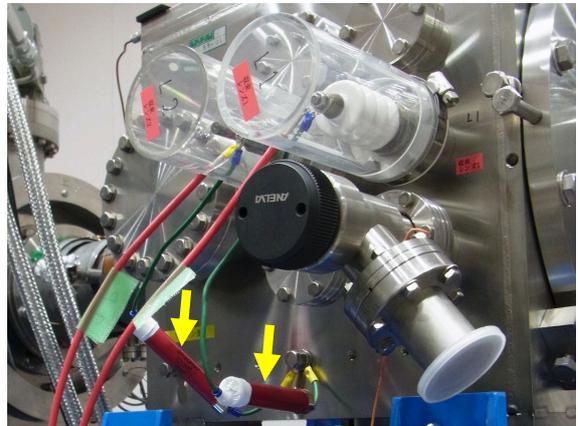
Fig. 1. (a) Cesium deposits around the aperture of the extractor in the DP chamber. (b) Cesium deposits around the cesium cell. (c) The present turbomolecular pump for DP. (d) Two electrical resistors grounding the two electrodes of focus lenses, indicated by yellow arrows.

1.4 Pilot study for visualizing accelerator activation with the portable γ-ray imaging device: GeGI5

G. Yoshida[1], H. Matsumura[1], A. Toyoda[1], T. Miura[1], H. Nakamura[1], K. Masumoto[1], K. Sasa, T. Moriguchi, M. Matsumura

Accelerator activation is a serious problem in terms of radiation protection of workers and waste management of radioactive materials. There has been no method to evaluate the activation of accelerator facility, except for direct survey with a γ-ray detector such as a scintillation survey-meter. Direct survey is inefficient and also of high risk of radiation exposure. The portable γ-ray imaging device (imager), which has been rapidly developed since the Fukushima nuclear accident, can be supposed to be a breakthrough to visualize the γ-rays from the radiation source, hence we have been tackling the application of this novel instrument to evaluation of accelerator activation. Although there have been a variety of commercial γ-ray imagers with different measurement methods and detector crystals, no model has responded to the requirements to evaluate accelerator activation; specification of activation sites, residual nuclides, and their activity. We conducted benchmark tests with various commercial devices assuming an actual accelerator activation, and found the best candidate GeGI5 manufactured by PHDS Co., US-TN [1]. We are investigating the above requirements for evaluation of accelerator activation with GeGI5 at accelerator facilities in Japan.

Currently, portable γ-ray imaging devices commercially available employ one of three representative measurement methods: "pinhole", "coded-mask", and "Compton-scattering" [2]. From the pre-selection tests, we adopted GeGI5 (Fig. 1) which employs Compton-scattering method as the best candidate for evaluating the accelerator activation. Through the series of selection tests, we found that the most important factor is detection efficiency of the device. The detection efficiency of GeGI5 was outstanding among the compared models equipped with a relatively large Ge single crystal of 90 mm diameter and 11 mm thickness.

Fig. 1. Overview of GeGI5.

According to our previous activation studies, the UTTAC facility would be ideal for a pilot study of imaging device because activated areas are limited [3]. We measured activation of the beamlines of 6MV tandem accelerator at UTTAC with GeGI5 just after stopping the acceleration of a proton beam. Short-lived nuclei attributing to beam-loss were generated at certain places and we identified their locations by radiation scanning with the survey-meter. From the screening result, we adopted the flexible joint at the middle of the beamline as the target object for the imaging test. The maximum surface dose rate of the object was 3.5 μSv/h, and the principal radionuclide was ^{56}Co. We obtained visualized images of the radiation source with changing the measurement time and the distance between source and detector.

Figure 2 shows the time-lapse of visualized images of the radiation source. GeGI5 was set 40 cm distant

---

from the object. As a characteristic of the Compton-scattering method, arc shapes depending on incident γ-ray energy and scattering angle are projected onto the screen at the 40 cm distance from the object. Color of the arc reflects the number of overlaps (amount of statistics), in particular, the red area corresponds to the most probable site of the source. The arcs overlap at the flexible tube for about 30 minutes. Similar measurements at different distances showed that the time required to identify the source sites is inversely proportional to the square of the distance and can be standardized using statistics recorded by the device.
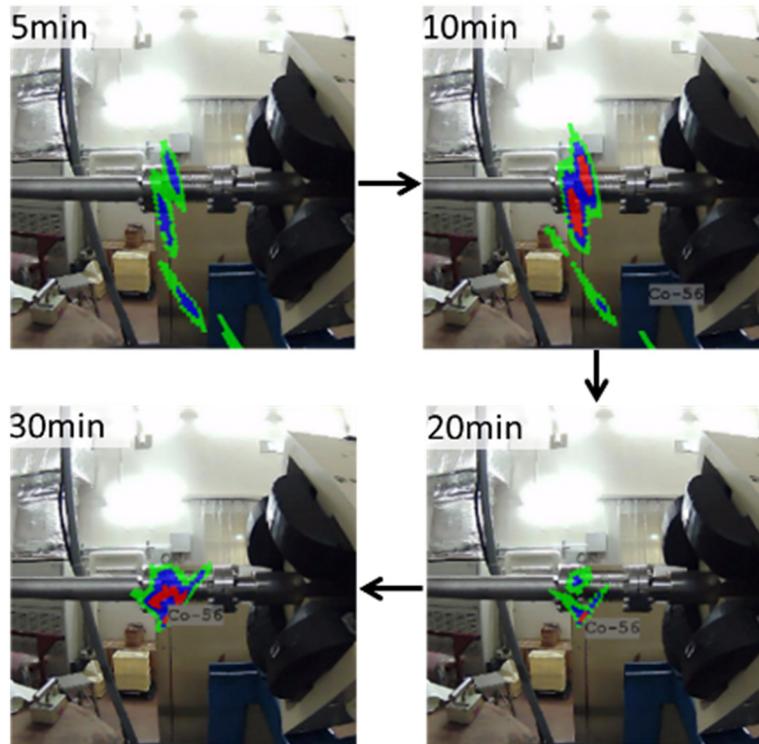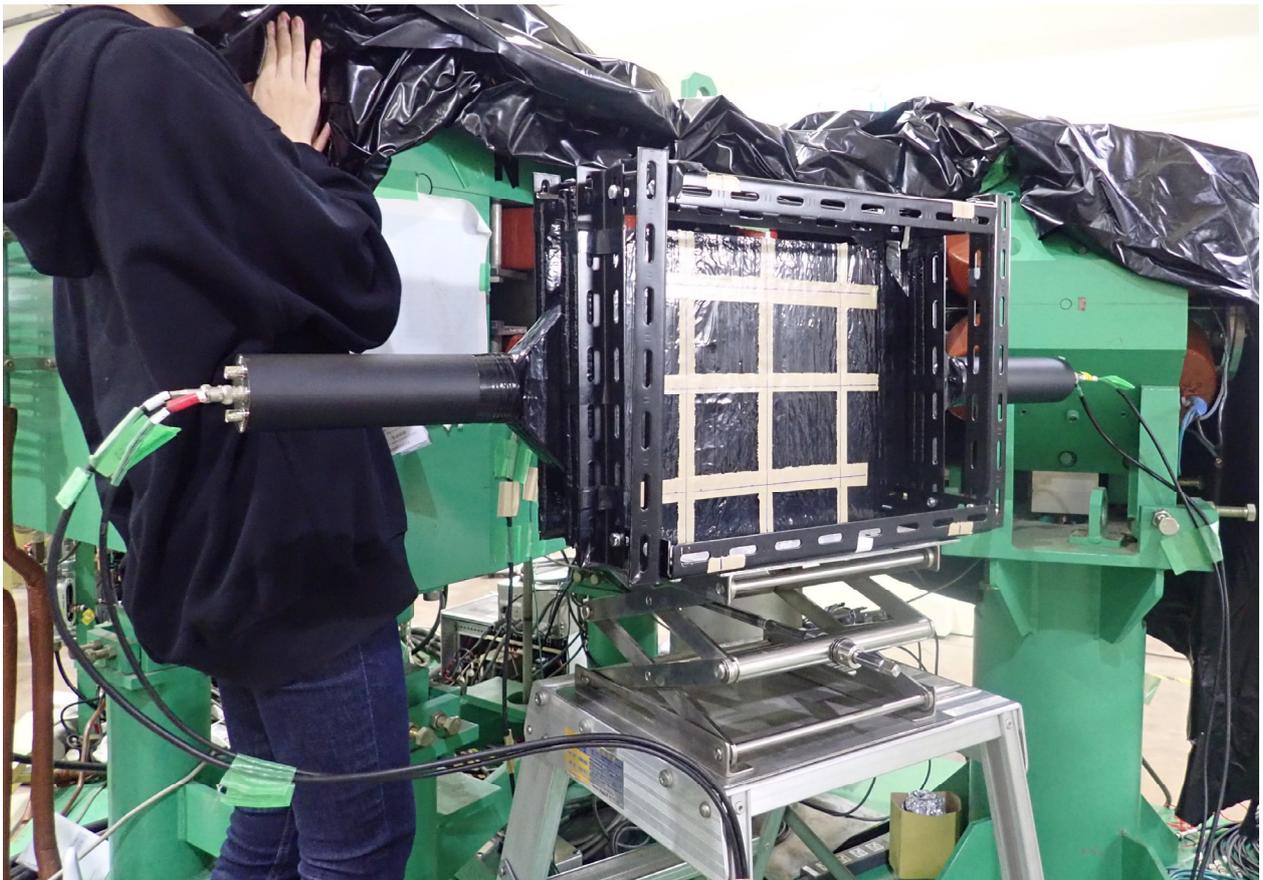

Fig. 2. Time-lapse of visualized images of the radiation source (activated flexible tube).

References

[1] G. Yoshida et al., SORC2021, on-line (2021) 3K13.

[2] G. Yoshida et al., Environmental Radiochemical Analysis VI (2019) 183.

[3] G. Yoshida et al., Radiation Safety Management 20 (2021) 1.

2.

NUCLEAR AND ATOMIC PHYSICS

Plastic scintillation detector

2.1 Measurement of the sign of nuclear moment for unstable nucleus ^{25}Al by using rotating magnetic field

A. Ozawa, T. Moriguchi, Y. Yamato, N. Kaname, A. Moriyama, A. Yano

We developed rotating magnetic field system to determine the sign of nuclear magnetic moments (μ's) for unstable nuclei. In FY2020, we have succeeded in determining the positive sign of μ for ^{29}P (I^{π}=1/2^{+}) [1]. In FY2021, we confirmed the sign of μ for ^{29}P based on the sign of μ of ^{20}F, which is known to be positive [2]. Furthermore, based on the sign of μ for ^{29}P, we determined the sign of μ for ^{25}Al(I^{π}=5/2^{+}).

Our rotating magnetic field system is presented in Ref. [3]. If the β-NMR effect disappears in a clockwise (counterclockwise) rotating magnetic field when the static magnetic field is downward, the sign is positive (negative). In our system, we use cross coils to generate a rotating magnetic field, and we put a cable delay between the two high frequency systems to create a phase difference between the cross coils. The phase difference produces the clockwise (or counterclockwise) rotating magnetic field. The experiment was conducted at the 6MV tandem accelerator at UTTAC. In the ^{29}P confirmation experiment, the polarized deuteron beam was accelerated to 6 MeV and the CaF$_2$ target was irradiated to generate polarized ^{20}F. The static magnetic field was set to ~4.3 kG with downward, and RF was set to ~3.3 MHz including the Larmor frequency of ^{20}F in this magnetic field. This frequency corresponds to a period of ~320 ns. The β-NMR effect for ^{20}F disappeared when we put ~250 ns cable delay. Next, a polarized deuteron beam was applied to the Si target to generate polarized ^{29}P. The static magnetic field was set to ~1.7 kG and RF was set to ~3 MHz including the ^{29}P Larmor frequency in this magnetic field. The β-NMR effect for ^{29}P disappeared when a cable delay of ~270 ns was inserted. Since the β-NMR effect for ^{29}P disappeared with almost the same cable delay as in the case of ^{20}F, it was confirmed that μ for ^{29}P is of the same positive sign as for ^{20}F. Next, the sign measurement for ^{25}Al was performed with ^{29}P as a reference. The polarized proton beam was accelerated to 12 MeV and irradiated to the Si target to generate polarized ^{29}P. The static magnetic field was set to ~3.5 kG with downward, and RF was set to ~6.7 MHz including the ^{29}P Larmor frequency in this magnetic field. This frequency corresponds to a period of ~155 ns. The β-NMR effect for ^{29}P disappeared when we put a delay of ~10 ns. Next, a polarized proton beam was applied to the Si target to generate polarized ^{25}Al. The static magnetic field was set to ~6 kG, and RF was set to ~6.6 MHz including the ^{25}Al Larmor frequency [4] in this magnetic field. The β-NMR effect for ^{25}Al disappeared when a delay of ~20 ns was inserted. Since the β-NMR effect disappeared with almost the same delay as in the case of ^{29}P, it is shown that μ for ^{25}Al is of the same positive sign as for ^{29}P. The positive sign for ^{25}Al is consistent with prediction by the Schmidt value (μ=+4.7926 n.m.) for the nucleus (odd Z, l=2).

References

[1] A. Ozawa et al., UTTAC Annual Report 2020 (2021) 7.

[2] T. Tsang and D. Connor, Phys. Rev. 132 (1963) 1141.

[3] K. Tomita et al., UTTAC Annual Report 2019 (2020) 8.

[4] N. J. Stone, Atomic Data and Nuclear Data Tables 90 (2005) 75.

2.2 Acceleration of polarized deuterons for observation of the nuclear magnetic resonance of ^{20}F

T. Moriguchi, Y. Yamato, A. Ozawa, N. Kaname, A. Moriyama, A. Yano

The Lamb-shift polarized ion source (PIS) at UTTAC is able to produce highly polarized proton and deuteron beams [1, 2]. Since the operation of the 6MV Pelletron tandem accelerator was started, polarized proton beams from PIS have been mainly used to measure nuclear moments of unstable nuclei [3-8]. So far, acceleration of polarized deuteron beams has been limited because of the induced radioactivity. According to the recent report, the air dose rate during the irradiation of deuteron beams under the certification in UTTAC is less than that of proton beams [9]. In FY2021, we performed acceleration of polarized deuterons for the first time with the 6MV Pelletron tandem accelerator to observe the nuclear magnetic resonance (NMR) of an unstable nucleus ^{20}F ($t_{1/2} = 11.0160$ sec [10]).

To maximize beam currents from PIS, we optimized the several parameters of PIS. The beam currents were measured by the Faraday cup (FC-PIS), which is located just downstream of PIS. Figure 1 shows beam currents of proton and deuteron beams measured by varying the magnetic field of the spin filter [1, 2]. The two peaks around 540 and 605 Gauss correspond to the resonances of the nuclear spin magnetic quantum number m_I = +1/2 and –1/2 for protons, respectively, and three peaks around 565, 575, and 585 Gauss correspond to those of m_I = +1, 0, and –1 for deuterons, respectively. Under the optimal condition, the beam current of polarized deuterons is approximately 40 nA, which is about seven times larger than that reported previously [11]. Furthermore, the resonance peaks of deuterons in Fig. 1 have become narrower than those reported previously [11]. The polarization of the polarized deuterons was ∼60% with a quenching method [2].
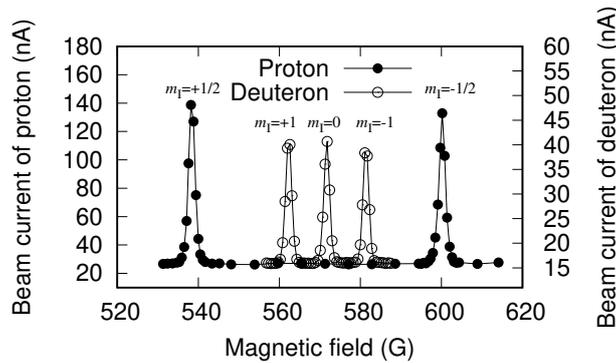
Fig. 1. Beam currents on the Faraday cup (FC-PIS) as a function of the magnetic field of the spin filter. Closed and open circles indicate beam currents of proton and deuteron, respectively.

For production of ^{20}F and observation of its NMR, polarized deuteron beams were accelerated up to 6 MeV by the 6MV Pelletron tandem accelerator, and transported to the A6 course. In this experiment, the transport rate from the FC-PIS to the Faraday cup of A6 course (FC-A6) was approximately 40%, and the beam current on FC-A6 was ∼13 nA. For both PIS and the beam transport line, optimized transport is necessary to reduce the beam loss. A CaF$_2$ stopper installed in the vacuum chamber of the A6 course was

irradiated with polarized deuteron beams to produce ^{20}F via the ^{19}F($\vec{d}$, p) reaction. β rays emitted from ^{20}F were detected by two sets of plastic scintillation counters placed above and below the stopper. Figure 2 (a) shows a typical β-ray time spectrum. By taking into account the lifetime of ^{20}F, the experimental data can be successfully fitted, as shown in Fig. 2 (a). From this result, the production of ^{20}F was confirmed using the polarized deuteron beams. Following this confirmation, we attempted to observe NMR of ^{20}F with the NMR system associated with β-rays (β-NMR system) [3]. The CaF$_2$ stopper surrounded by the RF coil was placed in the static magnetic field of 0.43 T. Recently, a variable condenser for tuning the resonance frequency was improved to be controlled remotely with a brushless motor and its driver (BLM230HP-GFV and BMUD30-A2, Oriental motor Co., Ltd.). Figure 2 (b) shows the asymmetry of the number of β rays counted by up and down plastic scintillation counters as a function of RF frequency. Considering the RF-Off level, the NMR peak has been successfully observed around 3.3 MHz, which is equal to the Larmor frequency of ^{20}F, corresponding to the nuclear magnetic moment of ^{20}F already reported [12]. From this result, we confirmed the polarization of ^{20}F using the polarized deuteron beams. In Ref. [13], we report the measurement of the sign of the magnetic moment for ^{20}F with the rotating magnetic field [6].

(a) (b)
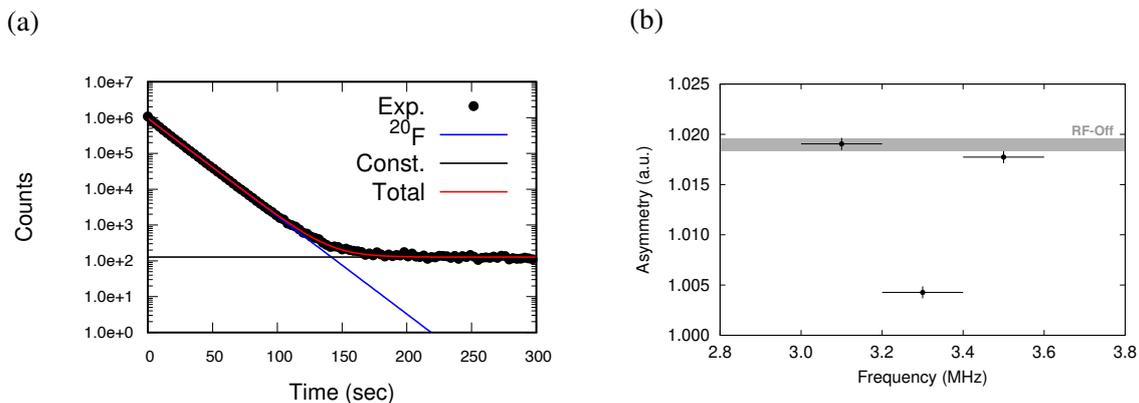
Fig. 2. (a) Typical β-ray time spectrum and (b) β-NMR effects of ^{20}F.

References

[1] Y. Tagishi et al., Nucl. Instr. Meth. 164 (1979) 411.

[2] T. Moriguchi et al., Proceedings of Science, PSTP2017 (2018) 018.

[3] A. Ozawa et al., UTTAC Annual Report 2017, UTTAC-87 (2018) 7.

[4] A. Ozawa et al., UTTAC Annual Report 2018, UTTAC-88 (2019) 7.

[5] A. Ozawa et al., UTTAC Annual Report 2019, UTTAC-89 (2020) 7.

[6] K. Tomita et al., UTTAC Annual Report 2019, UTTAC-89 (2020) 8.

[7] A. Ozawa et al., UTTAC Annual Report 2020, UTTAC-90 (2021) 7.

[8] A. Yano et al., UTTAC Annual Report 2020, UTTAC-90 (2021) 8.

[9] T. Moriguchi et al., UTTAC Annual Report 2020, UTTAC-90 (2021) 5.

[10] D. P. Burdette et al., Phys. Rev. C 99 (2019) 015501.

[11] T. Moriguchi et al., UTTAC Annual Report 2016, UTTAC-86 (2017) 3.

[12] N. J. Stone, At. Data Nucl. Data Tables 90 (2005) 75.

[13] A. Ozawa et al., this Annual Report 2.1.

2.3 Development of a position-sensitive detector using scintillating fibers

T. Yamaguchi[1,2], M. Kanda[2], H. Seki[2], N. Shinozaki[2], M. Otsu[2], Y. Koizumi[2], S. Matsuda[2], K. Okubo[2], K. Sasaki[2], S. Sugimoto[2], A. Yanai[2], T. Suzuki[2], T. Moriguchi, A. Ozawa, N. Kaname, A. Yano

We have been developing the Rare-RI Ring facility [1] at the RI Beam Factory in RIKEN for precision storage-ring mass spectrometry of short-lived exotic nuclei relevant to the astrophysics r-process scenario. Since the Rare-RI Ring is coupled with the cyclotron facility and hence individually stores a single ion of interest in-flight selected at the fragment separator, conventional beam diagnostic devices are often difficult to be employed. Besides, a long injection beam line is equipped to realize such a unique injection scheme. As such many beam diagnostics detectors, which can be easily operated and maintained and with a low cost, are required. We designed several shaped plastic scintillation detectors for position detection, and tested with swift heavy ions at the Heavy Ion Medical Accelerator in Chiba (HIMAC) facility [2] and with 12-MeV protons at the 6MV tandem accelerator at UTTAC. In particular, general versatility of the detector performance was examined with a low-energy beam.

In the previous annual reports in 2017 [3] and 2018 [4], we reported two kinds of position-sensitive detectors. The first case is a beam line detector, which consists of thin plastic scintillator bars (3 mm wide, 100 mm long, and 3 mm thick) vertically arranged to a flat plane (20 bars for 60×100 mm^2) and a common light guide connected to both ends. The scintillation photons are read out by four photo sensors at four corners: left-up (LU), left-down (LD), right-up (RU), and right-down (RD), through the common light guides. The time difference and pulse height difference of both ends were correlated well with the beam position. As a result, a position resolution of 1.7 mm (σ) in the y-direction was obtained at the HIMAC experiments [5].

To upgrade this detector, we use a simple plastic scintillator plate (100×100 mm^2 and 3 mm thick) instead of the bar array structure and three bundled wavelength shifters (each 1×1 mm^2, Kuraray Y-11) instead of one light guide, which is an easy and cheap solution, as shown in the inset photo in Fig. 1. For a 200-MeV/u Kr beam at the HIMAC facility, a position resolution of 1.2 mm (σ) in the y-direction was obtained from the pulse height difference. Figure 1 (left panel) shows a correlation plot of beam profile in the y-direction measured with PPAC [6] and that with the present detector, where a pulse height ratio is defined as $E_y = (Q_{LU} - Q_{LD} + Q_{RU} - Q_{RD})/(Q_{LU} + Q_{LD} + Q_{RU} + Q_{RD})$. Here, Q_i means an integrated charge measured with a charge-sensitive analog-to-digital converter, and the subscript i means each position of the photo sensors as described above. A linear relation in a wide range has been achieved. However, a large distortion in the x-direction was found, which needs to be improved. An experiment with a 12-MeV proton beam was conducted to investigate the detector performance. Figure 1 (right panel) shows a correlation plot of beam position in the y direction and the E_y ratio defined above. The beam position collimated to a 5-mm diameter was changed by moving the detector set up on a remotely-controlled movable platform. A linear correlation was confirmed, but a position resolution more than 10 mm was observed. We are currently improving the detector further.

As the second case, we produced a prototype of a long scintillating fiber detector to observe de-

---

[1]Cross appointment
[2]Department of Physics, Saitama University
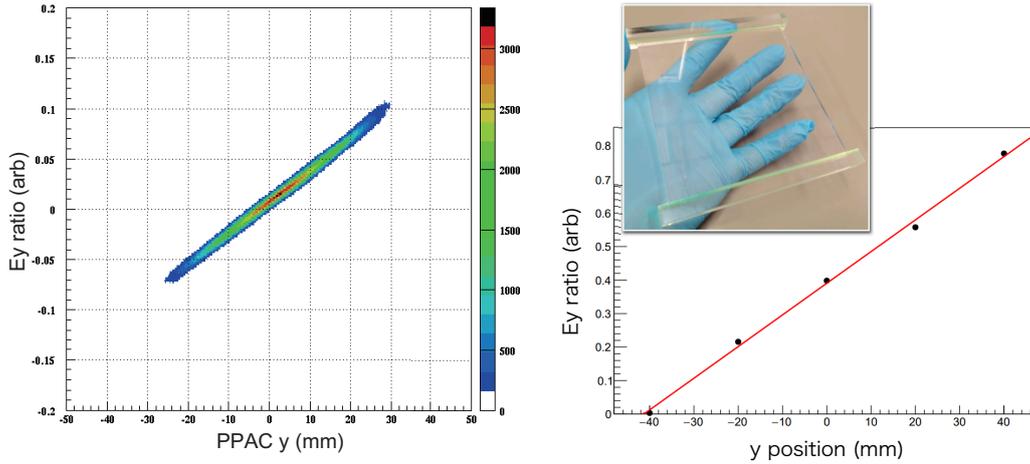
Fig. 1. Left: A two-dimensional correlation plot of the *y*-direction beam profile measured with PPAC and that with the present detector at HIMAC. A pulse height ratio, E_y, is well correlated to the beam position. Right: the same but with a 12-MeV proton beam at Tsukuba. The inset shows a photo of the present detector without photosensors.

cay particles of stored ions in the Rare-RI Ring. The detector will be installed in the vacuum chamber along the circumference of the storage ring. The original concept and results of experiments conducted at the HIMAC facility were published elsewhere [7]. The prototype consisting of nine scintillating fibers (Kuraray SCSF-78J, 2×2 mm^2 and 2 m long) was arranged to form a flat plane of 18 mm $\times$ 2 m. Each end of the nine scintillating fibers was assembled and connected to a common photo sensor. The results of the 12-MeV proton beam test show the position resolution of a few cm from the ratio $T_{\text{ratio}} = (T_{\text{left}} - T_{\text{right}})/(T_{\text{left}} + T_{\text{right}})$, where $T_{\text{left(right)}}$ indicates the timing of the left (right) photo sensor measured with a time-to-digital converter.

To upgrade this fiber detector, we use several plastic scintillator plates (100×39 mm^2 and 5 mm thick) and several wavelength shifters (WLS) for scintillation readout. The WLS are embedded on the back surface of the plastic plates. The advantage of the simple plate structure is to measure energy loss of decaying particles, which helps particle identification capability. A beam test with 12-MeV protons showed a position resolution of 5 cm, while that with 400-MeV/u Kr showed a position resolution of 5 mm, which is good enough to be applied at the Rare-RI Ring.

References

[1] A. Ozawa et al., Prog. Theo. Exp. Phys. 2012 (2012) 03C009.

[2] M. Kanazawa et al., Nucl. Phys. A 746 (2004) 393c.

[3] T. Yamaguchi et al., UTTAC Annual Report 2017, UTTAC-87 (2018) 9.

[4] T. Yamaguchi et al., UTTAC Annual Report 2018, UTTAC-88 (2019) 8.

[5] K. Wakayama et al., JPS Conf. Proc. 35 (2021) 011024.

[6] H. Kumagai et al., Nucl. Instrum. Methods Phys. Res. B 317 (2013) 717.

[7] K. Inomata et al., JPS Conf. Proc. 35 (2021) 011021.

2.4 Spin polarized ^{19}O beam produced through low energy nuclear reaction using inverse kinematics

M. Mihara[1], Y. Otani[1], Y. Kimura[1], T. Sugisaki[1], T. Moriguchi, A. Yano, K. Tomita, N. Kaname, A. Ozawa, H. Ishiyama[2], M. Fukutome[1], G. Takayama[1], R. Uda[1], H. Yuta[1], M. Fukuda[1], K. Matsuta[1]

Nuclear magnetic resonance (NMR) spectroscopy of oxygen is usually difficult to perform because of its low sensitivity due to very small natural abundance of ^{17}O (0.04%) which is the only nucleus with nonzero nuclear spin among the stable oxygen isotopes. As a new alternative method to ^{17}O NMR for materials science and other applications, we are attempting to use β-ray detected NMR (β-NMR) spectroscopy, which shows ultra-high sensitivity by using short-lived radioisotopes (RIs). In this study, ^{19}O (I = 5/2. $T_{1/2}$ = 16.9 s) which is a promising β-NMR probe nucleus was produced by a low-energy neutron transfer (d, p) reaction in inverse kinematics to provide a spin-polarized ^{19}O beam.

The experiment was continued since 2020 at the A7 course of the UTTAC facility using the apparatus shown in Fig. 1 [1]. An ^{18}O^{4+} beam with an energy of 30 MeV and an intensity of $100-200$ nA was provided by the 6MV tandem accelerator at UTTAC to irradiate a deuteron target. Deuterium-absorbed titanium foil TiD$_x$ with a thickness of 1 μm was used as the deuteron target, which was prepared by heating the Ti foil at 400 °C for about 75 minutes in a deuterium gas atmosphere with a pressure of about 220 Torr. The target was fixed to a Cu holder attached to a water-cooled flange and the beam was collimated by a Cu holder of 3 mm diameter. The target chamber was fixed to a rotating table so that only the direction of the vacuum duct could be changed while the target position was fixed. A welded bellows was used to connect the target chamber to the upstream beamline so that the target chamber can rotate freely.

^{19}O nuclei produced by the d(^{18}O, ^{19}O)p reaction were stopped in a single crystalline TiO$_2$ sample and spin polarization of ^{19}O was measured as a function of the emerging angle θ. For this measurement, an ultra-compact β-NMR spectrometer, which was newly fabricated for this study, was installed at the downstream side of the chamber. The performance of this instrument has already been confirmed using a spin-polarized ^{19}O beam at HIMAC in the Institute for Quantum Medical Science [2]. Polarization (P) of ^{19}O was obtained by measuring the β-ray asymmetry AP, where $A(= -0.7$ for ^{19}O) is the β-decay asymmetry parameter. The cycle of 40 s of the beam irradiation and 40 s of the β-ray measurement was repeated, and once in every two cycles, polarization was inverted via the adiabatic fast passage (AFP) by applying an RF magnetic field between the beam irradiation and measurement periods. β-rays were counted by counter telescopes placed at the top and bottom of the sample, respectively. Using the counting ratio $r_{\rm on}$ ($r_{\rm off}$) of these telescopes for the cycle with (without) RF, the β-ray asymmetry can be obtained by $AP = (\sqrt{R} - 1)/(\sqrt{R} + 1)$, where $R = r_{\rm off}/r_{\rm on}$.

Figure 2 shows the result of AP and β-ray yield of ^{19}O plotted as a function of θ, taken for both the left and right directions viewed from upstream of the beam. This indicates significant polarization with the absolute value of $|AP| \sim 2\%$ at around $\theta = 5.4°$, and when the angle is reversed from the left to right direction, the sign of AP is reversed from positive to negative. The present result is in very good agreement with the θ and AP values predicted from the previous result of ^{19}O polarization in forward kinematics [3].

[1]Department of Physics, Osaka University
[2]RIKEN Nishina Center for Accelerator-Based Science

The energy of ^{19}O emitted in the direction of $\theta = 5.4° \pm 0.4°$, where the polarization maximum was observed in the present study, is estimated to be (25 ± 2) MeV by the kinematics. This corresponds to about 15 μm in terms of range in Si.

Using the polarized ^{19}O beam with the above condition, we have measured the spin-lattice relaxation time of ^{19}O in Y_2O_3 stabilized ZrO_2 (YSZ) which is used as fuel cell materials, in order to study the property of oxide ion conduction [4]. In conclusion, it has been demonstrated that a polarized ^{19}O beam with nearly uniform energy can be obtained by using the low energy nuclear reaction in inverse kinematics, which is useful for materials science studies.
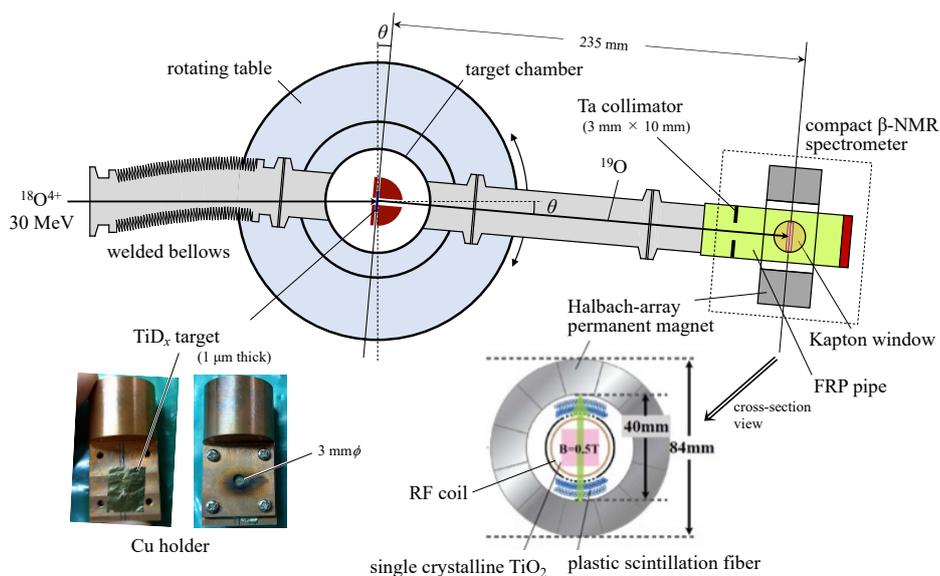
Fig. 1. Apparatus of the present experiment to measure ^{19}O polarization via the d(^{18}O, ^{19}O)p reaction.
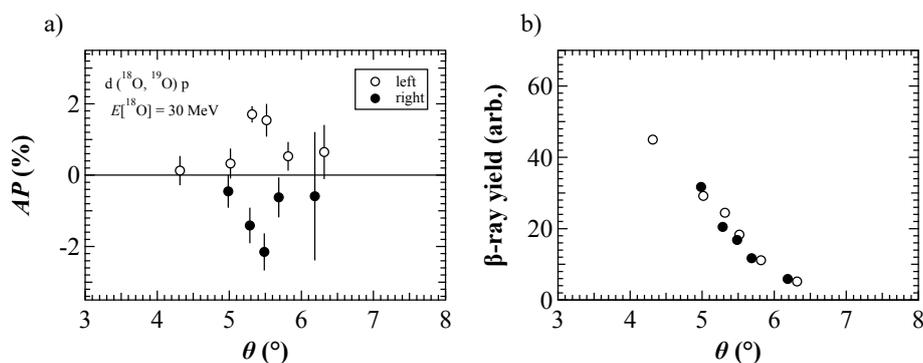
Fig. 2. a) β-ray asymmetry AP and b) β-ray yield of ^{19}O produced in the d(^{18}O, ^{19}O)p reaction measured as a function of the emerging angle θ. The left (right) indicates the case where the ^{19}O nuclei are emitted in the left (right) direction when viewed from the upstream of the beam. The sign of AP is defined positive in the vertical upward direction.

References

[1] M. Mihara et al., UTTAC Annual Report 2020, UTTAC-90 (2021) 10.

[2] Y. Kimura et al., Hyperfine Interactions 243 (2022) 1.

[3] K. Matsuta et al., Nucl. Instrum. Methods A 402 (1998) 229.

[4] Y. Otani et al., Hyperfine Interactions 242 (2021) 47.

2.5 Development of PIXE system using superconducting tunnel junction X-ray detectors

S. Shiki[1], S. Tomita, S. Ishii, S. Hatada, K. Sasa

Superconducting tunnel junction (STJ) detector is promising for soft X-ray spectroscopy due to its high sensitivity, high energy resolution, and high counting rate [1]. Particle Induced X-ray Emission equipped with superconducting tunnel junction detector array (SC-PIXE) will expand the energy coverage of PIXE into soft X-ray region where light elements are visible. The present paper reports the first measurement of photon using the SC-PIXE system which is set up in the μ-beam line at UTTAC [2].

The details of the experiments are as follows. The STJ spectrometer consists of a helium-3 cryostat, an STJ detector array of 512 pixels, 16-channel charge sensitive amplifier, multichannel analyzer having 16-inputs, and the μ-beam transport system. The temperature of the cold stage can be cooled down to approximately 320 mK. The beam current of proton was approximately 1 nA. The distance from the beam spot to the STJ detector was approximately 100 mm. The test sample was an aluminum plate.

Fig. 1. (a) Pulse height spectrum of an STJ pixel. (b) Pulse height spectrum of an STJ pixel after rejection of coincidence events to neighbor pixels.

Figure 1(a) shows a pulse height spectrum of an STJ pixel. We see two clear peaks at pulse heights of about 400 and 1500 on a broad continuum. These peaks are due to C-Kα and Al-Kα lines, respectively. The origin of the continuum might be protons which are scattered on the sample and absorbed by the Si substrate. A part of phonons generated by a proton create a pulse signal when the Cooper pair in the superconducting film of STJ pixel is broken by the phonons. Figure 1(b) shows a pulse height spectrum of the STJ pixel after rejection of the coincidence events of neighbor pixels. In this case, the peaks are seen without the background of broad continuum. The energy resolution of Al-Kα line is about 50 eV, which is better than that of high-quality semiconductor detectors. Continued research is needed to complete the SC-PIXE as a standard method of material analysis.
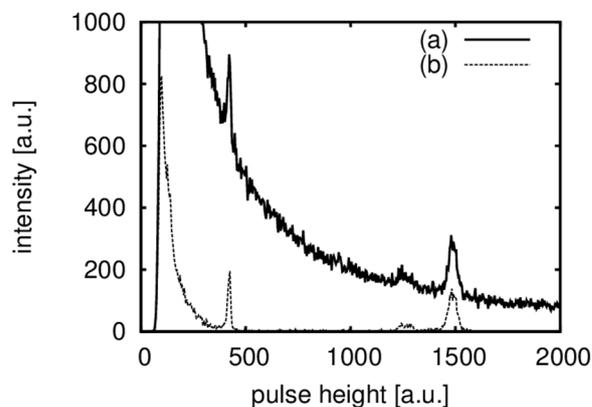
References

[1] S. Shiki et al., J. Low Temp. Phys. 167 (2012) 748.
[2] A. Yamazaki et al., Nucl. Instr. Meth. Phys. Res. B 404 (2017) 92.

---

[1] National Institute of Advanced Industrial Science and Technology

2.6 Measurement of convoy electrons produced by fast molecular ions in carbon foils

S. Tomita, M. Hiraga, S. Hatada, S. Ishii, T. Takahashi, K. Sasa, Y. Shiina[1]

The dynamic response of electrons in material caused by injection of fast molecular ions attracts certain attention because the response is related to the transport mechanism of the scattered electrons under interaction with the projectile ion. This leads to non-linear electron yield, which is called the cluster effect for molecular ion injections. We have investigated especially the yield of convoy electrons under injection of fast molecular ions [1, 2]. The convoy electron is the electron emitted in the same direction and with the same velocity as the projectile ions. The convoy electron yield $Y(C_n^+)$ shows a strong nonlinear effect of $Y(C_n^+) \propto n^2$ for 3.5 MeV/atom C_n^+ ions. To study the characteristic effect in the low-energy region. We have developed an apparatus of zero degree electron spectroscopy adapted to 1MV Tandetron at UTTAC.

The schematic drawing of the experimental setup is shown in Fig. 1. Ions accelerated with 1MV Tandetron were injected into the experimental chamber. The chamber was surrounded by a triaxial square Helmholtz coil to eliminate the Earth's magnetic filed [3]. The electrons produced by penetration of the ions in the foil were deflected by an electrostatic deflector, and the energy was analyzed with an electron spectrometer. The relative resolution of the spectrometer was 3.3%. The beam current of projectile ions passed through the electrostatic deflector was monitored by the Faraday cup located downstream of the beam line. Since the average charge of the transmitted ion depends on the thickness of the target foil as well as the cluster size of the projectile, we employed a beam-monitor system with Au bulk target. This target was fixed on the device with metronomic movement [4], thereby the incident beam crossed the Au target and the empty frame towards the foil target alternately. The amount of back-scattered ions were detected with SSD located at 150 degree to normalize the electron yield.

The measured electron energy spectrum is shown in Fig. 2 for incident ions of C^+ and C_2^+ with an energy of 437 keV/atom. The electron yield is normalized to the number of injected atoms. The peak located around
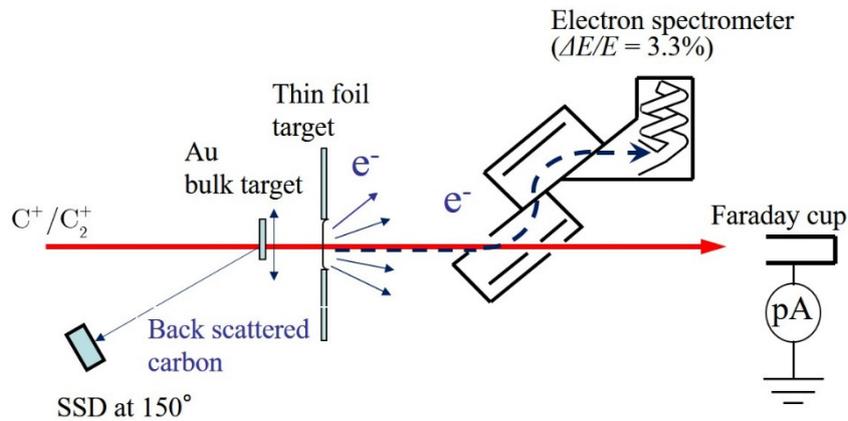
Fig. 1. Schematic drawing of the experimental setup.

[1] Rikkyo University

15 eV is due to convoy electrons, which have almost the same velocity as the 437 keV carbon ion. The amount of C_2^+ is twice that of C^+, as previously reported [1].
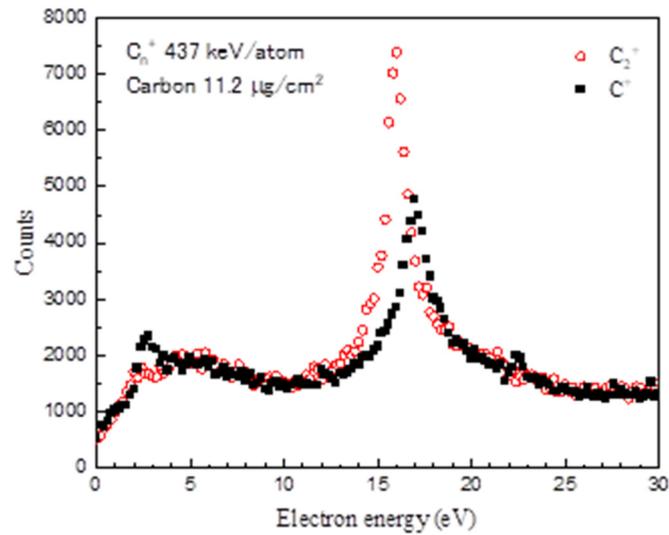
Fig. 2. Energy spectrum of zero-degree electrons emitted from a carbon foil of 11.2 µg/cm^2 in thickness.

References

[1] S. Tomita et al., Phys. Rev. A 73 (2006) 060901.

[2] Y. Shiina et al., Nucl. Instr. Meth. Phys. Res. B 460 (2019) 30.

[3] S. Tomita et al., UTTAC Annual Report 2020, UTTAC-90 (2021) 14.

[4] R. Ishiwari et al., Nucl. Instr. Meth. Phys. Res. B 47 (1990) 111.

3.

ACCELERATOR MASS SPECTROMETRY

3.1   Status report of the Tsukuba 6 MV multi-nuclide AMS system in FY2021

K. Sasa, T. Takahashi, M. Matsumura, D. Shiine, A. Sakaguchi, K. Sueki

The Tsukuba 6 MV multi-nuclide AMS system was operated for a total of 51 days and 530 hours in fiscal 2021. Figure 1 shows monthly-measured rare nuclides from April 2021 to March 2022. We measured 469 samples in total dealing with rare radionuclides such as ^{36}Cl and ^{129}I, as shown in Table 1.
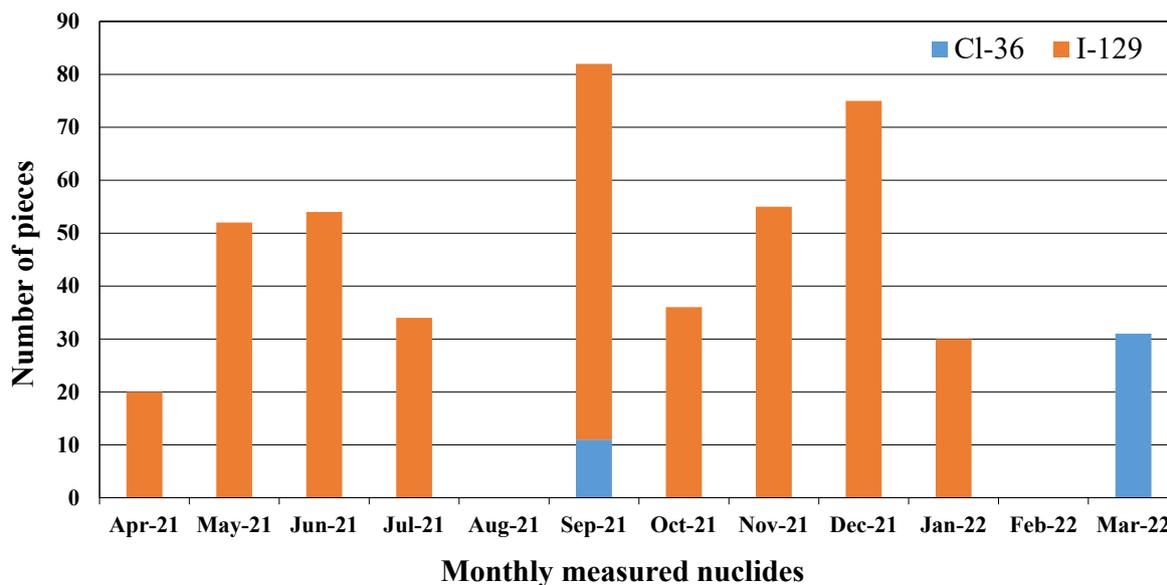
Fig. 1. Monthly-measured nuclides from April 2021 to March 2022.

Table 1. Number of measured ^{36}Cl and ^{129}I samples in fiscal 2021.

Item	Reagent & Blank samples	Standard samples	Unknown samples	Total
Cl-36	15	12	15	42
I-129	93	89	245	427
Sub total	108	101	260	469

^{36}Cl-AMS

^{36}Cl-AMS was applied for tracing cosmic ray events remaining in the ice-core in fiscal 2021 [1]. We have started analysis of Cl-36 in the relatively recent ice cores of the Antarctic H15 shallow core. The ^{36}Cl/Cl background and ice-core samples have been measured since fiscal 2021 under the beam condition of ^{36}Cl^{7+} with 48.0 MeV using a carbon foil stripper. The background ratios of ^{36}Cl/Cl $\sim 3 \times 10^{-15}$ were achieved with AgCl blank samples by using ^{36}Cl^{7+} [2].

^{129}I-AMS

^{129}I-AMS was mainly used for investigations of the radioactive contamination in surface soils, water samples, dissolved matters in the river at Fukushima and the tracer for oceanic circulation with a total of 245 unknown samples in fiscal 2021.

^{135}Cs-AMS

In recent years, development of a highly sensitive detection method for a long-half-life cesium-135 (Cs-135: half-life of 2.3 million years) has been required as one of the anthropogenic nuclides of the nuclear age. However, the Cs sputter negative ion source limits the analysis of cesium isotopes in AMS using a tandem accelerator. For this reason, we have started development of the rubidium (Rb) sputtering negative ion source by replacing Cs of the S-5 ion source (MCG-SNICS) with Rb. At present, the maximum $^{133}Cs^{19}F_2^{-}$ beam current of 0.2 μA was obtained from Cs_2SO_4 mixed with PbF_2. $^{133}Cs^{19}F_2^{-}$ was accelerated with a terminal voltage of 6 MV as a beam transport test. A beam transmission of $^{133}Cs^{9+}$ with an energy of 58.7 MeV was about 1.3%.

Measurement history
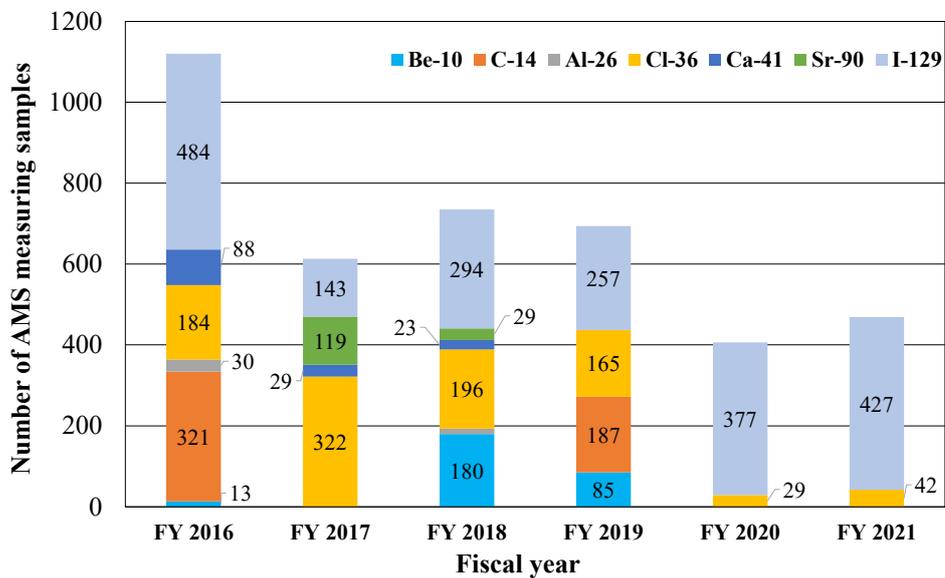
Fig. 2. Cumulative number of measured samples for AMS since 2016.

Figure 2 shows the cumulative number of measured samples since the AMS system started operation. A total of 4,037 samples was measured from 2016 to 2021.

References

[1] K. Kanzawa et al., JGR Space Physics 126 (2021) e2021JA029378.
[2] K. Sasa et al., UTTAC Annual Report 2019, UTTAC-89 (2020) 10.

3.2 Reconstruction of ^{129}I input history to the surface environment using a core from Beppu Bay

Z. Shi, A. Sakaguchi, K. Sasa, M. Matsumura, T. Takahashi, S. Yamasaki, K. Sueki

The Earth's environment has drastically changed by human activities in the past several decades. To describe this human age, scientists have proposed the setting of a new geological time scale, the Anthropocene. To define this new geological age, some candidate places for setting the Global Boundary Stratotype Section and Point (GSSP) have been raised and discussed in the international committee. Among the many identified candidate areas, Beppu Bay, Japan, is considered a very favourable candidate.

In this research, we focused on iodine-129 (^{129}I, $T_{1/2}$ = 15.7 Ma) which is the long-lived radioiodine. Anthropogenic ^{129}I is known to have been released to the environment by human nuclear activities such as nuclear bomb testing, nuclear fuel reprocessing, and nuclear accidents. Some of the previous research clarified ^{129}I input history to the surface environment using coral cores [1] and sediments of brackish lake and estuary [2, 3], thereby evidenced specific human nuclear activity. Thus, it is expected that ^{129}I becomes an important marker for the Anthropocene as a fingerprint of human activity if the reconstruction of the input history of ^{129}I can be achieved with the Beppu sediment samples. Eventually, the results obtained here will serve as an aid to set Beppu Bay as GSSP for the Anthropocene.

A sediment core sample (BMC19 S1-3) was collected from Beppu Bay (33°16'40.6"N, 131°32'35.2"E; 70.7m water depth), and cut into 1 cm segments from the sediment surface to 90cm depth. The sedimentation rate of this sediments was determined by caesium-137 (^{137}Cs) and lead-210 (^{210}Pb) methods [4]. Two procedures were conducted to determine the bulk stable iodine concentrations in each sediment layer. One is the TMAH (tetramethyl ammonium hydroxide) leaching method: the sediments were leached with 25% TMAH solution at 80°C for 12 hours. The other is the pyrohydrolytic procedure method: the sediments were calcinated at 990°C and the iodine released from sediments were trapped by mixed solution of 1% Na_2SO_3 and 1%TMAH. The concentrations of ^{127}I in leaching/trapping solutions were measured with Inductively Coupled Plasma Mass Spectrometer (ICP-MS, Agilent 7700) with ^{185}Re as an internal standard solution.

For analysis of ^{129}I/^{127}I, iodine was collected by the pyrohydrolytic procedure, and was chemically purified by solvent extraction and back extraction methods. Finally, iodine was collected as AgI precipitates by adding AgNO$_3$ solution to an aqueous solution. Dried AgI was mixed with Nb (AgI:Nb=1:4 in mass ratio), which is an ionization supporter for iodine, and measured ^{129}I/^{127}I ratios with Accelerator Mass Spectrometry (AMS) at UTTAC. By comparison between the concentrations of ^{127}I obtained by the two methods (TMAH leaching and pyrohydrolytic procedure), the higher
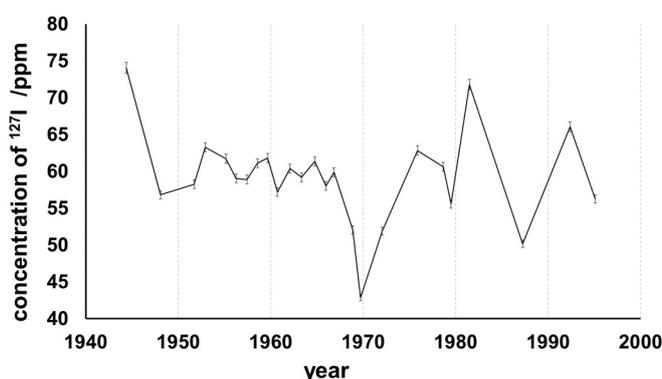
Fig. 1. Concentration of ^{127}I in sediments from Beppu Bay in the period 1944–1995.

concentrations of [127]I were employed as the bulk concentration of stable iodine (Fig. 1) considering the cumbersome method and complex composition of marine sediments with contributions of organic and inorganic iodine precipitations. The concentration of [127]I lies in the range of 40-75 ppm with an average of 59.2 ppm, which is in line with the general range of iodine concentration in the oceanic sediment.[127]I concentrations are uniform around 1948-1967, and then decrease in 1970 sharply. The [127]I concentrations fluctuate more after 1970, but any significant trend could not be seen over years.

Atom ratios of [129]I/[127]I in sediments from Beppu Bay vary from 5.07×10^{-13} to 1.11×10^{-10} over analysis years (Fig. 2). The atom ratio of [129]I/[127]I increases from 1944 to 1948 but decreases slightly around 1953. The ratio gradually increases with prominent peaks at 1958, 1969 and 1975. Then the ratio slightly decreases and keep higher values in 1980s and 1990s compared with those before 1970. The rough trend of [129]I/[127]I ratios through the 1940s to the present, i.e., gradual increase of the ratio over the years,
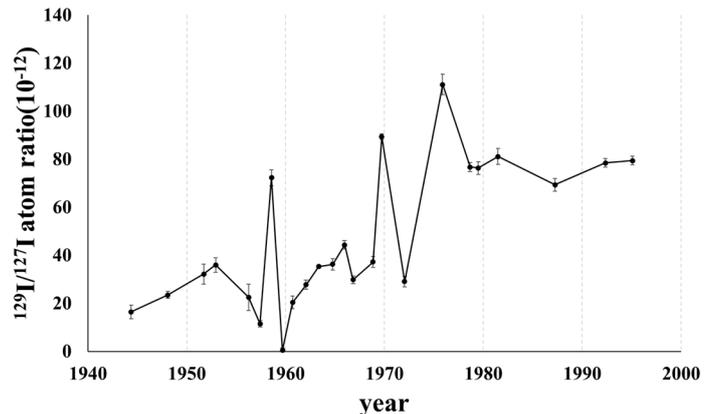
Fig. 2. Atom ratio of [129]I/[127]I in Beppu Bay sediments in the period 1944–1995.

is similar to those of marine sediments from Jiaozhou Bay, China [5] and the coral core sample from the Japan Sea [1]. However, significant signals such as the maximum nuclear testing, hydrogen bombing, Chernobyl accident were not clearly found in the core from Beppu Bay. These are due to the complex composition of the sediments and the unclear sedimentation process of iodine in the Beppu Bay system.

The variation of iodine isotopes might reflect the human nuclear activity somehow, although the records are not so clear as the result from coral samples. Thus, when the iodine isotope composition is used as a marker for the Anthropocene definition, the behaviours of both terrigenous and authigenic iodine following the surrounding environmental changes must be well considered.

References

[1] A. Sakaguchi et al., Mar. Environ. Res. 142 (2018) 91.

[2] Y. Ishiga et al., Geoscience Rept. Shimane Univ. 36 (2018) 39.

[3] Y. Satoh et al., J. Radioanal. Nucl. Chem. 322 (2019) 2019.

[4] S. Takahashi et al., Sci. Total Environ. 743 (2020) 140767.

[5] Y. Fan et al., J. Environ. Radioactiv. 154 (2016) 15.

3.3 Development of a measurement technique for ^{135}Cs as a new oceanic circulation tracer

D. Shiine, A. Sakaguchi, K. Sasa, T. Takahashi, M. Matsumura, S. Yamasaki, K. Sueki

Cesium-135 (^{135}Cs, $T_{1/2}$=1.33 million years) is an important nuclide that requires monitoring in waste-related samples and environmental impact assessment because of its long-term persistence in radioactive waste. On the other hand, it is expected to have a potential as a geochemical tool/tracer for seawater circulation, which can identify the origin of water masses, and for other geoscientific applications by utilizing it together with short-lived ^{137}Cs. However, there are some problems especially in the analysis of ultra-trace amounts of ^{135}Cs in seawater by mass spectrometry, (1) the measurement of ^{135}Cs using accelerator mass spectrometry, which is considered to be the most promising method for the ultra-trace measurement, is limited because of severe interference by isobar ^{135}Ba in addition to use ^{133}Cs as a sputter ion source, (2) a large amount of ^{133}Cs carrier, which will interfere with mass spectrometry, should be added to seawater when the conventional Cs concentration method 'ammonium phosphomolybdate coprecipitation (AMP)' is employed [1], and this AMP is in powder form making it difficult to handle particularly on board, and (3) AMS analysis requires that the analyte should be extracted as a negative ion beam from solid samples, but Cs compounds that can extract Cs as a negative ion are unknown, since Cs tends to be a positive ion. In order to solve these problems, the following studies were conducted to measure Cs isotopes by AMS and the concentration of Cs from seawater.

Rubidium (Rb), which has similar physicochemical properties to Cs, was used as a sputter ion to replace Cs, and a new Rb ion source was established. By sputtering some kinds of Cs reagents with Rb, we investigated whether Cs in the sample can be extracted by Rb ions. Actually, we examined the speciation of the negative ion beam of Cs extracted from the sample. In the experiments, Cs_2SO_4, $CsNO_3$, Cs_2CO_3, $CsBr$, CsI and mixtures of PbF_2 with these Cs reagents were used to extract Cs as a fluoride beam [2]. Further, the current intensity of the Cs beam was increased by optimizing the oven temperature and the ionizer in the Rb ion source. By introducing the beam into the final ionization chamber, signals of nuclides with a mass number of 135 were measured.

The adsorption rates of ^{137}Cs and ^{133}Ba added to seawater were investigated using copper-substituted Prussian blue non-woven fabric [3] (hereafter referred to as "PB") by a batch method. After the adsorption experiments, the PBs were leached with several concentrations of hydrochloric acid and nitric acid to find the optimum conditions for Cs desorption from the PB.

Current intensities more than 10 nA were
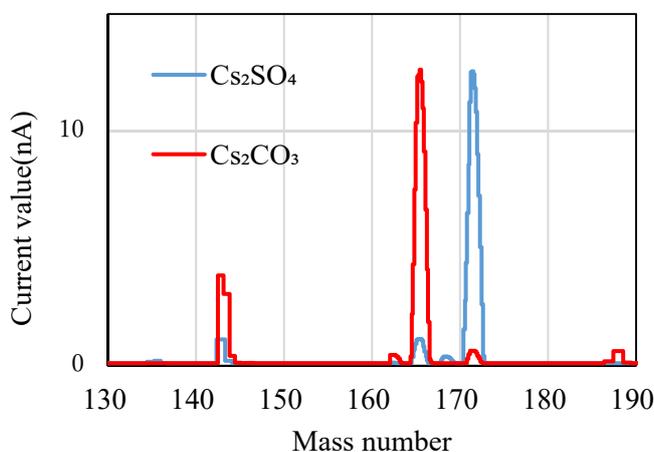
Fig. 1. Mass spectra of ion beams extracted from Cs_2SO_4+PbF_2 and Cs_2CO_3+PbF_2.

found for CsO_2^- and CsF_2^- beams from Cs_2SO_4 and Cs_2CO_3 mixed with PbF_2 sputtered by Rb (Fig. 1). Considering the preparation and stability of the sample, Cs_2SO_4+PbF_2 is expected to be used as an AMS sample in the future. In addition, an accelerated beam of CsF_2^- obtained from Cs_2SO_4+PbF_2 allows extraction of multiply charged Cs ions. Thus, it can be concluded that the Rb ion source actually succeeded in extracting Cs from the sample. The spectrum with a mass number 135 was also confirmed by the final detector after optimizing the oven temperature and ionizer current value (Fig. 2).

The Cs adsorption rates with 0.92-46.0 µmol of PB for 1 kg of seawater were 20.2-95.8% (Fig. 3). Therefore, about 46 µmol of PB per 1 kg of seawater is required to efficiently adsorb Cs. On the other hand, the adsorption rates of Ba, which is an interference element in mass spectrometry, was less than 5.3% for all sizes of adsorbents, indicating that it is relatively difficult to adsorb Ba on the PB. In the desorption experiment, 97.2 ± 2.6% of Cs desorption was found in 35% HCl.
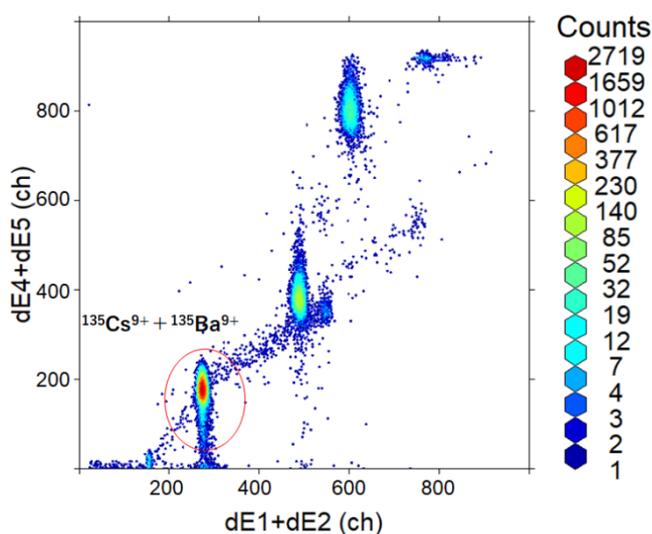
Fig. 2. 2D spectrum showing the unresolved peak of $^{135}Cs^{9+}$ and $^{135}Ba^{9+}$.
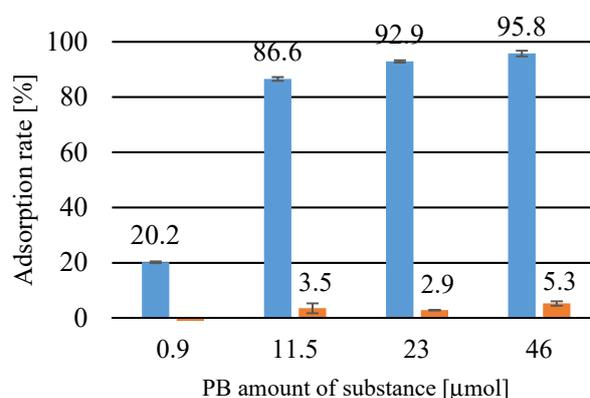
Fig. 3. Cs and Ba adsorption rates on PB.

References

[1] M. Aoyama et al., Appl. Radiat. Iso. 53 (2000) 159.

[2] J. Eliades et al., Nucl. Instr. Meth. Meth. Phys. B 294 (2018) 361.

[3] T. Yasutaka et al., J. Nucl. Sci. Tech. 53 (2016) 1243.

3.4 The performance of iodine-129 AMS measurements at the University of Tsukuba (FY 2021).

M. Matsumura, K. Sasa, T. Takahashi, A. Sakaguchi, T. Matsunaka[1], K. Sueki

Continuing from 2017, we have reported that the performance of ^{129}I measurements by accelerator mass spectrometry (AMS) for the development of the standard reference materials (STD) of ^{129}I in the near future. Details of the ^{129}I AMS measurements are described in the references [1-2].

From April 2021 to March 2022, we measured 427 samples of ^{129}I, the details of which are shown in Fig. 1. The test samples were chosen from natural environment such as sea, rain, river water, and sediments. Figure 2 shows the measured values of carrier-reagent blanks. The machine background is estimated to be on the order of 10^{-15} in the ^{129}I/^{127}I ratio, which is sufficiently lower than the background level of the ratio of 2×10^{-14} for "Old Iodine" provided from Deep Water company, USA. However, sometimes, the measured ^{129}I/^{127}I values in blanks ranged over ten times higher than 2×10^{-14}. One of the causes for this might be the memory effect. The rise in blank values in 2018 and 2019 is most likely caused by this memory effect, however, the memory effect has been prevented by measurement schemes since 2020.
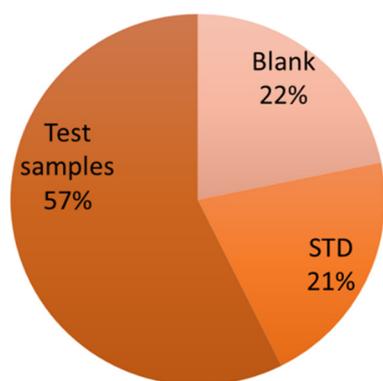
Fig. 1. Details of measured ^{129}I by the AMS system in fiscal 2021.
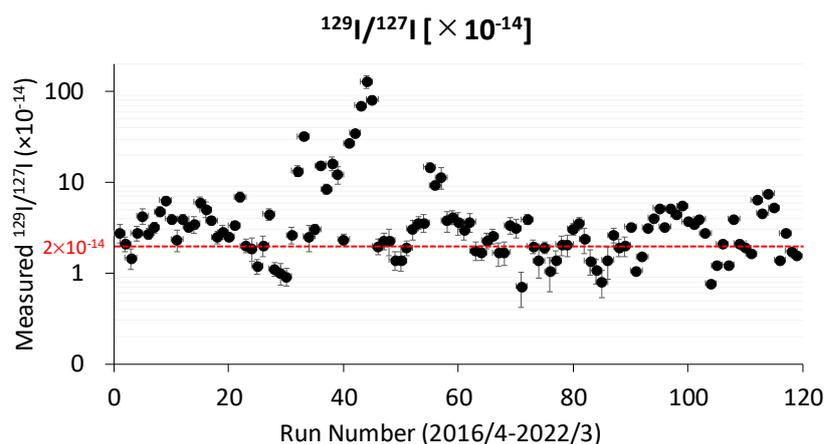
Fig. 2. ^{129}I/^{127}I ratios in blanks.

We have measured the certified materials since 2020. The results of measurement for Standard Reference Material® 3230, Level I and Level II, provided from the National Institute of Standards and Technology (NIST, USA) are shown in Fig. 3. They were normalized by using Purdue-2 STD (Z94-0596) with an ^{129}I/^{127}I ratio of 6.54×10^{-11} [3] (the value was revised in 2014 [4]), which was provided by the Purdue Rare Isotope Measurement Laboratory (PRIME Lab) at Purdue University, USA. The nominal ^{129}I/^{127}I ratios are $(4.920 \pm 0.062) \times 10^{-10}$ and $(0.985 \pm 0.012) \times 10^{-12}$, for NIST 3230- Level I and Level II, respectively. The two samples after sputter-cleaning for 1 or 5 min. were measured in each run. The measured values of Level I are approximately 10% lower than the nominal one. The resulting ratio and standard deviation (1σ) of the precision are $(4.362 \pm 0.048) \times 10^{-10}$ (1.1%) and $(0.918 \pm 0.070) \times 10^{-12}$ (7.6%), respectively.

---

[1] Kanazawa University
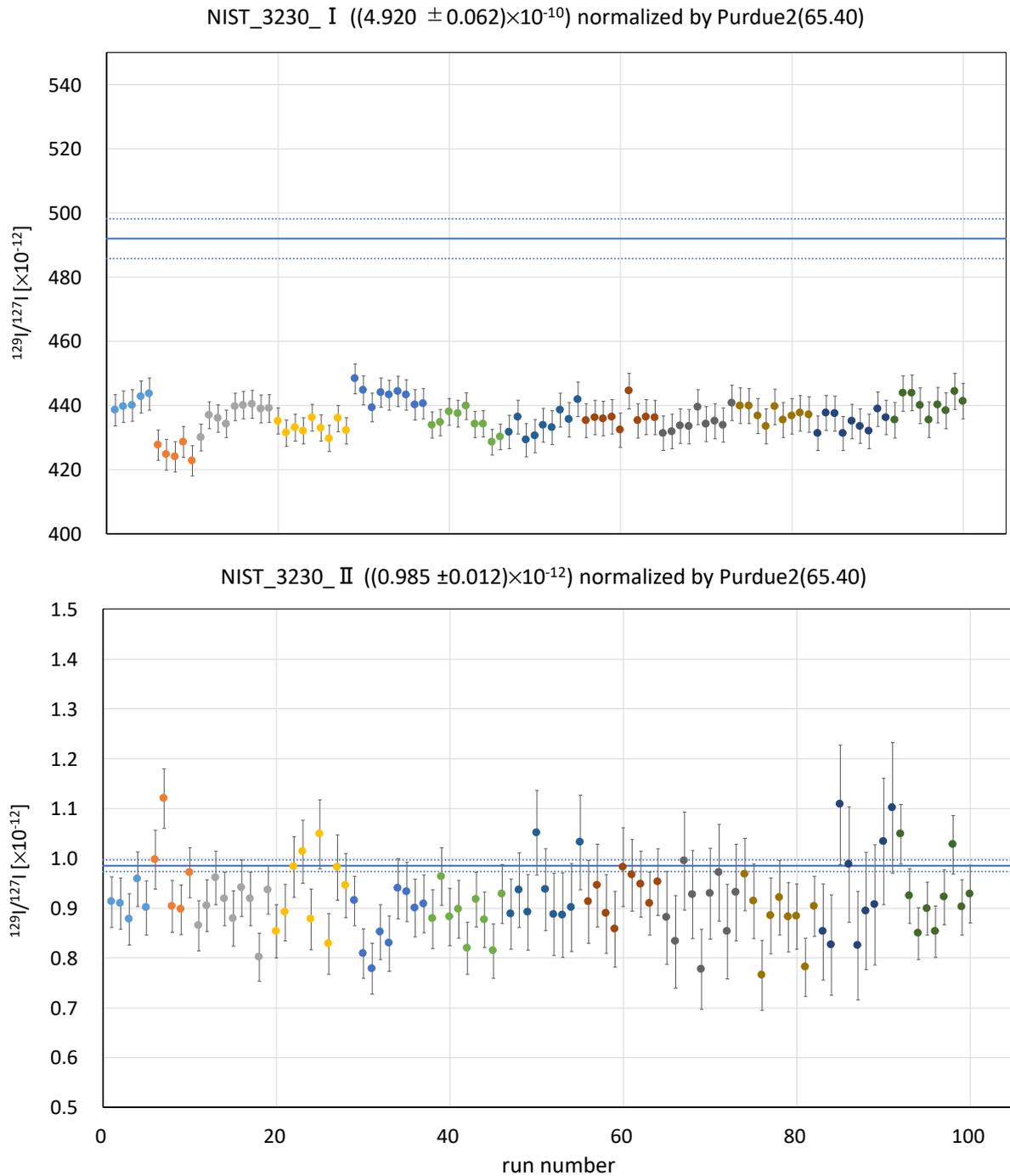
Fig. 3. Measured ^{129}I/^{127}I ratios of NIST 3230-STD. The error bars attached to all measured points represent counting statistics. The dots of the same color correspond to the same target.

References

[1] K. Sasa et al., Nucl. Instrum. Meth. Phys. Res. B 437 (2018) 98.

[2] M. Matsumura et al., UTTAC Annual Report 2019, UTTAC-89 (2020) 16.

[3] P. Sharma et al., Nucl. Instrum. Meth. Phys. Res. B 123 (1997) 347.

[4] M. Caffee, (Purdue University), Private communication (2014).

3.5 Vertical distribution and temporal changes of ^{129}I in soil derived from the Fukushima Daiichi Nuclear Power Plant accident

Y. Gao, A. Sakaguchi, K. Sasa, M. Matsumura, T. Takahashi, Y. Ota, K. Sueki

Studies related to the Fukushima Dai-ichi Nuclear Power Plant (FDNPP) accident reported depth profiles of ^{129}I at upland field, empty lot, and ground level in Fukushima [1]. Also, the workers reported observations of changes in depth distribution of one sampling point for less than a year [2].

To clarify the long-term migration behavior of ^{129}I, depth profiles of ^{129}I in soil at the same site in the vicinity of FDNPP have been evaluated over a long period of time from 2 to 10 years after the accident. From the measured depth profiles of ^{129}I in the soil, (i) the downward mobility of ^{129}I derived from FDNPP was estimated, and (ii) the behavior of ^{129}I in the soil were analyzed using a diffusion model. Further, we attempted to predict the amount of ^{129}I in the soil in the next 100 years by using a diffusion model. Cs-137 in the same soil samples was also analyzed to compare the differences in the migration processes of these elements.

About 30-cm-long soil cores were collected from Namie-machi, Fukushima on June 12, 2013, June 17, 2016, September 10, 2017 and November 6, 2020. These samples were cut into 1−4 cm segments from the surface of the core. Each sample was freeze-dried and homogenized [3].

Iodine in soil was extracted by the pyrohydrolysis method, and was purified by solvent extraction/back extraction method. Finally, the iodine was precipitated as AgI for AMS [4]. The ^{129}I/^{127}I ratio was measured by the AMS system at UTTAC. The ^{127}I concentration in the trapped solvent obtained by pyrohydrolysis was measured with the Inductively Coupled Plasma-Mass Spectrometer (ICP-MS, Agilent 8800). The amounts of ^{129}I in the soil cores were calculated using ^{127}I concentrations obtained from ICP-MS and ^{129}I/^{127}I ratios obtained from AMS.

The depth profiles of ^{129}I obtained over the years show that the concentrations of ^{129}I derived from the FDNPP decrease with increasing depth from the surface [5]. More than 80% of the ^{129}I inventory is accumulated in surface layers (less than 2.5 g/cm^2 in mass depth). Thus most of the accident-derived ^{129}I is accumulated in the surface soils. By applying the one-dimensional (1D) diffusion model from the ICRU report, the expectation mass depth α (g/cm^2), which represents the migration of ^{129}I and ^{137}Cs during the observation period, is calculated. The results are shown in Table 1 and also in Fig. 1.

Table 1. Expectation mass depths (g/cm^2) of ^{129}I and ^{137}Cs during the observation period.

Date of soil core collection	Expectation mass depth of ^{137}Cs (g/cm^2)	Expectation mass depth of ^{129}I (g/cm^2)
2013/6/12	0.88	0.91
2016/6/17	0.77	1.19
2017/9/10	1.27	1.74
2020/11/6	1.23	1.40
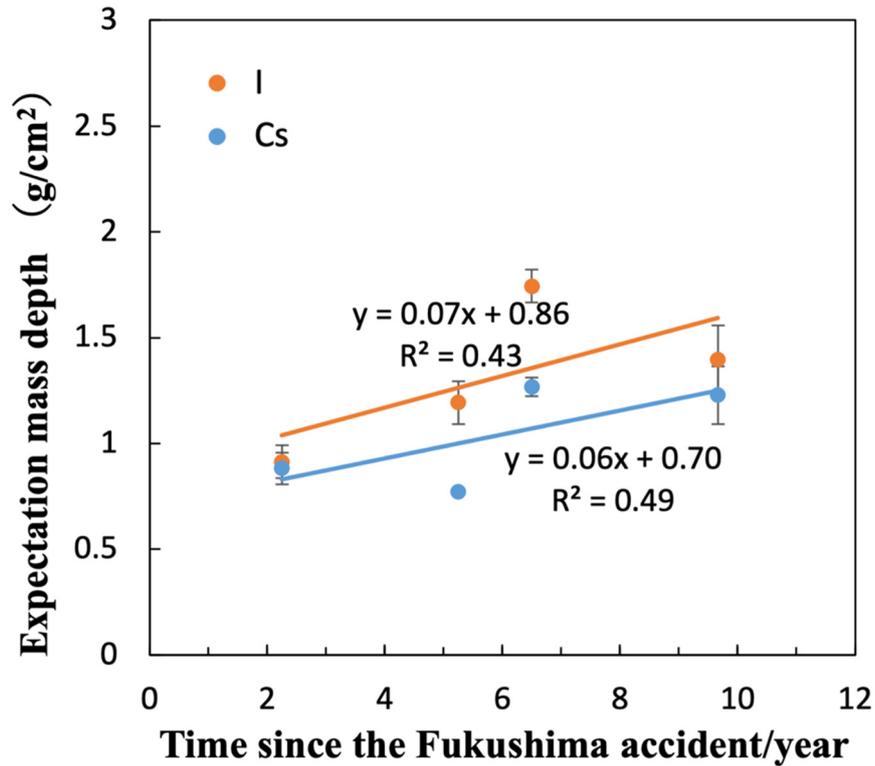
Fig. 1. Expectation mass depth of ^{129}I and ^{137}Cs over the years since the FDNPP accident, determined by applying the 1D diffusion model.

From Fig. 1, the downward migration rates of accident-derived ^{129}I and ^{137}Cs were determined to be 0.07 g/cm^2/yr and 0.06 g/cm^2/yr, respectively. There appears to be a difference between the two in the expectation mass depths, but not in the downward migration rates. It may be predicted from the present results that the expectation mass depth of FDNPP accident-derived ^{129}I in 100 years would be about 8 g/cm^2 (about 8 ~ 9 cm depth), indicating that ^{129}I may continue to remain relatively in the surface layer.

References

[1] M. Honda et al., Applied Geochem. 85 (2017) 169.

[2] M. Honda et al., J. Environ. Radioact. 146 (2015) 35.

[3] Y. Ota et al., UTTAC Annual Report 2018, UTTAC-88 (2019) 21.

[4] Y. Muramatsu et al., Quat. Geochronol. 3 (2008) 291.

[5] Y. Gao et al., UTTAC Annual Report 2020, UTTAC-90 (2021) 24.

3.6   Surface distribution of iodine-129 in the Arctic Ocean

T. Matsunaka[1], S. Nagao[1], M. Inoue[1], Y. Kumamoto[2], T. Takahashi, M. Matsumura, K. Sueki, K. Sasa

Over the last several decades, Arctic river discharge from several countries increased, conveying heat and freshwater into the Arctic Ocean, and resulting in the decline of Arctic sea ice [1]. The investigation of water dynamics change in the Arctic Ocean caused by the recent global warming is essential for forecasting the response of ocean circulation with climate change. Anthropogenic ^{129}I ($T_{1/2}$ = 15.7 million years) produced from the thermal neutron fission, is dominated by release from nuclear fuel reprocessing plants in the Europe and is supplied at the Arctic Ocean via atmospheric deposition, surface runoff, and sea currents. To illuminate the availability of ^{129}I as a tracer of surface circulation in the Arctic Ocean, we investigated the horizontal distribution of ^{129}I in 2019.

The dissolved ^{129}I in surface water in the Arctic Ocean, Bering Sea, and North Pacific Ocean varies from 13.6±0.9 to 250±4.2 nBq L^{-1}, and is negatively correlated with water temperature (Fig. 1A, R^2 = 0.74) and salinity (Fig. 1B, R^2 = 0.85). This water temperature and salinity-dependent distributions reveal that the dissolved ^{129}I in the Arctic Ocean is controlled by mixing of water mass from the Arctic Ocean surface mixed layer water with cold and lower salinity and the Alaskan Coastal Water from Bering Sea with warm and higher salinity. ^{129}I is considered to be a tracer for the front of the Arctic Ocean surface mixed layer water influenced by the freshwater input.
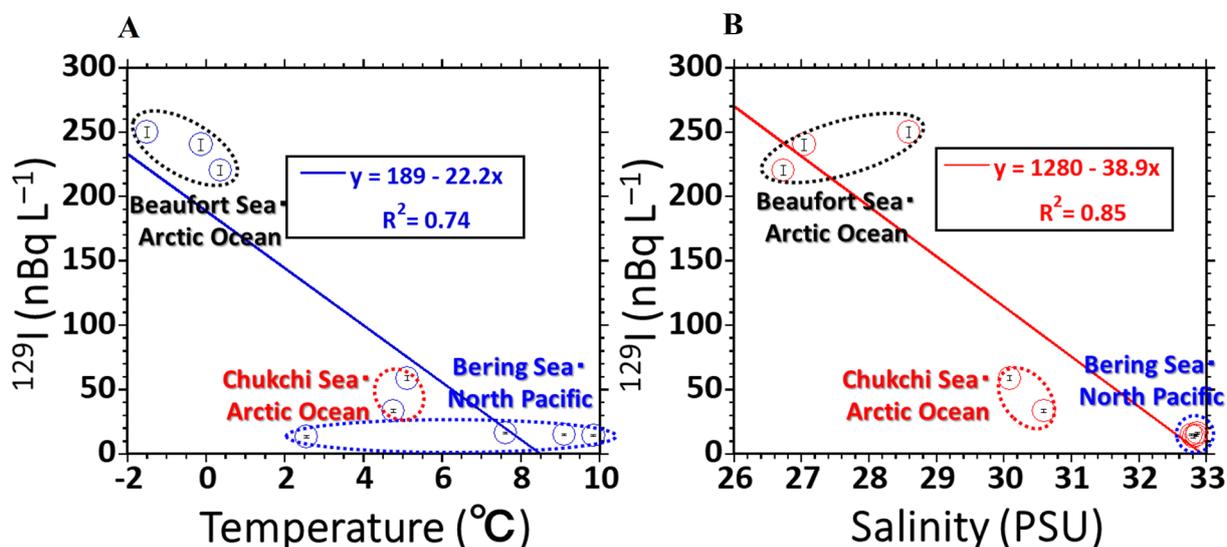
Fig. 1. The correlations between ^{129}I activities in surface seawater and (A) water temperature, and (B) salinity in the Arctic Ocean, Bering Sea, and North Pacific Ocean in 2019. The linear regression lines and coefficients of determination (R^2) are shown in the correlation diagrams.

Reference

[1] H. Park et al., Science Advances 6 (2020) 4699.

---

[1] Kanazawa University
[2] JAMSTEC

4.

ION-BEAM APPLICATIONS

An engineer making experimental items using a grinder

4.1 Composition analysis of particles released from the FDNPP using microbeam scanning PIXE

K. Sueki, T. Nakamura, S. Ishii, K. Sasa, S. Tomita

Among the radioactive substances released from the Fukushima Daiichi Nuclear Power Plant (FDNPP) in the March 2011 accident, the particulate matter called radioactive particle that is highly contaminated with radioactive cesium has been found [1]. We have reported on the composition of radioactive particles that have been found so far by quantitative analysis of the main components and by elemental mapping of silica glass particles. The main components of the sample T47 whose surface was polished were analyzed by PIXE using a microbeam of 2 MeV protons and a Si(Li) detector, from which we were able to detect Sr that could not be observed by SEM-EDS analysis until now [2]. The scanning analysis with a 4 MeV proton microbeam from the 6MV tandem accelerator was carried out using a CdTe detector, thereby the authors succeeded in obtaining elemental mapping of Sr and Pb [3].

In the present work, we compared the information obtained by elemental mapping of non-processed radioactive particles with that obtained by detectors of different type and by SEM/EDS. We also measured not only the particles of silica glass, but also the particles mainly composed of iron oxide, and also the particles in which iron oxide and siliceous glass are mixed, similar to the measured radioactive particles. The data collected with two types of detectors, a CdTe detector and a silicon drift detector (SDD) were used. The data obtained by SDD can be compared with SEM-EDS. The beam current was maintained at several pA for a beam size of 8 μm square in consideration of sufficient X-ray intensity. It was possible to collimate the beam size to 1-2 μm square, but at that time the intensity was much lower than 1 pA and practical measurement was not possible. The measured four samples, T47, R008, Y04, and Y06, which were taken out of the environments except for T47 and were not processed at all.

Figure 1 shows the X-ray spectra measured for the narrow (for T47, R008, Y04, and Y06) and wide (for T47, R008, and Y06) energy ranges using SDD and the CdTe detector, respectively. The spectra for R008 and T47 are very similar, but the intensity of K X-ray from Ba at ~34 keV is obviously higher for R008 than for T47. In this case, the X-ray yield was not enough to take an elemental map. It was found from SEM/EDS observation that Y06 was in such a situation where siliceous glass was attached to a piece of iron oxide and, as a result, Si, Fe and Zn were strongly observed in the spectrum, while Pb, Sr and other heavy elements were not observed. Y04 is also considered to be an oxide of iron, but the composition is different from that of Y06 since both Fe and Si are observed in the whole particle.

Figure 2 shows a comparison of the elemental maps for Y06 by PIXE with those by SEM/EDS. It is noticeable that Fe is observed with a considerable intensity in the map-i even where Si is rich, whereas it is hardly visible in the map-b. This is because 4 MeV protons reach a depth of several tens of μm from the surface, while SEM/EDS can only observe X-rays from the surface layer of 1 μm thickness or less.

Observing particles with complicated shapes without processing causes problems in quantification, but the present work has shown a possibility that new findings can be obtained by using them so as to complement SEM/EDS in element mapping.
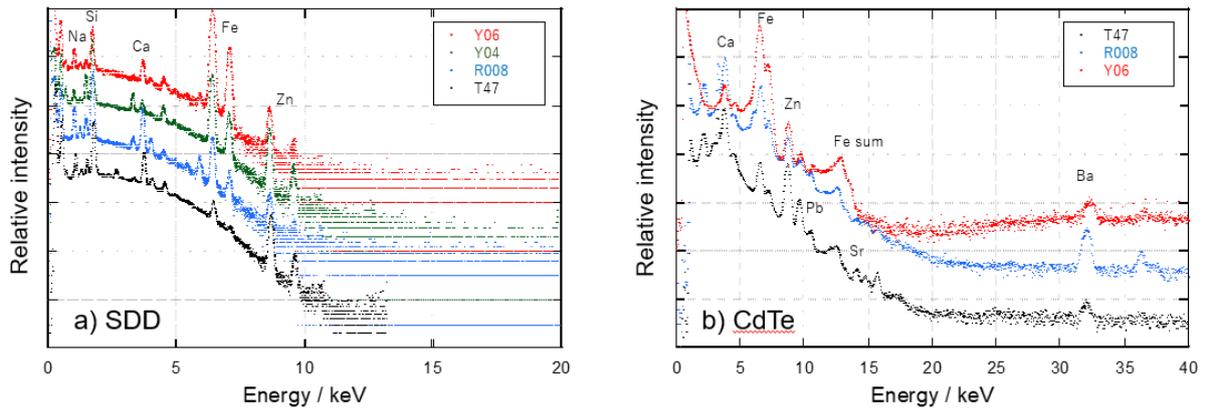
Fig. 1. PIXE spectra of radioactive particles measured with (a) the silicon drift detector and (b) the CdTe detector.
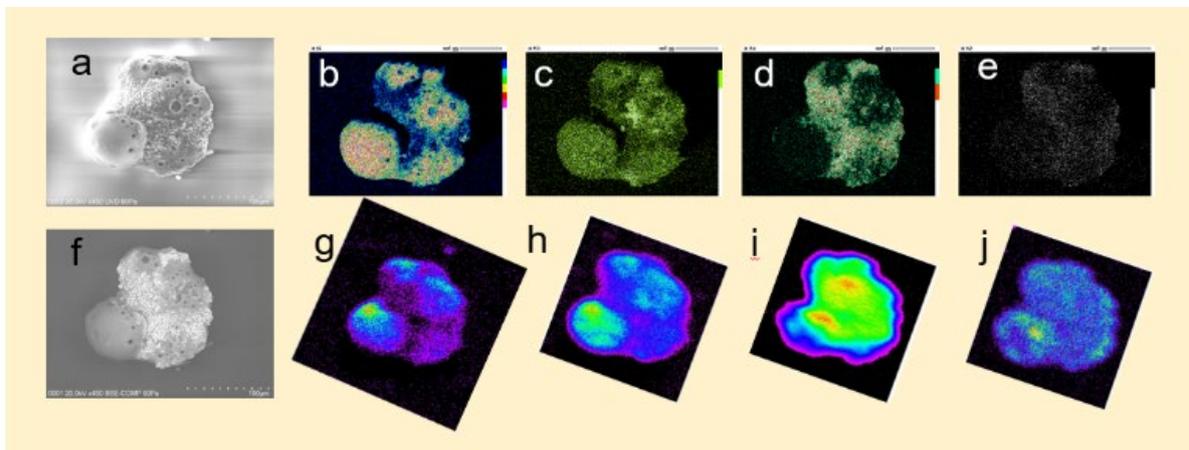
Fig. 2. SEM images and elemental maps of the radioactive particle Y06. a: SEM image, b–e: SEM/EDS elemental maps, f: backscattered electron image and g–j: PIXE elemental maps. Maps b and g for Si, c and h for Ca, d and i for Fe, e and j for Zn. The map-g was measured by SDD and h– j were observed by the CdTe detector.

References

[1] Y. Satou et al., Geochem. J. 52 (2018) 137.
[2] M. Kurosawa et al., UTTAC Annual Report 2018, UTTAC-88 (2019) 31.
[3] K. Sueki et al., UTTAC Annual Report 2020, UTTAC-90 (2021) 28.

4.2   Determination of H concentration in solids by T-ERDA

H. Kudo, M. Kurosawa, H. Naramoto, M. Sataka, S. Ishii, K. Sasa, S. Tomita

It is of practical interest to establish transmission ERDA (T-ERDA) as a standard technique of quantitative hydrogen analysis, considering open use of this technique in future at UTTAC not only by internal, but also by external users.   For this purpose, we have carried out T-ERDA using well-characterized samples of polyphenylene sulfide (PPS) and natural muscovite [1]. Figure 1 shows the experimental setup which has been optimized for the quantitative H analysis, compared with the previous cases [2, 3].
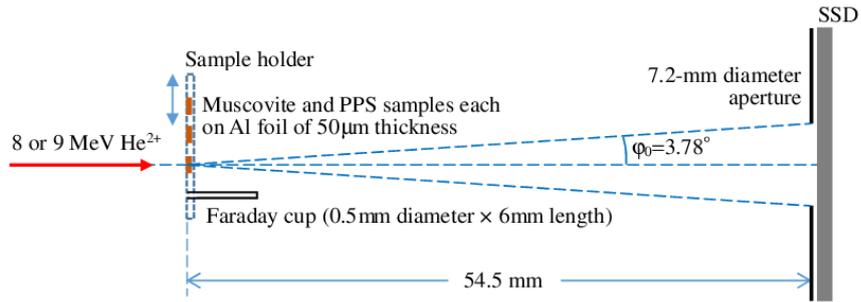
Fig. 1. Schematic diagram of the experimental setup for T-ERDA.

The PPS samples are stacked layers of 1.35-µm thick PPS and Al foils, which were used in the previous work [3]. The muscovite sample of ~12 µm thickness was prepared by cleaving the bulk muscovite which was collected from a granitic pegmatite rock at Ishikawa, Fukushima Prefecture. These samples were fixed on the Al foil of 50 µm thickness to prevent the incident He from entering the particle detector. Figures 2 and 3 show energy spectra of recoil H measured with SSD in Fig. 1.
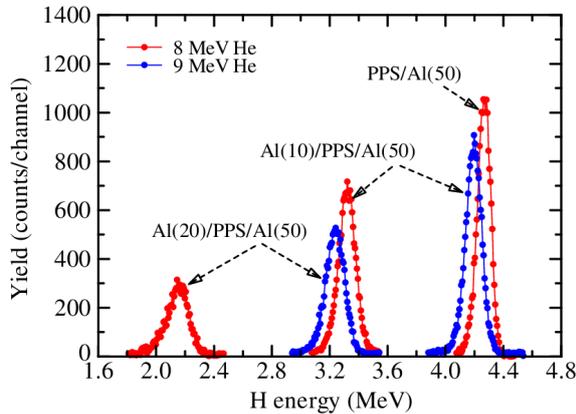
Fig. 2. T-ERDA spectra for incidence of 8 and 9 MeV He^{2+} on the three PPS samples, shown for the same number of incident He^{2+}, 2×10^{11}.
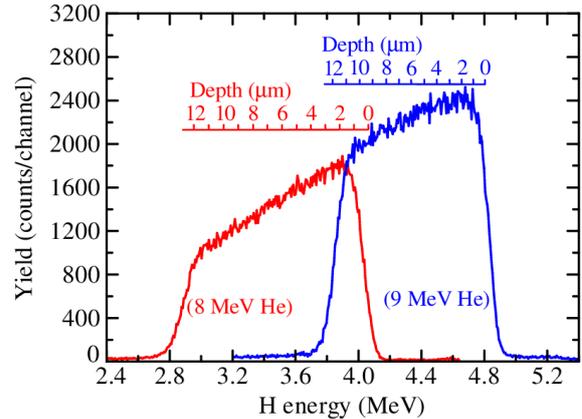
Fig. 3. T-ERDA spectra of recoil H from the muscovite sample, shown for the same number 1.05×10^{12} of incident 8 and 9 MeV He^{2+}.

According to the previous study [3], the present T-ERDA can be discussed using the straight-path approximation for the trajectories of He and recoil H. It is notable that the angular spread of recoil H after passing through the present sample causes negligible change in the H yield. This is because the differential recoil cross section changes slowly with recoil angle in the narrow forward direction under consideration, hence the H yield is unchanged as a whole even when the recoil directions of recoil H are smeared and

mixed with each other by the multiple scattering suffered in the sample. Such physical backgrounds simplify the analysis of the experimental data.

The analysis of the H spectra shown in Figs. 2 and 3 has been based only on the database of stopping power and recoil cross section for material analysis [4], without using any reference sample of known H content. For PPS, the determined H concentration is $(2.87\pm0.26)\times10^{22}$ H/cm^3. This value agrees well and consistently with the calculated concentration of 3.01×10^{22} H/cm^3 from the nominal density of 1.35 g/cm^3 and the atomic composition of $(C_6H_4S)_n$, using Avogadro's constant, which demonstrates the validity of the present analysis. For the muscovite sample, the determined H concentration as a function of the depth is shown in Fig. 4. We see that the results for 8 and 9 MeV He agree consistently with each other at the depth from 1.5 to 11 μm. Outside this depth range, the slopes near the high- and low-energy ends of the spectra should lead to unreliable results. We see uniformity of the H concentration at a depth of 1.5-11 μm, hence the average value $(9.43\pm0.75)\times10^{21}$ H/cm^3 is obtained. This value agrees excellently with the concentration of 9.36×10^{21} H/cm^3 obtained from the composition data, using the density of the muscovite 2.83 g/cm^3 and Avogadro's constant. The results also imply that the H concentration originating from absorbed water is uniform in the muscovite, like that from bound water constituting the crystal structure of muscovite.
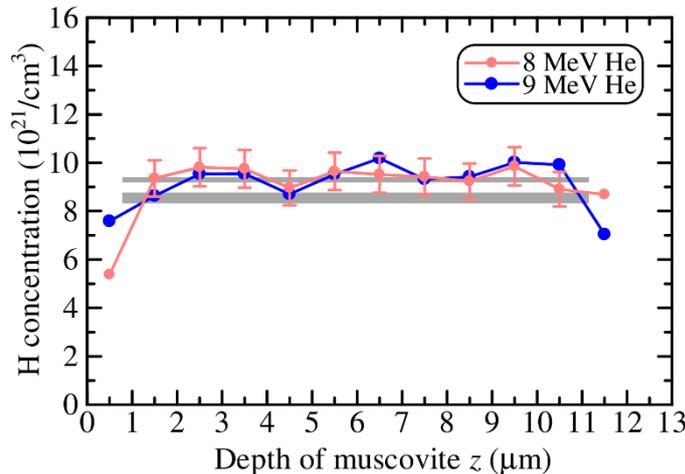
Fig. 4. H concentration in the muscovite, determined by T-ERDA. The uncertainty of ±8% in the values is shown for the 8 MeV case. The horizontal gray thick lines indicate the calculated values of 9.36×10^{21} H/cm^3 (upper) and 8.61×10^{21} H/cm^3 (lower), with and without the absorbed water in the muscovite sample, respectively. The width of these lines represent the uncertainty in the calculation.

For both PPS and the muscovite sample, the determined hydrogen concentrations are in good agreement with the calculated ones. The present quantitative H analysis demonstrates the capability of accurate determination of H contents in materials and minerals by T-ERDA.

References

[1] H. Kudo et al., 2022 J. Phys.: Condens. Matter https://doi.org/10.1088/1361-648X/ac8b4e, also uploaded at arXiv:2206.02387.

[2] A. Yamazaki et al., AIP Advances 9 (2019) 105111.

[3] H. Kudo et al., J. Phys.: Condens. Matter 33 (2021) 465901.

[4] IBANDL (Ion Beam Analysis Nuclear Data Library). https://www-nds.iaea.org/exfor/ibandl.htm

4.3 Effect of LiCoO₂ positive electrode insertion in all-solid-state Li-ion batteries investigated by NRA

N. Kishi, S. Kobayashi[1], Y. Sugisawa, R. Shimizu[1], T. Hitosugi[1], D. Sekiba

All-solid-state Li-ion batteries are attracting much attention, which would safely increase the capacity of Li-ion batteries. At present, there remains a problem that the conductivity is not sufficient for practical use. In the previous study, we tried NRA using the nuclear reaction ^7Li (p, α) ^4He to obtain the Li depth distribution under the operando conditions of an all-solid-state Li-ion battery in order to reveal the Li behavior at interfaces [1]. To check the feasibility of NRA at that time, we used a simplified battery in which a single Au layer (t=100 nm) was used for positive electrode and collector. As a result, we confirmed that non-destructive NRA has a sufficient depth resolution and can be used for operando measurement of all-solid-state Li-ion batteries. Recently, we have obtained NRA results for a more practical sample than before, which has a positive electrode layer made of LiCoO₂ (t=300 nm). The comparative analysis between the simplified and practical batteries is presented in this report.

NRA was performed using 1MV Tandetron at UTTAC. Figure 1 (a) shows the schematics of the experimental arrangement. We used a 1.5 MeV H$^+$ beam. The detector was mounted in the direction of 150° with respect to the beam direction, and the sample was tilted so that the drection of the detector was 70° from the surface normal. Figure 1 (b) shows the schematics of the practical sample. The sample consists of stacked layers of Li/Li₃PO₄/ LiCoO₂/Au deposited on a Si₃N₄ substrate of 1 μm thickness. In order to perform the operando measurement, a positive voltage is applied to the Au layer (collector) with respect to the Li layer (the negative electrode). The power supply for the bias voltage and the ammeter were connected to the sample in vacuum through a feedthrough. The sample was discharged at the bias voltage below 3.0 V and charged at the bias voltage above 4.3 V. Thus the behavior of ^7Li was studied by comparing the NRA spectra at the bias voltage of 4.3 V and 3.0 V.

Figure 2 (a) shows the NRA spectra measured for the simple battery (previous data) [1]. The measurement conditions were similar to those for the practical sample except the applied voltages, 5.0 V and 0.1 V for charge and discharge, respectively. The NRA profiles

(a)

(b)
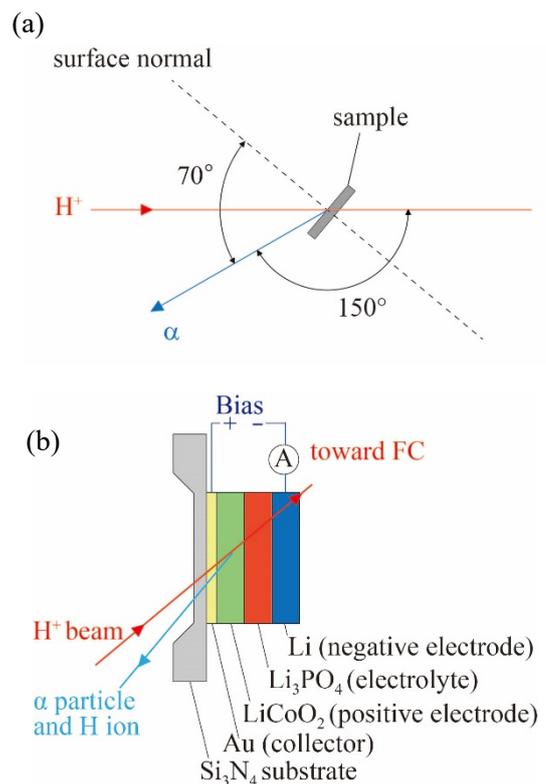
Fig. 1. Schematics of (a) the experimental arrangement and (b) the sample.

[1]Tokyo Institute of Technology.

corresponding to the first charge, discharge, and the second charge are represented by blue, orange, and green lines, respectively. Comparing the blue and orange lines, we notice that the Li ions penetrate into the Au layer, and form the Au-Li alloy layer around $3270 \sim 3320$ channel. This implies a self-organization of the positive electrode. On the other hand, the relative yield of Li layer (negative electrode) around 3050 channel decreases to compensate the Au-Li alloy formation. Figure 2 (b) shows the NRA spectra measured for the practical sample. The applied voltages of +4.3 V, +3.0 V, and again +4.3 V to the Au layer, are represented by blue, orange, and green lines, respectively. In contrast to the case of the simplified sample, we cannot find any drastic change in the NRA spectra through the measurements, while there are subtle changes at both the positive and negative electrodes. We may conclude that this practical battery is of stable structure during the charging and discharging cycle.

In order to focus our attention into the slight changes found in the practical battery, we will improve the statistical accuracy as future work by, for example, increasing the number of detectors and using higher-energy protons, which has larger NRA cross sections. Furthermore, it would be interesting to use a ^{6}Li-enriched target in the deposition of a particular layer.
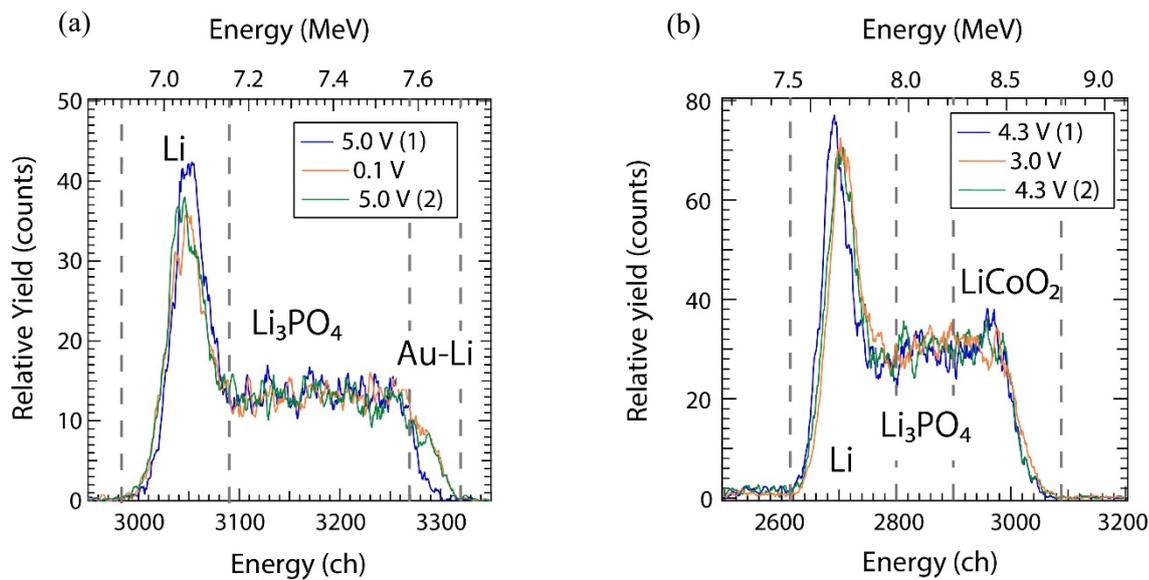
Fig. 2. NRA spectra of (a) Li /Li$_3$PO$_4$ / Au/ Si$_3$N$_4$ and (b) Li /Li$_3$PO$_4$ / LiCoO$_2$/Au/ Si$_3$N$_4$.

Reference

[1] Y. Sugisawa et al., UTTAC Annual Report 2020, UTTAC-90 (2021) 26.

5.

ISOTOPE APPLICATIONS

From the backyard of UTTAC

Monitoring radioactivity for radiation management

5.1 Characterization of GaN grown by oxide vapor phase epitaxy by means of positron annihilation spectroscopy

A. Uedono, J. Takino[1], T. Sumi[1], Y. Okayama[1], M. Imanishi[2], S. Ishibashi[3], Y. Mori[2]

GaN-based vertical power devices have gained tremendous attention due to their potential for large-current and high-voltage operations [1]. Compared with Si and SiC-based devices, the advantages of the GaN devices are a lower on-resistance and higher breakdown voltage, and their trade-off relationship is close to the physical limit of GaN [2]. Although their promising properties are clear, one of the obstacles for their commercialization is a lack of high-quality, low-cost, and large-diameter GaN substrates. The halide vapor phase epitaxy (HVPE) method is a well-established and commercialized method for growing bulk GaN [3]. Although the advantage of HVPE is its high growth rate (> 100 μm/h), the long-term growth of the crystal is limited because of ash accumulation in reaction chambers. Recently, for long-term growth of GaN without ash accumulation, oxide vapor phase epitaxy (OVPE) methods were developed [4]. In the present work, we use positron annihilation spectroscopy to probe vacancy-type defects in GaN grown by the OVPE method [5].

The present samples were GaN grown by the OVPE method. Details on the sample preparation process and the relationship between their properties and growth conditions are given elsewhere [4]. Impurity concentrations in the samples were evaluated by secondary ion mass spectrometry (SIMS), and the results are shown in Fig. 1. In the present work, the samples are referred to as O1 to O6 according to their hydrogen concentrations [H]. Details on the positron annihilation technique used in the present work are given elsewhere [6]. The Doppler broadening spectra of the annihilation radiation were measured with Ge detectors as a function of the incident positron energy E. The obtained spectra were characterized by the line-shape parameter S, defined as the fraction of annihilation events over the energy range of 510.22–511.78 keV.

Fig. 1. Impurity concentrations in OVPE-GaN samples (O1–O6) measured by SIMS.

Figure 2 shows the S parameter of the typical OVPE-GaN samples (O1, O3, and O5) and the MOVPE (metal-organic vapor phase epitaxy)-GaN film grown on O1 (MOVPE/O1) as a function of incident positron energy E. The increase in S at a low E is due to the annihilation of positrons at the surface of the sample. For OVPE/O1, the S value was found to saturate at $E > 15$ keV, and this value was close to the S value for defect-free GaN reported in previous works [7]. The solid curves in Fig. 1 are fits to the experimental data, and the derived diffusion length of positrons L_d for MOVPE/O1 was 77±3 nm. The obtained value of L_d was

---

Fig. 2. Relationships between S parameters and incident positron energy E for OVPE-GaN (O1, O3, and O5) and MOVPE-GaN grown on O1 (MOVPE/O1).
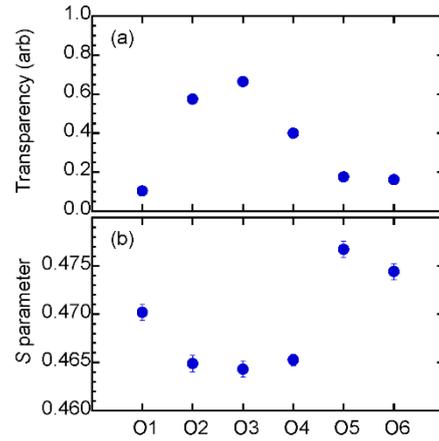
Fig. 3. (a) Relative transparency and (b) S parameters measured by coincidence Doppler broadening system [6] with $E = 28.6$ keV for OVPE-GaN samples.

typical for defect-free GaN. The concentration of vacancy-type defects in MOVPE/O1, therefore, is under the detection limit of positron annihilation. This suggests that the effect of vacancy-type defects in the substrate was negligible in the top epitaxial film. For the OVPE-GaN samples, the saturated S value was larger than that for MOVPE/O1, and the values of L_d were shorter than L_d of MOVPE/O1 (20–30 nm), which can be attributed to the trapping of positrons by vacancy-type defects. The obtained short diffusion length of positrons suggests that almost all positrons were annihilated from the trapped state of vacancies in these samples.

Figure 3(a) shows the relative transparencies and the S value measured by the coincidence system for the OVPE-GaN samples (O1–O6), where the transparency of defect-free GaN grown by Na-flux method [8] was used as a reference. It can be seen that the sample with low transparency tended to show a large S value, suggesting a strong correlation between the transparency and vacancy-type defects in the OVPE-GaN samples. The present experiments suggest that the control of vacancy-type defects is a key to improve the crystal quality of bulk GaN.

References

[1] H. Amano et al., J. Phys. D: Appl. Phys. 51 (2018) 163001.

[2] T. Ueda, Jpn. J. Appl. Phys. 58 (2019) SC0804.

[3] K. Fujito et al., J. Cryst. Growth 311 (2009) 3011.

[4] A. Kitamoto et al., Jpn. J. Appl. Phys. 58 (2019) SC1021.

[5] A. Uedono et al., J. Cryst. Growth 570 (2021) 126219.

[6] R. Krause-Rehberg and H. S. Leipner, Positron Annihilation in Semiconductors, Solid-State Sciences (Springer-Verlag, Berlin, 1999) vol. 127.

[7] A. Uedono et al., Phys. Stat. Sol. (B) 255 (2018) 1700521.

[8] A. Uedono et al., J. Cryst. Growth 475 (2017) 261.

5.2   Low temperature Mössbauer study on a hexagonal FeCo nitride

C. Kodaka, M. Kishimoto, T. Sekido, E. Kita, H. Yanagihara

Fe nitrides have been studied as magnetic materials consisting of common elements such as Fe and nitrogen. Fe nitrogen system forms metallic compounds with several crystal structures depending on the nitrogen content [1]. Small number of nitrogen atoms stabilizes an fcc-structure Fe which is a high temperature phase of Fe and is never realized at room temperature. The Fe-N compound with the lowest concentration of nitrogen is $Fe_{16}N_2$ with a body-centered tetragonal structure, which was extensively studied as an expecting material with high magnetization exceeding bcc Fe [2] and high magnetic anisotropy [3, 4]. Higher nitrogen concentration compounds than $Fe_{16}N_2$ are Fe_4N and $Fe_{2-3}N$ whose basic crystal structures are fcc and hcp, respectively. Additionally, FeNi nitrides, (FeNi)N, has been studied as a precursor of $L1_0$-FeNi ordered compound [3, 4]. On the other hand, nitrides of FeCo alloys have not been studied because of difficulty in their synthesis. Recently, the $(FeCo)_{2-3}N$ alloy with an hcp structure has been studied as novel magnetic materials and/or starting materials for them by using the high-rate ammonia gas nitriding [5]. To investigate magnetic property of $(FeCo)_{2-3}N$, Mössbauer spectroscopy was performed at various temperatures.

A sample was fabricated by nitriding of FeCo alloy powder using the high-rate ammonia gas furnace. At first, FeCo fine hydroxide particles were produced with a co-precipitation technique using Fe and Co chlorides. A nominal atomic ratio of Fe and Co was set to 1:1. After heating in an H_2 gas atmosphere, FeCo spherical particles with averaged diameters of about 400 nm were produced. The FeCo particles were treated in the ammonium-gas furnace to obtain the nitride. The structure of the product was examined with XRD and was confirmed to be an hcp single phase (see Fig. 1) and the nitrogen concentration was determined with an inorganic elemental analysis at Chemical Analysis Division, University of Tsukuba. A sample of $(FeCo)_{2.48}N$ was used for the measurement.

Fig. 1. XRD pattern of $(FeCo)_{2.48}N$ fine particles.

Mössbauer spectroscopy was performed at sample temperatures between room temperature and 2.6 K. To obtain low sample temperatures, a closed-cycle refrigerator cryostat was used [6]. Velocity modulation between −12 mm/s and 12 mm/s was applied to the ^{57}Co gamma-ray source, and the number of transmitted gamma rays were accumulated with a 512 channel MCS.

Figure 2 shows temperature dependence of Mössbauer spectra for the $(FeCo)_{2.48}N$ particles. Spectra below 50 K depict combinations of magnetic sextets due to the circumstance of Fe atoms. The weak peaks

seen at 8 and −7.5 mm/s and are possibly attributed to the Fe^{3+} oxide located on the surface. As a reference, low temperature Mössbauer spectra of $Fe_{2.5}N$ was analyzed by the combination of three sub-spectra with hyperfine fields (H_{hf}) of 66, 142 and 259 kOe [7]. Compared with $Fe_{2.5}N$, magnetic sub-spectrum with lower H_{hf} should exist. This might be due to Co atoms with low magnetic moment around Fe atoms, of which transfer hyperfine field is small. Random arrangement of Co atoms around Fe may cause the distribution in H_{hf}.

With the increase of temperature, the spectrum width becomes narrower and almost constant above 100 K. This implies that the magnetic transition temperature (T_C) places around 100 K. A tentative magnetization measurement supports this result. The T_C for the $(FeCo)_{2.48}N$ is much lower than that of the reference material, $Fe_{2.5}N$, reported to be 400 K [1]. Substitution of Fe atoms by Co atoms should be responsible for the decrease in T_C.
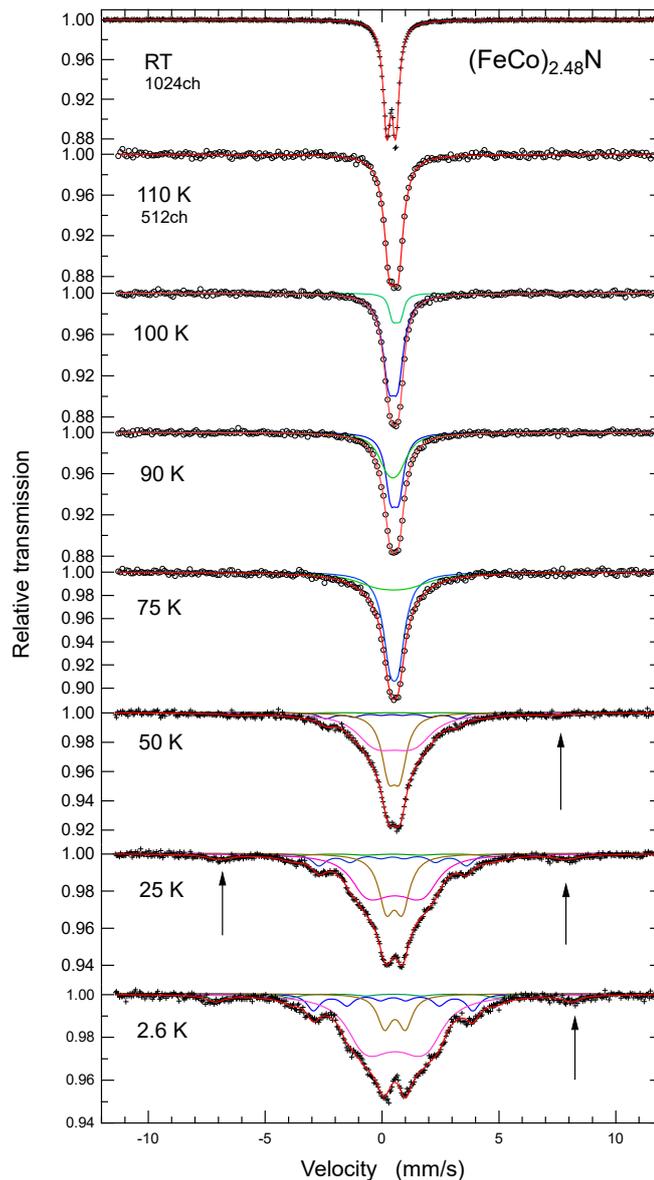
Fig. 2. Mössbauer spectra of $(FeCo)_{2.48}N$ particles at various temperatures. Arrows indicate absorption peaks due to the Fe oxides located on the particle surface.

References

[1] M. Mekata et al., J. Phys. Soc. Jpn. 33 (1972) 62.

[2] J. M. D. Coey, J. Appl. Phys. 76 (1994) 6632.

[3] S. Goto et al., Sci. Reports 7 (2017) 13216.

[4] S. Goto et al., ACS Appl. NANO Mater. 2 (2019) 6909.

[5] Chihiro Kodaka, Bachelor thesis (in Japanese), Engineering science degree program, 2022 Feb. University of Tsukuba.

[6] E. Kita et al., UTTAC Annual Report 2019, UTTAC-89 (2020) 34.

[7] G. M. Chen et al., J. Phys. Chem. 87 (1983) 5326.

5.3　^{57}Fe Mössbauer spectra of La/Fe-Al$_2$O$_3$

H. Asakura[1, 2], K. Terasaka[1]

Even though electric vehicles have been attracting a lot of interest, internal combustion engine vehicles will keep a strong presence in the coming decades. Oxygen storage material (OSM) is a key component for a kind of catalytic converters, three-way catalyst, which converts toxic exhaust gases such as CO, hydrocarbons, and NO$_x$ into CO$_2$, N$_2$, and water. To maximize the catalytic activity, CeO$_2$-ZrO$_2$ solid solution has been used as only one practical OSM for co-catalyst of three-way catalysis to maintain oxygen concentration to a suitable level. However, Ce and Zr are relatively scarce and expensive. So, alternative OSM have been desired.

We found, by chance, Fe-doped γ-Al$_2$O$_3$ works as an OSM without any rare elements [1]. However, the Fe-doped γ-Al$_2$O$_3$ (denoted as "Fe") was decomposed into α-Al$_2$O$_3$ under high temperature conditions, for example, at 1273 K, which can be experienced under the working condition of three-way catalysts. Therefore, we prepared La/Fe-Al$_2$O$_3$ ("Fe-La") from γ-Al$_2$O$_3$ and aqueous solution of metal nitrates as precursors by an impregnation method, followed by calcination under air and reduction under diluted hydrogen at high temperature. Rh/Ce$_{0.5}$Zr$_{0.5}$O$_2$ was prepared by a polymerized complex method, followed by an impregnation method.

The oxygen storage capacity (OSC) of the samples was evaluated by thermogravimetic profiles under cycle of 2% O$_2$/He or 2% H$_2$/He flow (Fig. 1). The Fe and Fe-La exhibited comparable OSC (ca. 1.2 wt%) to that of Rh/Ce$_{0.5}$Zr$_{0.5}$O$_2$. The OSC of "Fe" drastically decreased after the calcination at 1273 K (0.4 wt%), however, addition of La suppressed this deterioration and kept 0.9 wt% of OSC (Fig. 2).

We performed XRD analysis on these samples and found that each sample except for Fe-La calcined at 1273 K exhibits simple XRD patterns assignable to the spinel structure. In addition, after the high temperature reduction, the diffraction peaks shift to lower angles, corresponding to lattice expansion, which
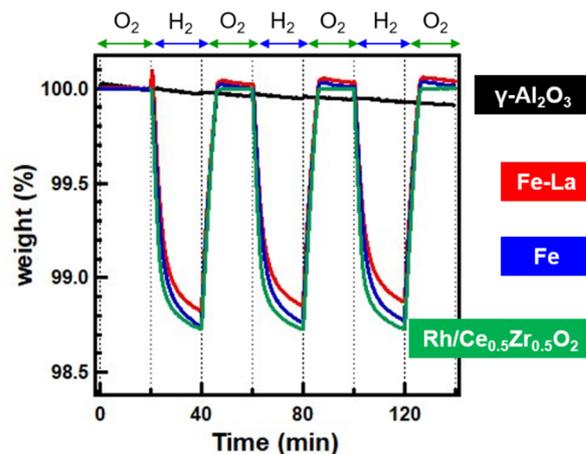
Fig. 1. Thermogravimetric profiles of Fe, Fe-La, Rh/Ce$_{0.5}$Zr$_{0.5}$O$_2$ under oxygen storage/release cycles of 2% O$_2$ and 2% H$_2$ at 773 K.
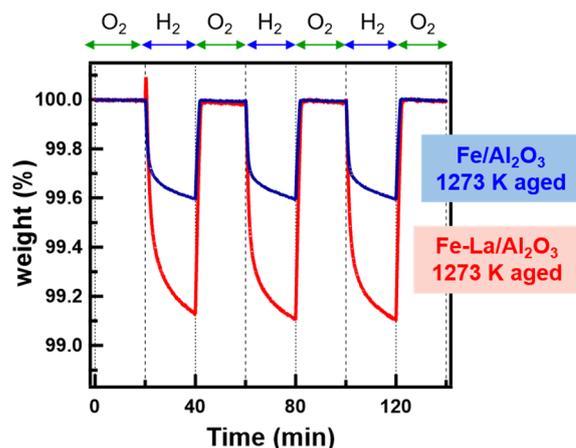
Fig. 2. Thermogravimetric profiles of Fe and Fe-La, calcined at 1273 K under oxygen storage/release cycles of 2% O$_2$ and 2% H$_2$ at 773 K.

[1]Kyoto University

[2]Kindai University (Current affiliation)

indicate incorporation of Fe cations into the spinel framework of γ-Al_2O_3. Then, we tried Mössbauer spectroscopy at room temperature to identify the states of Fe species.

Figure 3 shows the Mössbauer spectrum of Fe-La after high temperature reduction. We obtained a reasonable curve fitting result with two doublet peaks, which indicates presence of Fe^{2+} and Fe^{3+} at the tetrahedral site of the spinel framework. In contrast, the spectrum of Fe-La in oxidized state (Fig. 4) shows only one doublet peak with the same isomer shift of Fe^{3+} at Td site after reduction. The small amount of Fe^{3+} at the Td site in the reduced sample is explained by the fact that it is easily oxidized in air under ambient conditions. These results indicate that the Fe species is incorporated into the Td site (A site) of the spinel structure.

On the other hand, the γ-Al_2O_3 framework of the Fe sample without La doping completely collapsed into α-Al_2O_3 after the calcination at 1273 K as evidenced by their XRD patterns. The Mössbauer spectrum differs from those of the Fe-La samples and can be fitted with two doublet peaks, as shown in Fig. 5. At present, we have assigned the two peaks to Fe^{3+} at the Td site of the spinel structure and Fe^{3+} cations incorporated into the α-Al_2O_3, thus the OSC of the Fe sample after high temperature calcination significantly decreased. Further analysis with in-situ XAS/XRD measurement is undergoing.

Fig. 3. Mössbauer spectrum of Fe-La after high temperature reduction.

Fig. 4. Mössbauer spectrum of Fe-La in oxidized state.
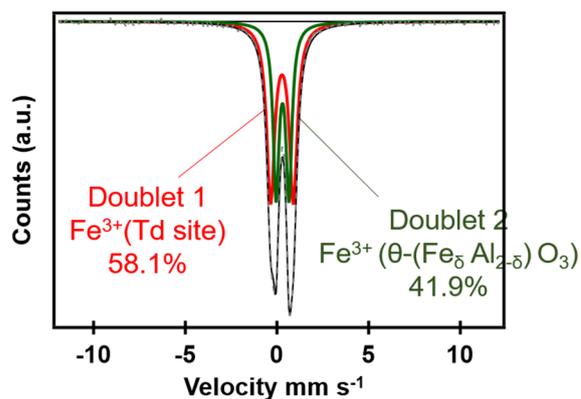
Fig. 5. Mössbauer spectrum of the Fe sample after calcination at 1273 K.

Reference

[1] K. Fujita et al., ACS Appl. Mater. Interfaces 13 (2021) 24615.

5.4 Mössbauer study of Fe ions in ferrocene derivative-based assemblies on a graphene oxide surface

M. Sakurai[1], P. Koley[1], E. Kita

Molecular assemblies of magnetic molecules on a surface are attractive building blocks in molecular spintronics and electronics. Here, we study magnetic properties of ferrocene derivative-based assemblies formed through on-surface chemical reactions (Fig. 1) by using ^{57}Fe Mössbauer spectroscopy at low temperatures.

Fe ions in the ferrocene derivatives on the graphene oxide (GO) nanosheet have unpaired electrons through charge transfer between the molecules and the nanosheet [1]. The isolated molecules are paramagnetic, however their assemblies on the GO surface show hyperfine splitting in Mössbauer spectra at low temperatures. The present study shows that onset temperature of the splitting is higher for the assemblies with an average diameter of 2.7 nm (Fig. 2) than those with an average diameter of 2.0 nm.

Fig. 1. Transmission electron microscope (TEM) image of ferrocene derivative-based assemblies (dark region) on a graphene oxide nanosheet.

The splitting is caused by slow magnetization relaxation, because the reaction time of Mössbauer spectroscopy with $10^{-8} - 10^{-12}$ s is shorter than the relaxation time of the molecular spins within the assemblies at low temperature. As the temperature decreases, the suppression of thermal spin fluctuations produces spin correlations between the Fe ions, leading to the onset of slow magnetization relaxation. The present approach based on assembling magnetic molecules in a self-organized manner and creating new functionalities through the assembly provides new insights into molecular and low-dimensional magnetism.

---

[1]National Institute for Materials Science
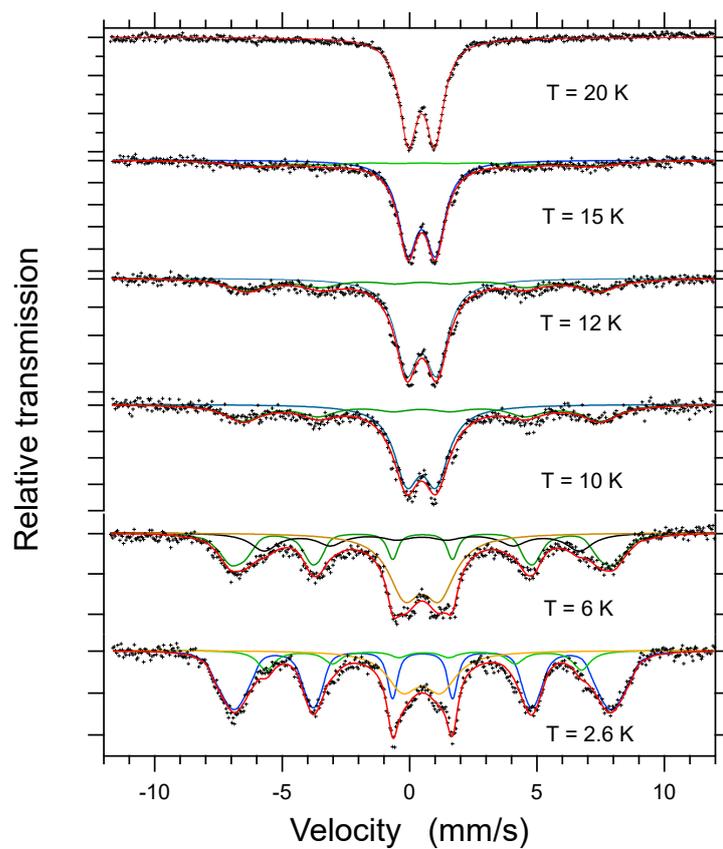
Fig. 2. Mössbauer spectra of ferrocene derivative-based assemblies on a graphene oxide nanosheet at low temperatures.

Reference

[1] M. Sakurai et al., J. Phys. Chem. 123 (2019) 29679.

6.

BEAM IRRADIATION EFFECT

Radiation tolerance test of electronic devices for use in space. The JAXA team is acquiring the data remotely in the booth adjacent to the accelerator operation desk. Recently, the experimenters are from JAXA, industries, and our campus.

6.1 Evaluation of radiation resistance of MPU and LoRa communication components for space applications

Y. Kurihara, H. Yoshikado, R. Tanaka, R. Takatsuki, T. Okamoto, T. Kameda

When using semiconductor components in space, it is necessary to consider the effects of cosmic radiation for stable operation. In particular, heavy ions in cosmic radiation can cause SEE (Single Event Effect), which can lead to temporary malfunctions (soft errors) and/or permanent failures (hard errors) in semiconductors and interfere with spacecraft operations, therefore detailed investigation is required in advance.

We focused on space application of LoRa modulation because of its high interference tolerance over very long distances and low current consumption. From this perspective, the feasibility of space applications of STM32L072CZ and the LoRa transceiver, SX1276 [1], built into the CMWX1ZZABZ-091 LoRa® module [2] manufactured by Murata Manufacturing Co.

Using the 6MV tandem accelerator at UTTAC, we irradiated de-capped SRM32L072CZ and SX1276 with F and Cl ions with the condition shown in Table 1, while changing the number of ions, and monitored the incidence of bit flips associated with soft errors and the increase in power consumption associated with hard errors to evaluate the SEU (Single Event Upset) and SEL (Single Event Latch-up) occurrence.

Two printed circuit boards of B-L072CZ-LRWAN LoRa®Discovery kit [3] were used as test specimens, and Char type "U" (0x55, 0b01010101) was written in the unused 18KB area of the 20KB RAM in STM32L072CZ for testing purpose. These boards were powered by a regulated power supply, and each current was recorded every 0.5 seconds using an INA216 (accuracy ±1%) to monitor SEL. The SEUs were monitored by comparing all the data collected every 10000 ms during irradiation.

In Figure 1, 1A refers to SX1276 and 2B to STM32L072CZ. Table 1 summarizes the results of experiments. For STM32L072CZ, no SEU was observed during the test as the number of particles was increased. On the contrary, when SX1276 was irradiated, an increase in current of about 30mA was observed with increasing a small amount of particles. Considering that roughly the same current of 30mA was consumed by SX1276 during transmission, we may assume that the SEU was generated and activated in a register in the SX1276. Hence, the lower three bits of RegOpMode (0x01) may have changed from 000 (Sleep mode) to 010 (FS mode TX) or 001 (Stdby mode) to 011 (Transmitter mode), although a further investigation is required to prove such behavior. In conclusion, STM32L0CZ MPU has resistance against cosmic radiation of LET=7.2 [MeV/(mg/cm^2)] level. SX1276 requires further investigation for quantitative evaluation for space application.

Table. 1. Experimental results

Ion species	LET [MeV/(mg/cm^2)]	Ion range in silicon [μm]	Ion charge	Energy [MeV]	Elapsed time	Target	Number of particles	SEE SEU	SEE SEL
Cl	17.3	14.2	7	48	0:18:33	1A	1078	x	+30mA
Cl	17.3	14.2	7	48	0:18:33	2B	1078	x	x
Cl	17.3	14.2	7	48	0:18:20	1A	1602	x	+30mA
Cl	17.3	14.2	7	48	0:18:06	2B	1602	x	x
Cl	17.3	14.2	7	48	0:18:30	1A	2765	x	+30mA
Cl	17.3	14.2	7	48	0:18:43	2B	2765	x	x
Cl	17.3	14.2	7	48	0:17:56	1A	3400	x	+30mA
Cl	17.3	14.2	7	48	0:18:38	2B	3400	x	x
Cl	17.3	14.2	7	48	0:17:29	1A	19000	x	+30mA
Cl	17.3	14.2	7	48	0:18:00	2B	19000	x	x
F	7.2	14.3	3	24	0:17:57	1A	957	x	+30mA
F	7.2	14.3	3	24	0:17:56	2B	957	x	x
F	7.2	14.3	3	24	0:18:17	1A	2154	x	+37mA
F	7.2	14.3	3	24	0:18:01	2B	2154	x	x
F	7.2	14.3	3	24	0:18:53	1A	531	x	+29mA
F	7.2	14.3	3	24	0:18:00	1A	531	x	+32mA
F	7.2	14.3	3	24	0:18:22	1A	214	x	+31mA
F	7.2	14.3	3	24	0:18:14	1A	3189	x	+37mA
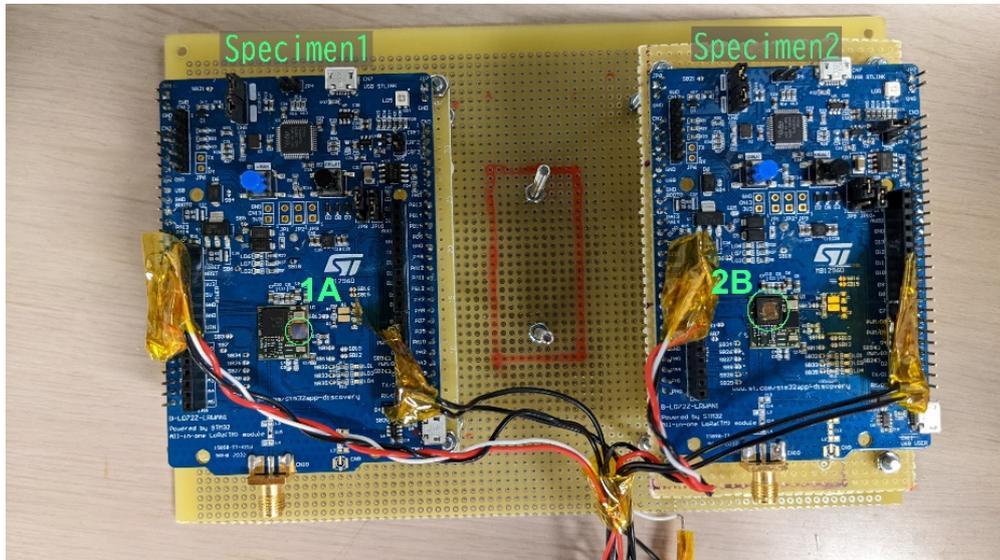
Fig. 1. Specimens and irradiated positions.

References

[1] Semtech Corporation, SX1276/77/78/79 Datasheet,
https://semtech.my.salesforce.com/sfc/p/#E0000000JelG/a/2R0000001Rbr/6EfVZUorrpoKFfvaF_Fkp
gp5kzjiNyiAbqcpqh9qSjE

[2] Murata Manufacturing Co., Ltd., Type ABZ CMWX1ZZABZ, https://www.murata.com/ja-
jp/products/connectivitymodule/lpwa/overview/lineup/type-abz

[3] STMicroelectronics, B-L072Z-LRWAN1 Product overview, https://www.st.com/en/evaluation-
tools/b-l072z-lrwan1.html

6.2　Development of QCM sensor system for use in space

T. Shiobara[1], E. Miyazaki[1], H. Kukita[2]

As a result of contract development and joint research with Japan Aerospace Exploration Agency (JAXA), Nihon Dempa Kogyo Co., Ltd. (NDK) developed "New outgas analysis system: Twin-QCM sensor system" for quantitative and qualitative analysis of outgas released from organic materials such as adhesives, heat dissipation materials, and resins in a vacuum environment. This system was put on the market [1, 2].

JAXA and NDK have started a joint research for development of the flight model enabling the Twin-QCM sensor system, which is mainly used now for research and evaluation on the ground, to be used in outer space on a satellite. In the flight model, we plan to use COTS (Commercial Off-The-Shelf) grade parts for electronic parts to reduce the cost significantly and, accordingly, to evaluate the radiation resistance performance of COTS grade parts in the space environment. A beam irradiation test using heavy ions from the 6MV tandem accelerator at UTTAC was performed for a BBM (bread board model) circuit board. Our purposes are to conduct a test of the single event effect as a part of evaluation of the radiation resistance, mentioned above, and to use the test result as a basis for determining whether or not to adopt the components.

(1)　Experimental results in December 2021

Irradiation tests with 66 MeV Si^{10+} and 90 MeV Br^{14+} were performed. The test results and calculated LET for Si^{10+} are described in the table below (the Br^{14+} data is omitted).

Ion	mass number	Energy [MeV]
Si	28	66.00

Parts	Manu-facturer	Component	Material	Thickness [μm]	After passing thru. the substance		Test results
					LET in Si [MeV/(mg/cm²)]	Range in Si [μm]	
A	a	Initial	–	–	12.408	22.720	SEL: no occurrence SET: one momentary disturbance occurred (#1)
		Scatterer	Au	0.20	12.532	22.041	
		Wiring layer	Al	6.50	13.623	14.569	
		Semiconductor sensitive layer	Si	1.00	13.739	13.569	
		Si substrate	Si	106.00	0.000	0.000	
B	b	Initial	–	–	12.408	22.720	SEL: no occurrence SET: no occurrence
		Scatterer	Au	0.20	12.532	22.041	
		Wiring layer	Al	4.70	13.348	16.641	
		Semiconductor sensitive layer	Si	1.00	13.480	15.641	
		Si substrate	Si	120.00	0.000	0.000	

#1 Possibly not to the irradiation effect, but to electromagnetic noise.

For both Si^{10+} and Br^{14+}, the range and LET (Linear Energy Transfer) in the Si sensitive layer are insufficient for the tested IC. Next approaches with other ions and modified test methods are under

---

[1] Nihon Dempa Kogyo Co., Ltd. (NDK)

[2] Japan Aerospace Exploration Agency

consideration for evaluation of single event to calculate the threshold LET and saturation cross-sections.

(2) Experimental results in February 2022

Irradiation tests with 66 MeV Si[10+] and 72 MeV Cl[11+] were performed. The test results and calculated LET for Si[10+] are described in the table below (the Cl[11+] data is omitted).

Ion	mass number	Energy [MeV]
Si	28	66.00

Parts	Manu-facturer	Component	Material	Thickness [μm]	After passing thru. the substance		Test results
					LET in Si [MeV/(mg/cm^2)]	Range in Si [μm]	
C	c	Initial	−	−	12.408	22.720	SEL: no occurrence SET: no occurrence
		Scatterer	Au	0.20	12.532	22.041	
		Wiring layer	Al	13.70	13.629	6.298	
		Semiconductor sensitive layer	Si	1.00	13.237	5.298	
		Si substrate	Si	152.00	0.000	0.000	
D	c	Initial	−	−	12.408	22.720	SEL: no occurrence SET: no occurrence
		Scatterer	Au	0.20	12.532	22.041	
		Protective film	Kapton	4.00	13.036	18.903	
		Wiring layer	Al	13.60	11.610	3.340	
		Semiconductor sensitive layer	Si	1.00	9.823	2.340	
		Si substrate	Si	151.00	0.000	0.000	
E	b	Initial	−	−	12.408	22.720	SEL: no occurrence SET: no occurrence
		Scatterer	Au	0.20	12.532	22.041	
		Wiring layer	Al	4.20	13.273	17.216	
		Semiconductor sensitive layer	Si	1.00	13.404	16.216	
		Si substrate	Si	291.00	0.000	0.000	
F	b	Initial	−	−	12.408	22.720	SEL: no occurrence SET: no occurrence
		Scatterer	Au	0.20	12.532	22.041	
		Wiring layer	Al	5.10	13.409	16.181	
		Semiconductor sensitive layer	Si	1.00	13.541	15.181	
		Si substrate	Si	213.00	0.000	0.000	

For both Si[10+] and Cl[11+], the range and LET in the Si sensitive layer are insufficient for the tested IC, causing no single event error, from which the threshold LET and saturated cross-sections are to be calculated. We will continue to consider the calculation of the error rate on the actual satellite orbits, the applicability of parts in space, and test methods in future.

References

[1] Nihon Dempa Kogyo Co., Ltd. Outgas Analysis System

https://www.ndk.com/jp/products/search/outgas/index.html

[2] Y. Tsuchiya et al., IEEE Sensors Journal 21 (2021) 10530.

https://ieeexplore.ieee.org/document/9351992

6.3 Unusual enhancement of self-field critical current density in YBa$_2$Cu$_3$O$_7$ films by several-tens-MeV Au ion irradiation

H. Matsui[1], I. Yamaguchi[1]

Applications of second-generation high-temperature superconducting wires consisting of YBa$_2$Cu$_3$O$_7$ (YBCO, critical temperature $T_c \sim 92$ K) films are roughly categorized into two groups based on the environment of their use: (i) high-temperature (> 65 K), self-field applications such as power-transmission lines, and (ii) low-temperature (< 65 K), in-magnetic-field applications such as motors and generators. In both groups, research efforts are focused on how to maximize the critical current density (J_c) via microstructure modification. However, in many kinds of YBCO films, enhancing J_c by such modification is more difficult at self-field (J_c^{sf}) than that at applied magnetic fields [1, 2]. Lack of sufficient number of examples of "J_c^{sf}" enhancement in YBCO films makes it unclear what type of microstructure in the material is ideal for application (i) above, namely, for J_c^{sf} at high temperatures.

In this work, we performed 24- to 84-MeV Au-ion irradiation on 1-µm-thick YBCO films prepared by fluorine-free metal organic deposition (FF-MOD) to gain insight into what type of microstructure in YBCO films is effective for J_c^{sf} at high temperatures. We observed significant enhancement (up to 63%) in J_c^{sf} in FF-MOD YBCO films at 77 K by introducing the discontinuous 1D irradiation defects of 5-10 nm in diameter, ~20 nm in size along an ion track, and a ~20 nm gap between defects in an ion track, which are directed in the c-axis.

We deposited 1.0-µm-thick YBCO epitaxial films ($T_c = 90.8$ K) on CeO$_2$-buffered SrTiO$_3$ substrates by FF-MOD [3]. For comparison, we also used 0.7-µm-thick YBCO epitaxial films (CERACO ceramic coating GmbH, $T_c = 87.9$ K) on SrTiO$_3$ substrates deposited by thermal co-evaporation. The Au-ion irradiation at different ion energies E_i =24, 44, 66, 75, and 84 MeV at room temperature was performed under a vacuum pressure of 1×10^{-6} Torr with the 6MV tandem accelerator at UTTAC. The specimens were fixed to a sample holder by electrically conductive adhesive tape to avoid electric charging by the ion irradiation. The incident angle of ions was set normal to the film surface. Irradiation dose of $3\times10^8 - 1\times10^{12}$ cm^{-2} was controlled by beam current and exposure time. J_c and T_c were measured inductively with a Cryoscan (THEVA).

Figures 1(a)–(e) show the dose dependence of J_c^{sf} in Au-irradiated FF-MOD YBCO films [4]. For comparison, J_c^{sf} values measured before irradiation ("as-grown"; open symbols) are also plotted in the same horizontal position as those after irradiation (filled symbols). At E_i=66 to 84 MeV, J_c^{sf} is significantly enhanced up to $J_c^{sf} = 2.2$ MA/cm^2 with a maximum enhancement factor of $J_c^{sf}/J_c^{sf}{}_{as-grown}$=1.6, while the enhancement is only slight at E_i =24 or 44 MeV, i.e., up to $J_c^{sf} = 1.7$ MA/cm^2 with a maximum enhancement factor of 1.2. The present observation of J_c^{sf} enhancement itself is unusual in YBCO films. In Fig. 1(f), the co-evaporated YBCO film shows as-grown J_c^{sf} values higher than those of the FF-MOD YBCO films, and also shows a negligibly small increase in J_c^{sf} after irradiation at 66 MeV, in contrast to the case in Fig. 1(c). This result is consistent with the absence of J_c^{sf} enhancement previously reported in the ion-irradiation

studies on YBCO films deposited by various methods [1]. This contrast in J_c^{sf} enhancement between FF-MOD and other film-deposition methods can be attributed to different microstructures in the as-grown samples. Namely, small pin density, i.e., clean microstructure, in FF-MOD YBCO films can cause the relatively low as-grown J_c^{sf} (~ 1.5 MA/cm^2), however it can be compensated by the irradiation defects, resulting in enhanced J_c^{sf}. This interpretation is supported by our results of film-thickness dependence of the irradiation effect and our microstructure imaging [4].
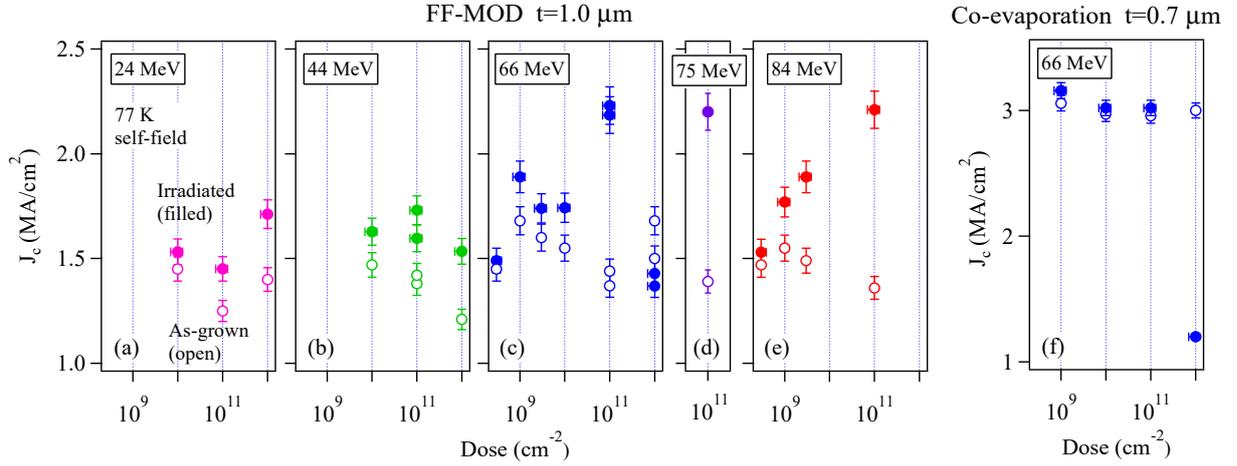
Fig. 1. Dose dependence of J_c^{sf} at 77 K in Au-irradiated YBCO films [4]. For comparison, J_c^{sf} values measured before irradiation (as-grown; open symbols) are plotted are also plotted in the same horizontal position as those after irradiation (filled symbols).

References

[1] S. R. Foltyn et al., Nature Mater. 6 (2007) 631.

[2] J. P. F. Feighan et al., Sci. Technol. 30 (2017) 123001.

[3] K. Tsukada et al., Physica C 458 (2007) 29.

[4] H. Matsui and I. Yamaguchi, Jpn. J. Appl. Phys. 61 (2022) 043001.

6.4 Study on mutagenesis with ^{15}N-resonant nuclear reaction and radiation effects

I. Suzuki, T. Yang, T. Ikeda, K. Sasa, S. Ishii, K. Tomita[1], Y. Iwata[1]

Marine microalgae draw people's attention as a new Blue Carbon to provide a generic technology of the supply chain with high-density culture. The authors aim to mutate *Haptophyte* of marine microalgae to enhance the productivity of long-chain unsaturated alkyl ketone (alkenone) that enables conversion to completely interchangeable biofuel (drop-in-fuel) for conventional petroleum-derived fuel. Furthermore, aminolevulinic acid (5-ALA), that can be applicable to new cancer therapy is also the featured product of the mutation *Haptophyte* strains.

Resonant nuclear reaction ^{15}N(p, $\alpha_1\gamma$)^{12}C (^{15}N-RNR) causes such strong structural modification of DNA as never induced by heavy ion irradiation, since high-density electronic excitation by the ^{12}C and ^{4}He product ions takes place inside DNA molecule efficiently. Structural modification of the target genes in DNA can be achieved by substituting 98% constituent nitrogen atoms of the targeted bases with isotopic tagged ^{15}N.

We have developed a vacuum flange to encapsulate cells alive in vacuum, named CS vacuum flange that possesses a metallic but soft shieling feature [1], since the resonance energy of the ^{15}N-RNR is too low for any proton beam to keep the precise resonance energy after being extracted into the atmosphere. Covering living mammalian cells in a culture medium with a polyphenylene sulfide film (Torelina™, TORAY) with 4 μm in thickness and shieling together with the medium in vacuum by the CS vacuum flange, we succeeded in proton-beam irradiation to the cells alive (see Fig. 1). We used the model RGM-GFP (normal cell) that were cultivated in a medium containing 5-ALA labeled with ^{15}N (^{15}N_5-ALA).

Proton beam irradiation was performed with utilizing the C-beam course of the 1MV Tandetron accelerator in UTTAC. After rinsing the ^{15}N_5-ALA medium, ^{15}N-labeled living
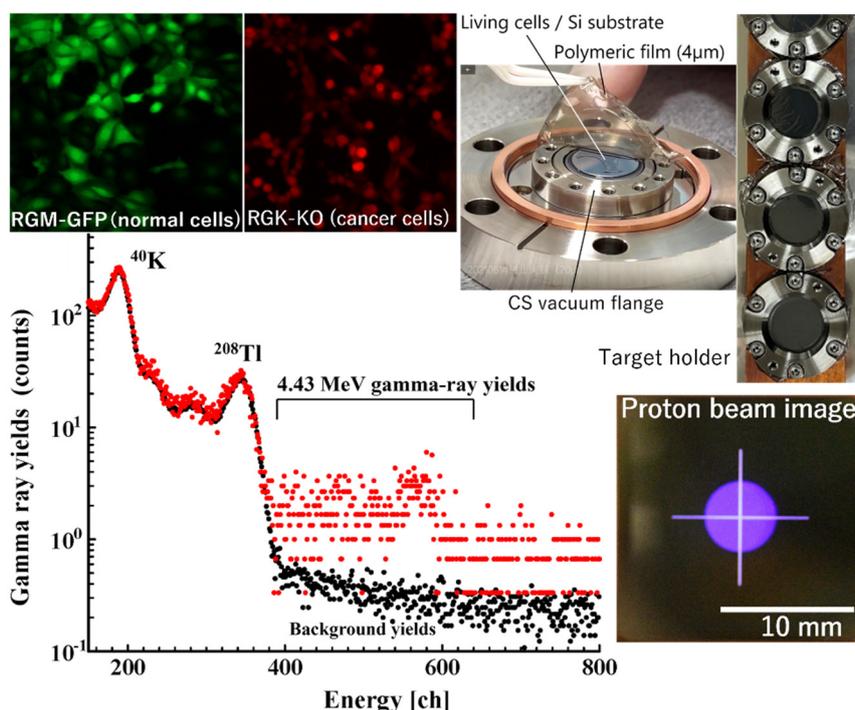
Fig. 1. CS vacuum flange to encapsulate cells alive in vacuum. Polyphenylene sulfide film (Torelina™, TORAY) is tolerant of hydrolysis and is suited for shieling cells together with the solution in vacuum. Both ^{15}N-labbeled model cells of RGM-GFP (normal cells) and RGK-KO (cancer cells) were covered with a Torelina film of 4 μm in thickness and the cells were irradiated with a proton beam through the film to detect the 4.43 MeV gamma-rays emitted from ^{15}N_NR.

[1]National Institute of Industustrial Science and Technology (AIST).
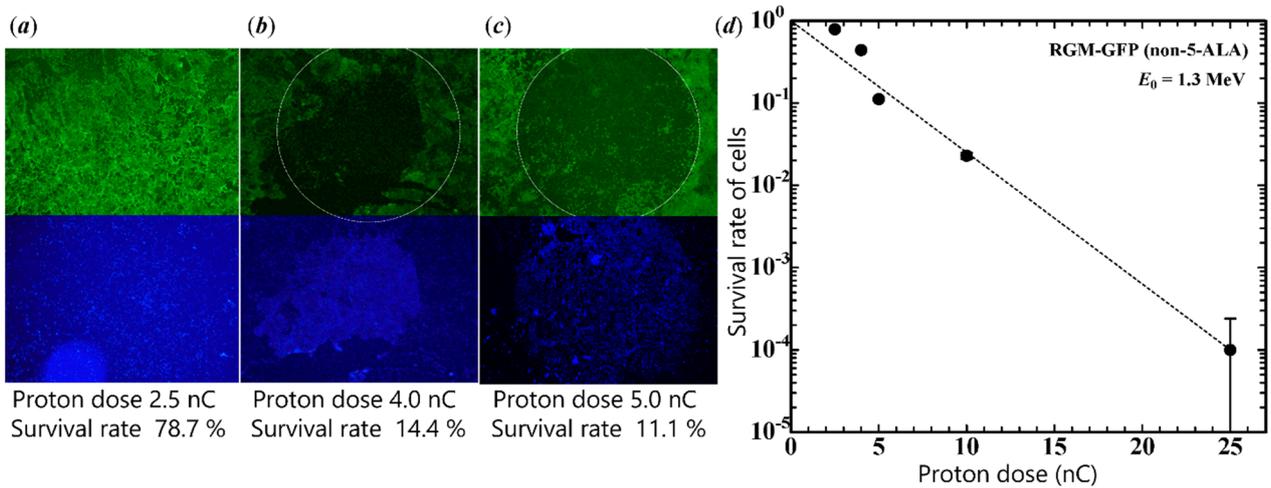
Fig. 2. Cell images alive after proton irradiation and their survival rate.
(*a*)~(*c*) Fluorescence microscopy images of the RGM-GFP cells alive (upper stage) and the same images of decease cells revealed with DAPI stain (lower stage). The beam irradiation area is indicated in the cell images by a white circle. The survival rate of the RGM-GFP cells as a function of proton dose (nC) is shown in (*d*).

cells were irradiated with a proton beam. First of all, we demonstrated the ^{15}N-RNR in collision with the ^{15}N accumulated in the cells by detecting the 4.43 MeV gamma-rays specific to the ^{15}N-RNR (see Fig. 1). The energy shift at the 1210 keV resonance energy after passing through the 4 μm Torelina™ film was 110 keV. By subtracting the energy loss of proton in the film, which was evaluated with the stopping power given by the SRIM-2013 code [2], the thickness of the encapsulate solution was estimated as 4 μm in H_2O terms. The proton path is shorter than the average diameter of the cells.

   Using the method for encapsulating the living cells in vacuum, the authors investigated the survival rate of the RGM-GFP cells in proton irradiation. We can observe the green fluorescence from the living RGM-GFP cells, and DNAs in the deceased cells were stained with 4',6-diamidino-2-phenylindole (DAPI) stain under the fluorescent microscopy. The fluorescence microscopy images of the living RGM-GFP cells after proton irradiation are shown in the upper stages in Fig. 2*a-c*. On the other hand, the same images of the deceased cells were revealed with DAPI staining of nucleic acids, as shown in the lower stages. The survival rate can be set as the ratio of the number of living cells (in the upper stages) to the total cells (sum in the upper and lower stages). The results of the survival rate of the RGM-GFP cells show a logarithm curve as a function of the proton dose in particle charge terms (nC) (see Fig. 2*d*).

   The present results substantiated that ^{15}N-RNR is applicable to mutagenesis of microalgae using the method for encapsulating living cells in vacuum, even though the resonance energy of ^{15}N-RNR is lower than 1 MeV. Also, ^{15}N-RNR is useful for quantitative evaluation of ^{15}N accumulated specifically in the cancer cells.

References

[1] Y. Iwata and A. Chayahara, US patent 7648586 2010/01/19, JP patent 5392752 2013/10/08.
[2] J. F. Ziegler et al., http://srim.org/

7.

LIST OF PUBLICATIONS AND PRESENTATIONS

ON-LINE
SYMPOSIUM

7.1 Peer-reviewed and proceedings papers

ACCELERATOR AND RERATED FACILITIES

1. G. Yoshida, H. Matsumura, H. Nakamura, A. Toyoda, K. Masumoto, T. Miura, K. Sasa, T. Moriguchi, "Survey Methodology for the Activation of Beamline Components in an Electrostatic Proton Accelerator", Radiation Safety Management 20 (2021) 1. [DOI:10.12950/rsm.200813]

NUCLEAR AND ATOMIC PHYSICS

1. Y. Kimura, M. Mihara, K. Matsuta, M. Fukuda, Y. Otani, G. Takayama, T. Izumikawa, N. Noguchi, M. Ogose, Y. Sato, K. Takatsu, T. Ohtsubo, H. Takahashi, S. Momota, H. Okumura, T. Moriguchi, A. Ozawa, A. Kitagawa, S. Sato, "Development of a small Beta-NMR system using Halbach Array permanent magnet", Hyperfine Interact. 243 (2022) 1. [DOI:10.1007/s10751-021-01789-5]

2. Y. Otani, M. Mihara, K. Matsuta, M. Fukuda, R. Wakabayashi, N. Okimoto, M. Fukutome, Y. Kimura, G. Takayama, T. Izumikawa, N. Noguchi, M. Ogose, M. Sato, K. Takatsu, T. Ohtsubo, D. Nishimura, H. Takahashi, S. Sugawara, A. Gladkov, H. Ishiyama, A. Kitagawa, S. Sato, S. Momota, H. Okumura, T. Moriguchi, A. Ozawa, N. Kaname, A. Yano, "Application of spin polarized ^{19}O beam to the study of oxygen motion in solid oxide fuel cell materials", Hyperfine Interact. 242 (2021) 47. [DOI:10.1007/s10751-021-01776-w]

3. A. Ozawa for Rare-RI Ring collaboration, "Past and future for Rare-RI Ring", JPS Conf. Proc. 35 (2021) 011011. [DOI:10.7566/JPSCP.35.011011]

4. D. Nagae, S. Omika, Y. Abe, Y. Yamaguchi, F. Suzaki, K. Wakayama, N. Tadano, R. Igosawa, K. Inomata, H. Arakawa, K. Nishimuro, T. Fujii, T. Mitsui, T. Yamaguchi, T. Suzuki, S. Suzuki, T. Moriguchi, M. Amano, D. Kamioka, A. Ozawa, S. Naimi, Z. Ge, Y. Yanagisawa, H. Baba, S. Michimasa, S. Ota, G. Lorusso, Y. A. Litvinov, M. Wakasugi, T. Uesaka, Y. Yano, "First demonstration of mass measurements for exotic nuclei using Rare-RI Ring", JPS Conf. Proc. 35 (2021) 011014. [DOI:10.7566/JPSCP.35.011014]

5. S. Suzuki, A. Ozawa, T. Moriguchi, M. Amano, D. Kamioka, Y. Ichikawa, Y. Tajiri, K. Hiraishi, T. Matsumoto, D. Nagae, Y. Abe, S. Naimi, H. Li, T. Yamaguchi, S. Omika, Z. Ge, K. Wakayama, N. Tadano, H. Arakawa, K. Inomata, T. Kobayashi, A. Kitagawa, S. Sato, "Performance of a Time-Of-Flight detector and demonstration of a novel position-sensitive detector for mass measurements with the Rare-RI Ring", JPS Conf. Proc. 35 (2021) 011017. [DOI:10.7566/JPSCP.35.011017]

6. K. Inomata, T. Yamaguchi, Y. Abe, M. Amano, H. Arakawa, T. Fujii, D. Kamioka, A. Kitagawa, H. Li, T. Moriguchi, D. Nagae, S. Omika, A. Ozawa, S. Sato, S. Suzuki, T. Suzuki, K. Wakayama, "Basic Study on Delta Ray Detection for the Determination of In-Ring Revolution Time", JPS Conf. Proc. 35 (2021) 011020. [DOI:10.7566/JPSCP.35.011020]

7. H. Arakawa, Y. Yamaguchi, Y. Abe, M. Amano, K. Inomata, D. Kamioka, A. Kitagawa, H. Li, T. Moriguchi, D. Nagae, S. Omika, A. Ozawa, S. Sato, S. Suzuki, T. Suzuki, K. Wakayama, "Properties of a thin YAP(Ce) scintillation counter for heavy ions", JPS Conf. Proc. 35 (2021) 011022. [DOI:10.7566/JPSCP.35.011022]

8. Z. Ge, S. Naimi, D. Nagae, Y. Abe, S. Omika, T. Uesaka, F. Suzaki, H. Li, Y. Yamaguchi, M. Wakasugi, K. Wakayama, T. Yamaguchi, A. Ozawa, H. Arakawa, K. Inomata, T. Kobayashi, K. Nishimuro, S. Suzuki, T. Moriguchi, D. Kamioka, M. Mukai, M. Amano, A. Kitagawa, S. Sato, G. Lorusso, Y. Yano, "Development of mirror-type MCP detectors for mass measurements at the Rare-RI Ring", JPS Conf. Proc. 35 (2021) 011023. [DOI:10.7566/JPSCP.35.011023]

9. K. Wakayama, T. Yamaguchi, Y. Abe, M. Amano, H. Arakawa, Z. Ge, K. Inomata, D. Kamioka, A. Kitagawa, T. Kobayashi, H. Li, T. Moriguchi, D. Nagae, S. Omika, A. Ozawa, S. Sato, S. Suzuki, T. Suzuki, N. Tadano, "A Simple Readout Method for a Position-Sensitive Detector Using Plastic Scintillator Bars", JPS Conf. Proc. 35 (2021) 011024. [DOI:10.7566/JPSCP.35.011024]

10. H. Li, Z. Ge, S. Naimi, D. Nagae, Y. Abe, T. Uesaka, F. Suzaki, M. Wakasugi, S. Omika, Y. Yamaguchi, T. Yamaguchi, K. Wakayama, H. Arakawa, K. Inomata, A. Ozawa, S. Suzuki, T. Moriguchi, "MCP with delay-line anode used for position sensitive detector at Rare RI Ring", JPS Conf. Proc. 35 (2021) 011025. [DOI:10.7566/JPSCP.35.011025]

11. S. Omika, T. Yamaguchi, Y. Abe, M. Amano, H. Arakawa, Z. Ge, K. Inomata, D. Kamioka, H. Li, H. Miura, T. Moriguchi, D. Nagae, S. Naimi, K. Nishimuro, A. Ozawa, F. Suzaki, S. Suzuki, T. Suzuki, N. Tadano, T. Uesaka, M. Wakasugi, K. Wakayama, Y. Yanagisawa, Y. Yamaguchi, "Development of experimental devices for precise mass measurements at the Rare-RI Ring Facility", JPS Conf. Proc. 35 (2021) 011026. [DOI:10.7566/JPSCP.35.011026]

12. X. Zhou, M. Zhang, M. Wang, Y. H. Zhang, Y. J. Yuan, X. L. Yan, X. H. Zhou, H. S. Xu, X. C. Chen, Y. M. Xing, R. J. Chen, X. Xu, P. Shuai, C. Y. Fu, Q. Zeng, M. Z. Sun, H. F. Li, Q. Wang, T. Bao, M. Si, H. Y. Deng, M. Z. Liu, T. Liao, J. Y. Shi, Y. N. Song, J. C. Yang, W. W. Ge, Yu. A. Litvinov, S. A. Litvinov, R. S. Sidhu, T. Yamaguchi, S. Omika, K. Wakayama, S. Suzuki, T. Moriguchi, "In-ring velocity measurement for isochronous mass spectrometry", Phys. Rev. Accel. Beams 24 (2021) 042802. [DOI:10.1103/PhysRevAccelBeams.24.042802]

13. M. Ahmed, Y. X. Watanabe, Y. Hirayama, M. Mukai, J. H. Park, P. Schury, Y. Kakiguchi, A. Ozawa, M. Oyaizu, M. Wada, H. Miyatake, "β-γ spectroscopy of the ^{195}Os nucleus", Phys. Rev. C 103 (2021) 054312. [DOI:10.1103/PhysRevC.103.054312]

ACCELERATOR MASS SPECTROMETRY

1. K. Kanzawa, F. Miyake, K. Horiuchi, K. Sasa, K. Takano, M. Matsumura, T. Takahashi, Y. Motizuki, K. Takahashi, Y. Nakai, K. Ohtani, Y. Tada, Y. Ochiai, H. Motoyama, H. Matsuzaki, A. Yamazaki, Y. Muramatsu, T. Yamagata, "High-Resolution ^{10}Be and ^{36}Cl Data from the Antarctic Dome Fuji Ice Core (~100 years around 5480 BCE): An Unusual Grand Solar Minimum Occurrence?", Journal of Geophysical Research: Space Physics 126 (2021) e2021JA029378. [DOI:10.1029/2021JA029378]

2. K. Hain, M. Martschini, F. Gülce, M. Honda, J. Lachner, M. Kern, J. Pitters, F. Quinto, A. Sakaguchi, P. Steier, A. Wiederin, A. Wieser, A. Yokoyama, R. Golser, "Developing accelerator mass spectrometry capabilities for anthropogenic radionuclide analysis to extend the set of oceanographic tracers", Front. Mar. Sci. 9 (2022) 837515. [DOI:10.3389/fmars.2022.837515]

3. A. Nakajima, K. Teranishi, A. Yokoyama, A. Sakaguchi, K. Hain, R. Morita, A. Sato, A. Nagai, D. Mori, Y. Komori, T. Yokota, Y. Wang, H. Haba, "Measurement of the isotopic ratio of Np-236 to Np-237 in Th-232 + Li-7 reaction products by accelerator mass spectrometry", RIKEN accel. Prog. Rep. 54 (2021) 142.

4. K. Sakata, Y. Takahashi, S. Takano, A. Matsuki, A. Sakaguchi, H. Tanimoto, "First X-ray Spectroscopic Observations of Atmospheric Titanium Species: Size Dependence and the Emission Source", Environ. Sci. Technol. 55 (2021) 10975. [DOI:10.1021/acs.est.1c02000]

BEAM AND ISOTOPE APPLICATIONS

1. H. Kudo, H. Naramoto, M. Sataka, S. Ishii, K. Sasa, S. Tomita, "Depth resolution of transmission ERDA for H in Al under nuclear-elastically enhanced recoiling of H by 8 MeV He", J. Phys.: Condens. Matter 33 (2021) 465901. [DOI:10.1088/1361-648X/ac17ac]

2. Y. Sugisawa, I. Harayama, Y. Takimoto, T. Wakasugi, Y. Hirose, T. Hasegawa, S. Ishii, D. Sekiba, "Installation of TOF-E telescope ERDA in UTTAC at the University of Tsukuba: analysis of metal-nitride-based multi-layer coatings on glasses", Nucl. Insrum. Methods Phys. Res. B 503 (2021) 68. [DOI:10.1016/j.nimb.2010.07.006]

3. Y. Liu, Y. Hisamatsu, S. Sharmin, D. Oshima, S. Iwata, T. Kato, D. Sekiba, E. Kita, H. Yanagihara, "Topotactic crystal structure transformation from spinel ferrite to wüstite in epitaxial Fe_3O_4 films via Kr ion irradiation", J. Vac. Sci. Technol. A39 (2021) 033403. [DOI:10.1116/6.0000885]

4. R. Murase, H. Tsuchida, S. Nakagawa, S. Tomita, A. Chiba, K. Nakajima, T. Majima, M. Saito, "Effect of structure and orientation of incident carbon-cluster ions C_n^+($n \leq 4$) on secondary-ion emission induced by electronic excitation", Phys. Rev. A103 (2021) 062812. [DOI:10.1103/PhysRevA.103.062812]

5. M. Sumiya, Y. Takahara, A. Alghamdi, Y. Nakayama, F. Uesugi, Y. Harada, A. Uedono, Y. Imanaka, "Growth of $Al_xGa_{1-x}N/In_yGa_{1-y}N$ hetero structure on AlN/sapphire templates exhibiting Shubnikov-de Haas oscillation", J. Cryst. Growth 574 (2021) 126324. [DOI:10.1016/j.jcrysgro.2021.126324]

6. A. Uedono, R. Tanaka, S. Takashima, K. Ueno, M. Edo, K. Shima, K. Kojima, S. F. Chichibu, S. Ishibashi, "Dopant activation process in Mg-implanted GaN studied by monoenergetic positron beam", Sci. Rep. 11 (2021) 20660. [DOI:10.1038/s41598-021-00102-2]

7. H. Okumura, R. Jinno, A. Uedono, M. Imura, "Optical and electrical properties of silicon-implanted α-Al_2O_3", Jpn. J. Appl. Phys. 60 (2021) 106502. [DOI:10.35848/1347-4065/ac21af]

8. P. Muhammed Shafi, E. Kurian, N. Joseph, S. Sellaiyan, A. Uedono, A. Chandra Bose, "Effect of Ag doping on crystallinity and microstrain of $LaMnO_3$ nanoparticles: Confirmations of defect levels with positron lifetime and Doppler-broadening calculations", Phys. B 615 (2021) 413087. [DOI:10.1016/j.physb.2021.413087]

9. A. Sagara, H. Yabe, X. Chen, B. Put, T. Hantschel, M. Mees, H. Arase, Y. Kaneko, A. Uedono, P. M. Vereecken, "Interfacial Conductivity Enhancement and Pore Confinement Conductivity-Lowering Behavior inside the Nanopores of Solid Silica-gel Nanocomposite Electrolytes", ACS Appl. Mater. Interfaces 13 (2021) 40543. [DOI:10.1021/acsami.1c09246]

10. T. Hamada, Y. Nakanishi, K. Okada, S. Tsukada, A. Uedono, J. Ohshita, "Thermal insulating property of silsesquioxane hybrid film induced by intramolecular void spaces", ACS Appl. Polym. Mater. 3 (2021) 3383. [DOI:10.1021/acsapm.1c00344]

11. A. Uedono, J. Takino, T. Sumi, Y. Okayama, M. Imanishi, S. Ishibashi, Y. Mori, "Vacancy-type defects in bulk GaN grown by oxide vapor phase epitaxy probed using positron annihilation", J. Cryst. Growth 570 (2021) 126219. [DOI:10.1016/j.jcrysgro.2021.126219]

12. M. Akazawa, R. Kamoshida, S. Murai, T. Kachi, A. Uedono, "Low-temperature annealing behavior of

defects in Mg-ion-implanted GaN studied using MOS diodes and monoenergetic positron beam", Jpn. J. Appl. Phys. 60 (2021) 016502. [DOI:10.35848/1347-4065/abcf08]

13. K. Shima, R. Tanaka, S. Takashima, K. Ueno, M. Edo, K. Kojima, A. Uedono, S. Ishibashi, S. F. Chichibu, "Improved minority carrier lifetime in p-type GaN segments prepared by vacancy-guided redistribution of Mg", Appl. Phys. Lett. 119 (2021) 182106. [DOI:10.1063/5.0066347]

14. L. Y. Li, K. Shima, M. Yamanaka, K. Kojima, T. Egawa, A. Uedono, S. Ishibashi, T. Takeuchi, M. Miyoshi, S. F. Chichibu, "Reduced nonradiative recombination rates in c-plane $Al_{0.83}In_{0.17}N$ films grown on a nearly lattice-matched GaN substrate by metalorganic vapor phase epitaxy", Appl. Phys. Lett. 119 (2021) 019105. [DOI:10.1063/5.0066263]

7.2 Reviews and books

1. 冨田成夫，山崎明義，石井 聰，笹 公和，左高正雄，楢本 洋，工藤 博，"透過 ERDA によるアルミニウム中水素の 3 次元分布計測"，応用物理学会放射線分科会誌「放射線」47 (2021) 15.

7.3 Poster and oral presentations

1. 森口哲朗，小沢 顕，冨田啓介，大和良広，林 実香，要 直登，景澤怜央，向井もも，矢野朝陽，"回転磁場を用いた $^{25}Al, ^{29}P$ の核磁気モーメントの符号測定"，日本物理学会第 77 回年次大会，オンライン開催（2022 年 3 月 15–19 日).

2. 矢野朝陽，小沢 顕，森口哲朗，要 直登，福田光順，三原基嗣，福留美樹，高山 元，木村容子，田口 諒，本多裕也，林 双葉，田中聖臣，鈴木 健，山口貴之，神田真矩，関 響咲，西村太樹，高橋弘幸，菅原奏来，宇根千晶，大坪 隆，野口法秀，泉川卓司，佐藤眞二，福田茂一，北川敦志，"反応断面積測定のための固体重水素標的の開発"，日本物理学会第 77 回年次大会，オンライン開催 (2022 年 3 月 15–19 日).

3. 森口哲朗，小沢 顕，堀内 渉，阿部康志，北川敦志，向井もも，長江大輔，佐藤眞二，鈴木伸司，鈴木 健，山口貴之，"固体水素標的を用いた反応断面積のエネルギー依存性"，第 1 回日本量子医科学会学術大会，オンライン開催 (2021 年 12 月 10–11 日).

4. 要 直登, 森口哲朗，小沢 顕，山口貴之，Sarah Naimi，向井もも，鈴木伸司，"薄膜からの二次電子放出を利用した RI ビーム位置敏感型検出器の開発"，第 1 回日本量子医科学会学術大会，オンライン開催 (2021 年 12 月 10–11 日).

5. 山口貴之, 鈴木 健, 福田光順, 西村太樹, 田中聖臣, 長江大輔, 小沢 顕, 森口哲朗, 大坪 隆, "高エネルギー重イオンビームによる粒子検出器の開発と荷電変化反応の研究", 第 1 回日本量子医科学会学術大会, オンライン開催 (2021 年 12 月 10–11 日).

6. T. Moriguchi, A. Ozawa, Y. Yamato, M. Hayashi, R. Kagesawa, N. Kaname, M. Mukai, K. Tomita, A. Yano, "Status of Lamb-shift polarized ion source at 6MV tandem accelerator in UTTAC and its application to nuclear physics", The 24th International Spin Symposium (SPIN2021), Matsue, Shimane, Japan (Hybrid), Gather Online (Oct. 18–22, 2021).

7. T. Moriguchi, A. Ozawa, K. Tomita, Y. Yamato, M. Hayashi, N. Kaname, M. Mukai, A. Yano, "Measurement of the sign of nuclear moment for unstable nuclei ^{25}Al and ^{29}P by using rotating magnetic field", 3rd International Conference on Hyperfine Interactions and their Applications (HYPERFINE2021), Brasov, Romania (Hybrid), Gather Online (Sep. 5–10, 2021).

8. 森口哲朗, 小沢 顕, 冨田啓介, 要 直登, 矢野朝陽, 林 実香, 山口貴之, 鈴木 健, 梶木大輔, 濱川大貴, 原山朔弥, 大津美沙紀, Sarah Naimi, George Hudson-Chang, 山口由高, 向井もも, 長江大輔, 鈴木伸司, 西村太樹, 髙橋弘幸, 北川敦志, 佐藤眞二, 阿部康志, "RI ビーム飛行時間検出器の開発 -理研稀少 RI リングのための検出器", 2020 年度 HIMAC 共同利用研究成果発表会, オンライン開催 (2021 年 6 月 7–10 日).

9. T. Yamaguchi "Precision experiments of exotic nuclei at the storage rings", Tsukuba Global Science Week 2021, Gather Online (Sep. 6–11, 2021). (invited)

10. 秩父重英, 嶋 紘平, 小島一信, 高島信也, 上野勝典, 江戸雅晴, 井口紘子, 成田哲生, 片岡恵太, 石橋章司, 上殿明良, "エピタキシャル成長及びイオン注入により作製された GaN 基板上 Mg 添加 p 型 GaN の室温フォトルミネッセンス寿命", 第 69 回応用物理学会春季学術講演会, 青山学院大学 ハイブリッド開催 (2022 年 3 月 23 日). （招待講演）

11. Y. Wakiyama, M. Matumura, T. Matsunaka, S. Hirao, K. Sasa, "Behavior of ^{129}I in the Abukuma river during two high-flow events in 2018", EGU General Assembly, vEGU21: Gather Online (Apr. 19–30, 2021).

12. K. Sasa, M. Matsumura, T. Takahashi, "Development of Non-Radiocarbon Accelerator Mass Spectrometry at the University of Tsukuba", Technical Meeting on Developments in Non-Radiocarbon Accelerator Mass Spectrometry Techniques and Relevant Applications, International Atomic Energy Agency (IAEA), Gather Online (Oct. 11–14, 2021).

13. K. Sasa, Y. Ochiai, Y. Tosaki, T. Matsunaka, T. Takahashi, M. Matsumura, K. Sueki, "Chlorine-36 deposition at Tsukuba, Japan, after the Fukushima Daiichi Nuclear Power Plant accident", The 15th

International Accelerator Mass Spectrometry Conference (AMS-15), Sydney, Australia, Gather Online (Nov. 15–19, 2021).

14. K. Sasa, M. Matsumura, T. Matsunaka, T. Takahashi, Y. Satou, N. Kinoshita, H. Matsuzaki, K. Sueki, "Determination of I-129/I-131 in surface soils related to the Fukushima Daiichi Nuclear Power Plant accident", The 15th International Accelerator Mass Spectrometry Conference (AMS-15), Sydney, Australia, Gather Online (Nov. 15–19, 2021).

15. M. Matsumura, K. Sasa, A. Sakaguchi, T. Matsunaka, T. Takahashi, K. Sueki, "Status report of the Tsukuba 6MV multi-nuclide AMS system: Progress in iodine-129 AMS", The 15th International Accelerator Mass Spectrometry Conference (AMS-15), Sydney, Australia Gather Online (Nov. 15–19, 2021).

16. M. Matsumura, K. Sasa, Y. Ochiai, Y. Tosaki, T. Matsunaka, T. Takahashi, K. Sueki, "Regional dependence of Be-10 and Cl-36 variations in rainwater at the Sea of Japan and Pacific sides of Japan", The 15th International Accelerator Mass Spectrometry Conference (AMS-15), Sydney, Australia, Gather Online (Nov. 15–19, 2021).

17. T. Matsunaka, S. Nagao, S. Ochiai, T. Takahashi, M. Matsumura, K. Sueki, K. Sasa, "Anthropogenic iodine-129 depositions at the Sea of Japan and Pacific sides of the Japanese archipelago, during 2017–2018", The 15th International Accelerator Mass Spectrometry Conference (AMS-15), Sydney, Australia, Gather Online (Nov. 15–19, 2021).

18. T. Matsunaka, S. Nagao, M. Inoue, Y. Taniuchi, H. Kasai, T. Takahashi, M. Matsumura, K. Sueki, K. Sasa, "Surface distribution of iodine-129 in the southwestern Okhotsk Sea in 2018", The 15th International Accelerator Mass Spectrometry Conference (AMS-15), Sydney, Australia, Gather Online (Nov. 15–19, 2021).

19. K. Sueki, Y. Ohta, H. Yokoyama, Y. Ochiai, S. Hosoya, M. Honda, Y. Satou, T. Matsunaka, T. Takahashi, M. Matsumura, K. Sasa, "Chlorine-36 and Iodine-129 Inventories in Difficult-to-return Zone in Fukushima", The 15th international Accelerator Mass Spectrometry Conference (AMS-15), Sydney, Australia, Gather Online (Nov. 15–19, 2021).

20. H. Shen, S. Shi, J. Tang, M. Qi, S. Wei, M. Liu, W. Li, Z. Guofeng, K. Sasa, W. Mingjun, G. Shanhua, D. Junyan, "The ^{14}C-AMS technology and its applications for evaluation of the properties of highly permeable aquifers cause by large volume water injection in oil field", Radiocarbon in the Environment III Conference, Gliwice, Poland (Jul. 5–6, 2021).

21. 杉澤悠紀, 小林 成, 岸奈津子, 清水亮太, 一杉太郎, 関場大一郎, "核反応法を用いた全固体リチウムイオン電池中 Li のオペランド深さ分布測定", 日本物理学会 2021 年秋季大会, オンライン開催　(2021 年 9 月 20–23 日). (日本物理学会学生優秀発表賞受賞講演)

22. 冨田成夫, 菅沼瑠里, 畑田颯太, 川崎銀河, 椎名陽子, 左高正雄, 松田 誠, 今井 誠, 石井 聰, 笹 公和, "コンボイ電子収量におけるクラスター効果の入射粒子依存性", 日本物理学会 2021 年秋季大会, オンライン開催　(2021 年 9 月 20–23 日).

23. 笹 公和, 石井 聰, 高橋 努, 大和良広, 田島義一, 松村万寿美, 森口哲朗, 上殿明良, "筑波大学タンデム加速器施設の現状報告" 日本加速器学会第 18 回年会, オンライン開催 (2021 年 8 月 9–12 日).

24. 笹 公和, 石井 聰, 高橋 努, 大和良広, 田島義一, 松村万寿美, 森口哲朗, 上殿明良, "筑波大学タンデム加速器施設 UTTAC の現状", 第 33 回 タンデム加速器及びその周辺技術の研究会, 国立研究開発法人量子科学技術研究開発機構, オンライン開催 (2021 年 6 月 24–25 日).

25. 笹 公和, 落合悠太, 松村万寿美, 高橋 努, 松中哲也, "加速器質量分析法を用いた長半減期放射性ハロゲン ^{36}Cl と ^{129}I の高感度検出による降下量変動の比較研究", 第 82 回応用物理学会秋季学術講演会, オンライン開催 (2021 年 9 月 10–13 日).

26. 吉田 剛, 松村 宏, 中村 一, 豊田晃弘, 三浦太一, 桝本和義, 笹 公和, 森口哲朗, 松村万寿美, "可搬型 γ 線イメージング装置 GeGI5 による加速器放射化評価の可能性", 日本放射化学会第 65 回討論会 (2021), オンライン開催 (2021 年 9 月 22–24 日).

27. 椎根大輔, 坂口 綾, 笹 公和, 松村万寿美, 高橋 努, 末木啓介, 山﨑信哉, "核分裂生成核種 ^{135}Cs の測定法確立に向けた取り組みと水圏科学研究への応用", 2021 年度日本地球化学会第 68 回年会, 弘前大学, ハイブリッド開催 (2021 年 9 月 1–15 日).

28. 西塚魁人, 坂口 綾, 笹 公和, 高橋 努, 松村万寿美, 三浦 勉, 浅井志保, 和田彩佳, 高久雄一, 山﨑信哉, 末木啓介, "水環境中における有機・無機ヨウ素同位体定量の試み", 2021 年度日本地球化学会第 68 回年会, 弘前大学, ハイブリッド開催 (2021 年 9 月 1–15 日).

29. 大石脩人, 村尾吉輝, 新田紀子, 土田秀次, 冨田成夫, 笹 公和, 平田浩一, 柴田裕実, 平野貴美, 山田圭介, 千葉敦也, 齋藤勇一, 鳴海一雅, 星野 靖, "高速 C_{60} クラスターイオンビーム照射による Si 表面構造の形態変化", QST 高崎サイエンスフェスタ 2021, 国立研究開発法人量子科学技術研究開発機構量子ビーム科学部門高崎量子応用研究所, ハイブリッド開催 (2021 年 12 月 7–8 日).

30. 西塚魁人，坂口　綾，浅井志保，本多真紀，高久雄一，笹　公和，高橋　努，松村万寿美，和田彩佳，三浦　勉，山﨑信哉，末木啓介，"水環境中における有機・無機ヨウ素同位体定量の試み"，福島大学環境放射能研究所第 8 回成果報告会　福島原発事故後の環境放射能 〜研究成果から見える将来〜，コラッセふくしま，福島県福島市 (2022 年 2 月 28 日–3 月 1 日).

31. 椎根大輔，坂口　綾，笹　公和，松村万寿美，高橋　努，山﨑信哉，末木啓介，"海水循環トレーサー利用に向けた極微量放射性核種 ^{135}Cs の測定法確立"，第 23 回「環境放射能」研究会，オンライン開催 (2022 年 3 月 8–10 日).

32. 吉田　剛，松村　宏，中村　一，豊田晃弘，三浦太一，桝本和義，笹　公和，森口哲朗，松村万寿美，"可搬型 γ 線イメージング装置 GeGI5 を用いた加速器放射化評価への応用の見込み"，第 23 回「環境放射能」研究会，オンライン開催 (2022 年 3 月 8–10 日).

33. 笹　公和，高橋　努，椎根大輔，松村万寿美，坂口　綾，"Rb スパッタイオン源からの負イオンビームの生成"，応用物理学会 2022 年第 69 回春季学術講演会，青山学院大学，ハイブリッド開催 (2022 年 3 月 22–26 日).

34. 冨田成夫，菅沼瑠里，畑田颯太，椎名陽子，高橋　努，石井　聡，笹　公和，"コンボイ電子収量におけるクラスター効果の入射粒子依存性 II"，日本物理学会　第 77 回年次大会，オンライン開催 (2022 年 3 月 15–19 日).

35. 畑田颯太，鈴木裕太郎，冨田成夫，"FPGA を用いた MCA の構築"，原子衝突学会第 46 回年会，オンライン開催 (2021 年 10 月 26–28 日).

36. 上殿明良，大島永康，満汐孝治，"陽電子消滅による配線材料の空孔検出 −後工程材料評価への応用−"，第 4 回量子ビーム計測クラブ研究会，オンライン開催 (2021 年 12 月 22 日).（招待講演）

37. A. Uedono, M. Dickmann, W. Egger, C. Hugenschmidt, S. Ishibashi, "Study of point defects in group-III nitrides by means of positron annihilation spectroscopy", MLZ User meeting, Gather Online (Dec. 7, 2021). (invited)

38. A. Uedono, "Development of Information and Communication Technology (ICT), and its impact on education", JANET – Japanisches Kulturinstitut forum (Nov. 12, 2021). (invited)

39. A. Uedono, M. Dickmann, W. Egger, C. Hugenschmidt, S. Ishibashi, "Carrier trapping by vacancies in semiconductors studied using positron annihilation spectroscopy − a collaboration work between TUM and University of Tsukuba", The joint MLZ and physics department lecture series (May 3, 2021). (invited)

40. 上殿明良, "陽電子消滅を用いた材料の欠陥, 自由体積の検出", コンピュータによる材料開発・物質設計を考える会 (CAMM フォーラム), オンライン開催 (2021 年 4 月 2 日).
（招待講演）

41. 秩父重英, 嶋 紘平, 小島一信, 高島信也, 上野勝典, 江戸雅晴, 井口紘子, 成田哲生, 片岡恵太, 石橋章司, 上殿明良, "エピタキシャル成長及びイオン注入により作製された GaN 基板上 Mg 添加 p 型 GaN の室温フォトルミネッセンス寿命", 応用物理学会春季学術講演会, 青山学院大学, ハイブリッド開催 (2022 年 3 月 22–26 日). (第 43 回優秀論文賞受賞記念講演)

42. 磯谷順一, 原 英之, 渡邊賢司, 角谷 均, 小野田 忍, 寺地徳之, 渡邊幸志, 梅田享英, 上殿明良, "HPHT ダイヤモンド結晶の EPR イメージング", 第 36 回ダイヤモンドシンポジウム, 慶應義塾大学矢上キャンパス (2021 年 11 月 17–19 日).

43. 上殿明良, 田中 亮, 高島信也, 上野勝典, 江戸雅晴, 嶋 紘平, 小島一信, 秩父重英, 石橋章司, "陽電子消滅を用いた Mg イオン注入により形成した p 型 GaN の Mg 活性プロセスと空孔型欠陥の研究", 第 82 回応用物理学会秋季学術講演会, オンライン開催 (2021 年 9 月 21–23 日).

44. 嶋 紘平, 田中 亮, 高島信也, 上野勝典, 江戸雅晴, 小島一信, 上殿明良, 秩父重英, "空孔ガイド Mg 拡散法による p 型イオン注入 GaN の空間分解 CL 評価", 第 82 回応用物理学会秋季学術講演会, オンライン開催 (2021 年 9 月 21–23 日).

45. 佐々木泰祐, 宝野和博, 上殿明良, "Mg 合金中のクラスター対相互作用による $L1_2$ クラスター層の積層配列", 日本金属学会 2021 年秋期（第 169 回）大会, オンライン開催 (2021 年 9 月 14–17 日).

46. 角谷正友, 後藤 修, Sang Liwen, 高原悠希, 上殿明良, 今中康貴, 今野泰一郎, 堀切文正, 木村健司, 藤倉序章, "AlN/SiC テンプレート上にヘテロ成長した GaN-HEMT 構造の特性評価", 第 82 回応用物理学会秋季学術講演会, オンライン開催 (2021 年 9 月 10–13 日).

47. 喜多英治, 小野寺礼尚, 岸本幹雄, 柳原英人, "凍結した磁性流体のメスバウアー効果と磁気緩和", 日本磁気学会講演会, オンライン開催 (2021 年 8 月 1 日–9 月 2 日).

7.4 UTTAC seminars

2021.11.24   Measurements of Higher-Order Cumulants of Net-Proton Distributions in 200 GeV p+p Collisions at RHIC-STAR, *Risa Nishitani (University of Tsukuba)*

2021.12.21   Development of Time-of-Flight detector MRPC for J-PARC E16 experiment and performance evaluation with 30 GeV proton beam in J-PARC, *Shono Kyan (University of Tsukuba)*

2021.12.21   Measurement of multiplicity dependence of electrons from beauty-hadron decay in pp and p-Pb collisions at $\sqrt{s_{NN}}$ = 5.02 TeV with LHC-ALICE, *Shunya Chiba* (*University of Tsukuba*)

2021.12.21   Measurement of transverse momentum and multiplicity dependence of heavy-flavor jets production in pp collisions at $\sqrt{s}$ = 13 TeV with LHC-ALICE, *Momo Eshita (University of Tsukuba)*

2022.1.11   Identification of quark and gluon jets by machine learning in pp collisions at $\sqrt{s}$ = 13 TeV with LHC-ALICE, *Shuto Okada* (*University of Tsukuba*)

2022.1.11   Measurement of neutral mesons inside jets in pp collisions at $\sqrt{s}$ = 13 TeV with ALICE at the LHC, *Hanseo Park (University of Tsukuba)*

2022.1.11   Measurements of directed flow at forward and central rapidity region in 400AMeV Xe + CsI collisions in HIMAC H447 experiment, *Hidaka Tanabe (University of Tsukuba)*

2022.1.11   Development of the RI beam position detector using the time-of-flight difference of secondary electrons emitted from a thin foil, *Naoto Kaname (University of Tsukuba)*

8.

THESES

Photo by N. Shimada

From the "real" backyard of UTTAC

This stray cat, sitting beside Tajima-san, lives maybe in the forest area adjacent to the UTTAC facility.

Doctor thesis

Yuki Sugisawa

Development of ERDA and NRA for light element depth profile in functional thin films (機能性薄膜中軽元素の深さ分布測定に向けた ERDA および NRA の開発)

Master theses

Naoto Kaname

Development of the RI beam position detector using the time-of-flight difference of secondary electrons emitted from a thin foil (薄膜から放出される二次電子の飛行時間差を用いた RI ビーム位置検出器の開発)

Yurika Otani

Evaluation of oxide ion conduction properties in a solid oxide fuel cell material Y_2O_3-stabilized ZrO_2 with short-lived nucleus ^{19}O (短寿命核 ^{19}O を用いた固体酸化物形燃料電池材料 Y_2O_3 安定化 ZrO_2 中における酸化物イオン伝導特性の評価)

Takuro Narita

Characterization of vacancy-type defects in high-κ HfO_2 using positron annihilation spectroscopy (陽電子消滅法を用いた High-κ 材料 HfO_2 の空孔型欠陥評価)

Kouya Nitta

Characterization of free volume in fatigued CFRP using positron annihilation spectroscopy (陽電子消滅法を用いた疲労 CFRP の自由体積評価)

Kiyoshi Yoshimura

Characterization of vacancy-type defects in AlN using positron annihilation spectroscopy (陽電子消滅法を用いた AlN の空孔型欠陥評価)

Natsuko Kishi

Development of Auger electron spectrometer under ion channeling condition (チャネリング・オージェ電子観察に向けた電子分光器の開発)

Undergraduate theses

Atsuyuki Moriyama

Search for ejectile ions from arc plasma source (アークプラズマ蒸着源からの出射イオンの探索)

Maruko Hiraga

Development of beam current monitoring system for the 0-degree electron spectroscopy（0°電子分光用ビームカレントモニターの製作）

Yutaro Suzuki

Development of analyzing methods for the depth-profiling of hydrogen using transmission ERDA (透過型 ERDA における水素の深さ分布解析手法の開発)

Kazuma Torii

Characterization of vacancy-type defects in N- and Mg-implanted GaN using positron annihilation spectroscopy (陽電子消滅法を用いた N と Mg 注入 GaN の空孔型欠陥の評価)

Ryu Hioki

Characterization of vacancy-type defects in high-pressure-annealed p-type GaN implanted with Mg using positron annihilation spectroscopy (陽電子消滅法を用いた超高圧アニールによる Mg イオン注入 p 型 GaN の空孔型欠陥評価)

Kouta Homma

Characterization of free volume in fatigued CFRP using positron annihilation spectroscopy (陽電子消滅法を用いた CFRP 疲労試験材の自由体積評価)

Ryosuke Miura

Characterization of vacancy-type defects in high-κ gate-insulating films of HfO$_2$ using positron annihilation spectroscopy (陽電子消滅法を用いた High-κゲート絶縁膜 HfO$_2$ の空孔型欠陥評価)

Chihiro Kodaka

Crystal structure and magnetic properties of FeCo nitride fine particles synthesized by ammonia nitrification (アンモニア導入により作製した FeCo 窒化物微粒子の結晶構造と磁気特性)

9.

LIST OF PERSONNEL

Commemorating the retirement of engineer Mr. Tajima (center) after his 47-year contribution to UTTAC.

Tandem Accelerator Complex

A. Uedono	Director, Professor
K. Sasa	Associate Professor
D. Sekiba	Lecturer
T. Moriguchi	Assistant Professor
Y. Tajima	Mechanical Engineer
S. Ishii	Mechanical Engineer
T. Takahashi	Electrical Engineer
Y. Yamato	Electrical Engineer
M. Matsumura	Technical Staff
S. Kuramochi	Administrative Staff
N. Shimada	Administrative Staff
H. Muromachi	Administrative Staff

Research Members[1]

Department of Physics

A. Ozawa   K. Sasa   T. Moriguchi
T. Yamaguchi (Saitama University [Cross appointment])

Department of Applied Physics

A. Uedono   H. Yanagihara   H. Tanimoto   E. Kita
S. Tomita   D. Sekiba   S. Sharmin

Department of Geoscience

M. Kurosawa

Department of Biology

I. Suzuki

Department of Chemistry

K. Sueki   A. Sakaguchi

Department of Information and Systems

T. Kameda

---

[1] The "research members" include the authors and coauthors within 5 years back from this fiscal year, as well as the members of research projects running at UTTAC.

Staff of Open Advanced Facilities Initiative

H. Kudo	H. Naramoto	M. Sataka

K. Awazu (National Institute of Advanced Industrial Science and Technology [AIST])

S. Aoki (Comprehensive Research Organization for Science and Society [CROSS])

Graduate students

Y. Sugisawa	T. Ikeda	N. Kaname	H. Koizumi
D. Hirose	N. Kishi	T. Okamoto	S. Hatada
A. Yano	Y. Yue	A. Inoue	T. Yang
K. Nishizuka	Y. Gao	Z. Shi	D. Shiine
T. Nakamura	K. Sakakura	N. Takahashi	S. Oshida

Undergraduates

Y. Suzuki	M. Hiraga	A. Moriyama	R. Tanaka
R. Takatsuki	Y. Kurihara	H. Yoshikado	K. Torii
K. Homma	R. Hioki	R. Miura	

External users and collaborators

Y. Iwata	National Institute of Advanced Industrial Science and Technology (AIST)
K. Tomita	National Institute of Advanced Industrial Science and Technology (AIST)
S. Shiki	National Institute of Advanced Industrial Science and Technology (AIST)
T. Ishizuka	National Institute of Advanced Industrial Science and Technology (AIST)
H. Matsui	National Institute of Advanced Industrial Science and Technology (AIST)
T. Matsunaka	Kanazawa University
M. Honda	Japan Atomic Energy Agency (JAEA)
M. Mihara	Osaka University
Y. Otani	Osaka University
Y. Kimura	Osaka University
G. Takayama	Osaka University
M. Fukutome	Osaka University
T. Sugisaki	Osaka University
R. Uda	Osaka University
H. Yuta	Osaka University
T. Suzuki	Saitama University
M. Otsu	Saitama University
N. Shinozaki	Saitama University
M. Kanda	Saitama University
H. Seki	Saitama University

S. Harayama   Saitama University

K. Sasaki   Saitama University

S. Matsuda   Saitama University

K. Okubo   Saitama University

S. Sugimoto   Saitama University

Y. Koizumi   Saitama University

A. Yanai   Saitama University

T. Hitosugi   Tokyo Institute of Technology

R. Shimizu   Tokyo Institute of Technology

S. Kobayashi   Tokyo Institute of Technology

H. Matsumura   High Energy Accelerator Research Organization (KEK)

G. Yoshida   High Energy Accelerator Research Organization (KEK)

H. Nakamura   High Energy Accelerator Research Organization (KEK)

A. Toyoda   High Energy Accelerator Research Organization (KEK)

T. Miura   High Energy Accelerator Research Organization (KEK)